Ternary and Quaternary Rare-Earth Transition-Metal Germanides

by

Dong Zhang

A thesis submitted in partial fulfillment of the requirements for the degree of

Master of Science

Department of Chemistry
University of Alberta

Abstract

Ternary and quaternary germanides containing rare-earth and transition metals are of interest because of their structural diversity and the potential for interactions between f- and d-electrons. Within the Ce–Rh–Ge system, three new ternary phases $Ce_3Rh_{11}Ge_5$, $CeRh_5Ge_3$, and $CeRh_3Ge_2$ were prepared and their structures were determined by powder and single-crystal X-ray diffraction. Their bonding was examined by calculating electron localization functions and performing a Bader charge analysis, which confirms the description of the structures as consisting of electropositive Ce atoms embedded within an anionic network of Rh and Ge atoms. Within the *RE*–*M*–*X*–Ge (*RE* = rare-earth metal; *M* = Mn–Ni; *X* = Ag, Cd) system, 73 quaternary germanides $RE_4M_2XGe_4$ adopting the same monoclinic structure ($Ho_4Ni_2InGe_4$-type) were prepared. A prominent feature in these germanides is the presence of deficient *X* sites coordinated weakly to Ge atoms in square planar geometry, which may have implications for the low thermal conductivity predicted in these compounds, as confirmed in $Nd_4Mn_2AgGe_4$. Some representatives of these germanides exhibit additional disorder between the *M* and *X* atoms, as seen in $Nd_4(Mn_{0.78(1)}Ag_{0.22(1)})_2Ag_{0.83(1)}Ge_4$. Solid solutions of these germanides in combination with silicon was investigated in the series $Nd_4Mn_2Cd(Ge_{1-y}Si_y)_4$, in which two intermediate members as well as the end members were characterized structurally.

Preface

This thesis summarizes work carried out from September 2016 to December 2018 by me and co-workers in the Mar research group in the Department of Chemistry at the University of Alberta. Contributions to the work are detailed below.

Chapter 2 represents a manuscript in preparation titled "Ternary Rh-rich Germanides in the Ce–Rh–Ge System" authored by D. Zhang, A. O. Oliynyk, and A. Mar. I synthesized and characterized the compounds, collected and analyzed the data, and wrote the initial draft of the manuscript. A. O. Oliynyk assisted in data collection and analysis, and manuscript preparation. A. Mar edited the manuscript.

Chapter 3 has been published as Zhang, D.; Oliynyk, A. O.; Duarte, G. M.; Iyer, A. K.; Ghadbeigi, L.; Kauwe, S. K.; Sparks, T. D.; Mar, A. "Not Just Par for the Course: 73 Quaternary Germanides RE_4M_2XGe$_4$ (RE = La–Nd, Sm, Gd–Tm, Lu; M = Mn–Ni; X = Ag, Cd) and the Search for Intermetallics with Low Thermal Conductivity" *Inorganic Chemistry* **2018,** *57*, 14249–14259. I synthesized and characterized the compounds, collected and analyzed the data, and wrote the initial draft of the manuscript. A. O. Oliynyk assisted in synthesis and characterization, data collection and analysis, and manuscript preparation. G. M. Duarte assisted in synthesis and characterization, and data collection and analysis. A. K. Iyer assisted in data collection and analysis. L. Ghadbeigi and S. K. Kauwe carried out the thermal conductivity measurement. T. D. Sparks and A. Mar were co-corresponding authors of the manuscript.

Acknowledgements

I thank Arthur for mentoring, educating, and inspiring me during my two-year graduate school period. Arthur gave me numerous supports on my study, my research, and my life. He is always patient in guiding me through all the difficulties and patient in everything. I feel lucky and really appreciate to meet a supervisor like him.

I thank all group members past and present for their support on my academic path. I thank Krishna, Mansura, Danisa, Alex, Dundappa, Vidyanshu, and Amit. I especially appreciate the help from Anton, Wenlong, and Abishek. They helped me through all kinds of problems at beginning of the research. I am also grateful to Yuqiao, Jan, and Lawrence for their support.

I thank my supervisory committee members, Dr. Michaelis and Dr. Klobukowski, who supported me in my work since the first year of graduate school. I am grateful for other faculty and staff who gave me great support.

I thank the ATUMS program and all members within. This is a great program which made me open to other people and started making friends in Department of Chemistry. It also provided research funding support allowing me to go to Germany for an exchange visit. I thank Prof. Dr. Tom Nilges for hosting me in his lab for three months and giving me a chance to make new friends overseas. Ebru, Claudia, Anna, Markus, Felix, Patrick, and Annabelle helped me become familiar with different instruments in their lab.

I thank my parents, in-laws, and my wife for their support during a challenging time in life. They gave me the courage to start and continue my graduate study.

I thank all my colleagues and friends for their kindness and help on the path of my life.

Cheers!

Table of Contents

List of Figures

List of Tables

List of Symbols and Abbreviations

α	Thermal diffusivity
a, b, c	Unit cell parameters
CCD	Charge-coupled device
CPS	Curved position-sensitive detector
COHP	Crystal orbital Hamilton population
C_p	Heat capacity
DOS	Density of states
1D	One dimension
2D	Two dimensions
3D	Three dimensions
d	*d* spacing, distance between lattice planes
E	Energy
E_F	Fermi energy
EDX	Energy dispersive X-ray spectroscopy
ELF	Electron localization function
e^-	Electron
$\boldsymbol{F}$	Structure factor
Hz	Hertz
h, k, l	Miller indices
$\mathcal{H}$	Hamiltonian operator
I	Intensity
κ	Thermal conductivity

L	Thickness of substrate
λ	Wavelength
NMR	Nuclear magnetic resonance spectroscopy
n	Orders
ψ	Wave function
RE	Rare-earth metals
ρ	Density; or electron density
SEM	Scanning electron microscopy
T	Temperature
T_c	Critical temperature
T_N	Néel temperature
Tt	Tetrel, group 14 elements
TB-LMTO	Tight binding linear muffin tin orbital
t	Time
$t_{1/2}$	Half life
θ	Diffraction angle
U_{eq}	Displacement parameter
V	Cell volume
VASP	Vienna ab initio simulation package
XRD	X-ray diffraction
Z	Atomic number; or number of formula unit

Chapter 1 Introduction

Intermetallic compounds, which have numerous useful applications, are the focus of this research project. The major objective is to discover and characterize new intermetallic compounds.

1.1 Intermetallic Compounds

Metals are combined with other metals can lead to improved chemical and physical properties, such as greater resistance to corrosion and higher strengths. In early times, brasses (Cu–Zn alloys) and bronzes (Cu–Sn alloys) were used in daily life. In modern times, advanced applications include NiTi as a shape memory material used in satellites deploying and stents for blood vessel;[1–4] Nb_3Sn as a superconducting magnet (T_c = 18 K) found in nuclear magnetic resonance instruments;[5, 6] and Bi_2Te_3 as a thermoelectric material in portable solid-state refrigerators.[7]

Intermetallic compounds are defined as a class of compounds involving combinations of metals and having definite compositions and ordered structures. They can also include combinations with metalloids or nonmetals (provided that they are a minor component) such as some of the group 13 and 14 elements. An interesting class of intermetallic compounds contains combinations of rare-earth and transition metals, because the complex interactions of f- and d-electrons can lead to interesting physical properties, such as magnetism, heavy fermion behaviour, and superconductivity.[8] For example, U_2RhSi_3 exhibits long-range ferromagnetism below 24 K, $CeCoIn_5$ shows heavy-fermion superconductivity, and $CeCu_2Si_2$ is superconducting. The bonding in intermetallic compounds can also be quite diverse.[9–11]

Given the large number of metallic elements in the periodic table, there are many intermetallic compounds that remain to be discovered, which may lead to materials with new properties and applications.

1.2 Methods of Synthesis

Reactions in the solid state typically require higher temperature to proceed than those in solution, because they are largely limited by diffusion of atoms. In the ceramic method, the reactants are normally ground into fine powders and compressed into pellets to promote diffusion at high temperature.[12] The products that are formed could be one or a mixture of several phases, which may or may not be thermodynamically stable, and which may be amorphous or crystalline. Product with amorphous phase will have a short range order of structures with random network, while crystalline product will remain long range order structure with repeated units. To avoid formation of oxides, the samples are prepared in evacuated fused-silica tubes which are loaded

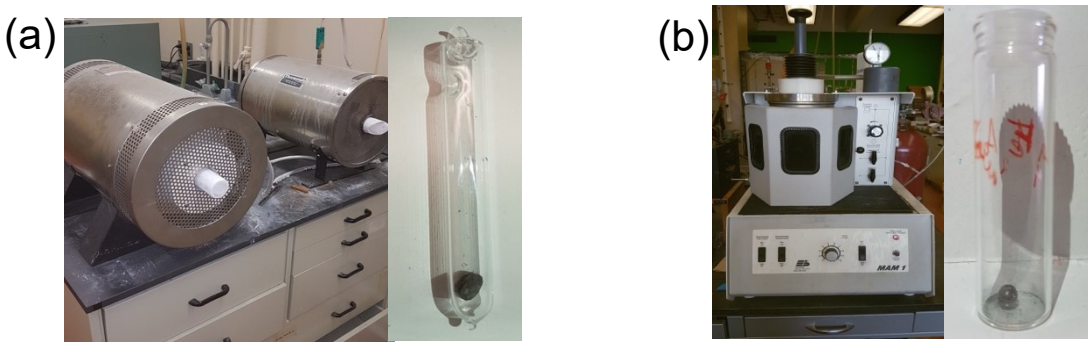

Figure 1-1. Synthesis of solid-state compounds. (a) Tube furnace and sealed fused-silica tube, (b) arc-melter and ingot sample.

into programmable tube furnaces (Figure 1-1a).

At high temperatures, reactants may melt or evaporate, which may facilitate reaction. Although fused-silica tubes are common containers, they cannot be used with alkali or alkaline-earth metals, and its softening point (1250 °C) limits the maximum temperature.[13] In cases where higher temperatures are required, arc-melting is an alternative method of synthesis in which an electric arc generated from high voltage on a water-cooled copper hearth within an argon-filled chamber attains temperatures as high as 4000 °C (Figure 1-1b). Samples can be instantly melted by the arc

to form ingots. To promote equilibration and crystallization, the arc-melted ingots are subsequently annealed (typically between 600 and 1000 °C for 7 to 10 days) within fused-silica tubes, which are then quenched in cold water. These samples are then analyzed by various techniques.

1.3 X-ray Diffraction

The primary method for structural characterization is X-ray diffraction, which can reveal the degree of crystallinity, the particle sizes of microcrystalline samples, and the detailed atomic arrangement of crystals.

1.3.1 X-ray Source

X-rays are a form of electromagnetic radiation with higher energy and shorter wavelength than visible light. Because of their high energy and strong penetrating ability, they are used in many areas such as medical photography and scientific analysis. X-rays are generated when electrons accelerated by high voltage (30–50 kV) strike a metal anode target (Figure 1-2).[14]

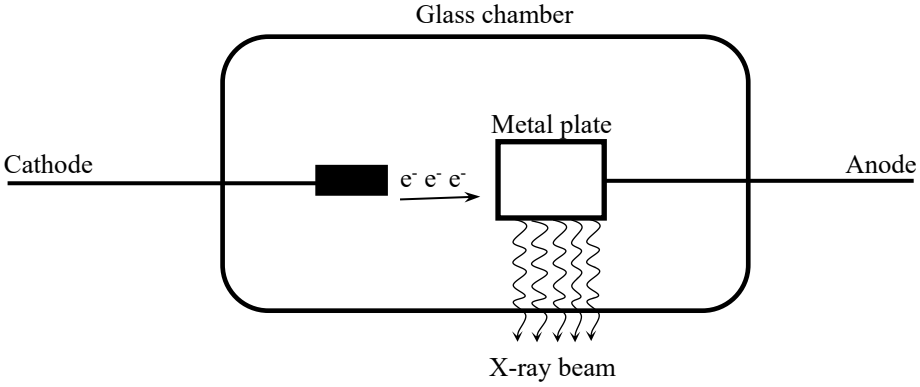

Figure 1-2. Generation of X-rays.

Two types of radiation are generated in the process: a continuous background called white radiation arising from inelastic collisions, and characteristic peaks at specific wavelengths which arise when core electrons are removed and higher-energy electrons relax into these levels (Figure

1-3). The wavelengths of characteristic X-rays can range from 0.1 to 100 Å, and they depend on the type of material in the metal anode. For most crystallographic investigations, Cu or Mo anodes are commonly used considering their signal intensity and diffraction resolution, with the intense

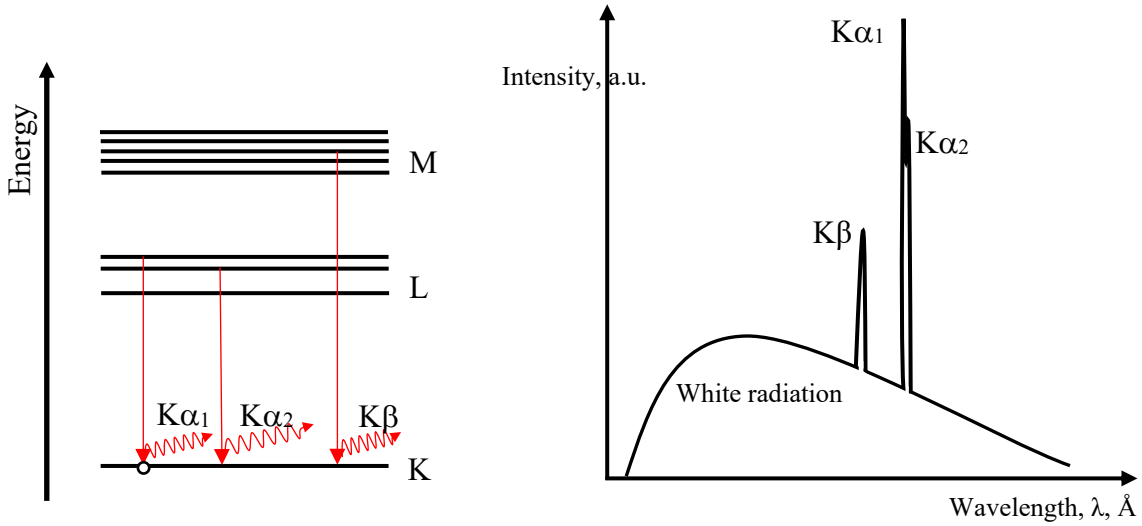

Figure 1-3. (a) Energy-level diagram, (b) X-ray spectrum generated with characteristic peaks and white radiation.

*K*α peak chosen and filtered from the white radiation and the other peaks. Monochromatic *K*α radiation has a wavelength of 1.5418 Å (Cu) or 0.7107 Å (Mo).[14]

1.3.2 Single-Crystal X-ray Diffraction

A crystal contains atoms in regular arrangements with long-range order. The repeat pattern can be described in terms of a *lattice*, which is a collection of points such that each point has the same environment as any other point. The contents of the unit cell are described by a *basis*, which is the set of atoms associated with each lattice point. Locations of atoms are specified by fractional coordinates *x*, *y*, *z* relative to the unit cell axes *a*, *b*, *c*. By making use of symmetry relationships (within 230 possible space groups), only a subset of these atoms needs to be specified.[14–16]

Diffraction occurs when incident X-rays strike lattice points and scatter in different directions. If the incident radiation approaches a row of lattice points at an angle μ, and becomes

scattered along a cone at an angle ν, the condition for constructive interference is that the path difference is an integer multiple of the wavelength. In three-dimensions, three cones must intersect (Figure 1-4).[17]

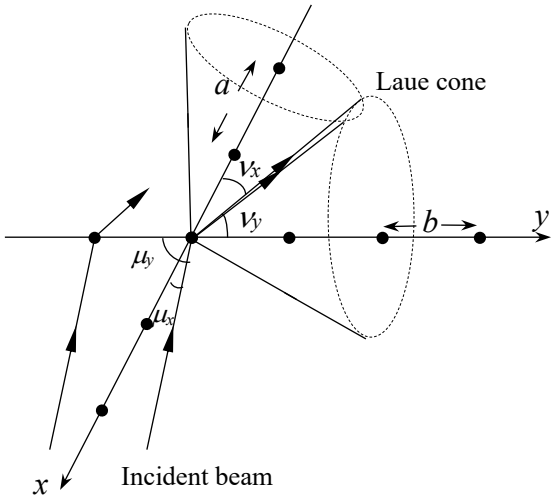

Figure 1-4. Plot of diffraction generated from a lattice plane with Laue cone.

The conditions for diffraction are thus specified by satisfying the equations below:

$$a\,(\cos\nu_x - \cos\mu_x) = n_x\lambda = h\lambda;$$

$$b\,(\cos\nu_y - \cos\mu_y) = n_y\lambda = k\lambda;$$

$$c\,(\cos\nu_z - \cos\mu_z) = n_z\lambda = l\lambda$$

A simpler analysis views the diffraction phenomenon as being equivalent to reflection of X-rays off neighbouring sets of lattice planes with spacing d (Figure 1-5).[18]

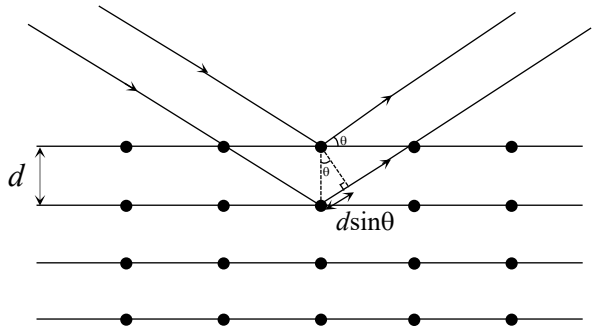

Figure 1-5. Bragg's law explanation on a 2D lattice plane.

The condition for diffraction, known as Bragg's law, becomes:

$$2d \sin\theta = n\lambda$$

Crystals obtained from the synthesis of intermetallic compounds are typically small, ranging from 0.05 to 0.2 mm in dimension. A single-crystal sample is attached to the tip of a glass fibre with adhesive or oil, and the specimen is placed on an adjustable three-circle goniometer, which is seated on a stage of the diffractometer (Bruker PLATFORM). The X-ray source generates Mo *K*α radiation and a SMART APEX II CCD area detector measures the diffracted radiation. To satisfy the geometrical conditions for diffraction, the goniometer is rotated over different angles (ω, ϕ) and the area detector collects frames of data over an exposure time of 10 – 20 s, depending on the crystal quality and the distance to the detector. A typical CCD frame shows many diffraction spots whose intensities are then obtained by integration (Figure 1-6).

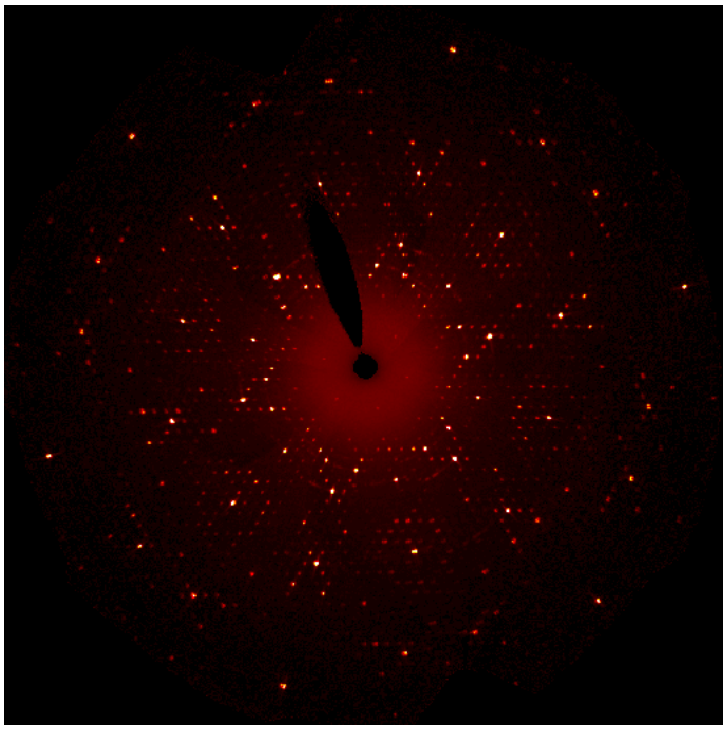

Figure 1-6. A CCD frame for $CeRh_5Ge_3$.

From the intensities of diffracted spots, I_{hkl}, the magnitude of observed structure factors $|\boldsymbol{F}_{obs}|$ are obtained by taking the square root. The structure factors contain information about the

electron density function of the crystal structure, which can be obtained by Fourier transform.[19] These structure factors are complex-valued, and may be represented as a vector with a magnitude and phase in complex number space. However, the experimental measurement only provides the magnitudes and not the phases of the structure factors. Therefore, these phases are guessed (through probabilistic methods) or structural models are proposed, and the magnitudes of calculated structure factors are compared with those of the experimental structure factors. The structure model is adjusted until better agreement is achieved. The quality of the agreement is measured by various residual indices (R or wR) as well as a goodness of fit.[19] In general, a value of $R < 0.05$ indicates good agreement. The standard crystallographic program package SHELXTL is used for structure solution and refinement.

1.3.3 Powder X-ray Diffraction

Diffraction patterns can also be obtained from powder samples. Unlike single-crystal diffraction, where discrete spots are observed, powder diffraction patterns consist of concentric rings arising from crystallites in random orientations. A powder diffraction pattern consists of intensities of various diffraction peaks plotted against the angle 2θ (Figure 1-7). Experimental powder diffraction patterns were collected on an Inel powder diffractometer with Cu $K\alpha$ X-ray radiation source and a curved position-sensitive (CPS) detector, which can collect data simultaneously in a 2θ range of 0–120°.

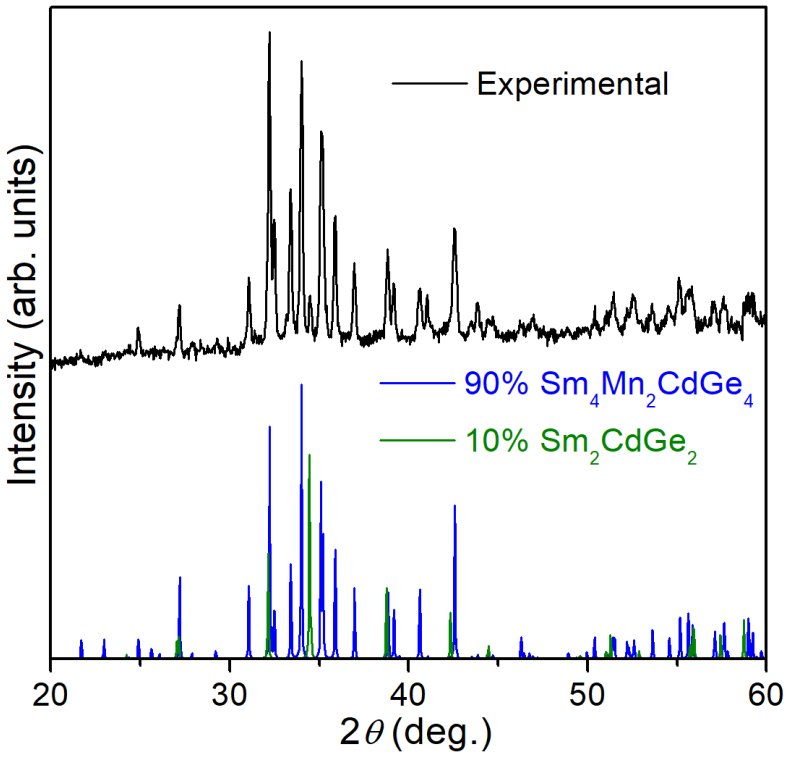

Figure 1-7. Powder X-ray diffraction pattern for $Sm_4Mn_2CdGe_4$ compared with simulated pattern, with 10% of Sm_2CdGe_2 phase.

Powder diffraction is primarily used to identify the phases present in a sample, by comparing experimental patterns with ones simulated from known or proposed structures. The relative amounts of phases can be estimated from the peak intensities. Unit cell parameters of a new phase can be refined from the precise angles of peaks, through the use of peak-fitting software such as WinCSD.

1.4 Electron Microscopy

An electron beam striking the surface of a solid can undergo many types of interactions (Figure 1-8).[20] Some of the electrons are scattered or penetrate the surface, secondary electrons can be generated, and characteristic X-rays can also be produced. Even some of the electrons can

transmit through a thin substrate layer. The volume where those interactions occur is called the interaction volume, which depends on substrate material, incident angle, and accelerating voltage. A common penetration depth is only few micrometers. The information from these interactions can be useful for characterizing the composition a morphology of the substrate surface.

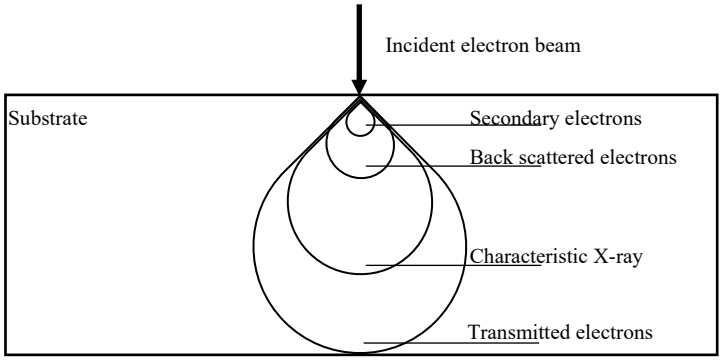

Figure 1-8. Interaction volume of incident electron beam.

1.4.1 Scanning Electron Microscopy (SEM)

Secondary electrons and backscattered electrons are detected in scanning electron microscopy. Secondary electrons are ejected from the surface when it is struck by an incident electron beam. They can be detected at different orientations and thus reveal information about

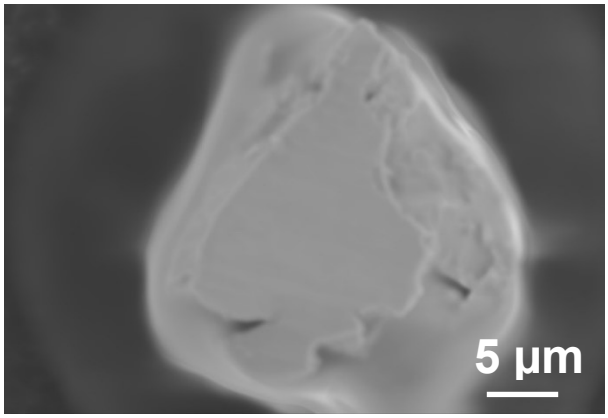

Figure 1-9. Secondary electron image of $Ce_3Rh_{11}Ge_5$.

surface morphology. Because samples must be electrically conducting for these secondary electrons to be detected, they are mounted on conductive carbon tape on an aluminum sample holder. A typical SEM image reveals information about sizes and shapes of crystals (Figure 1-9).

Electrons can also be scattered 180° backwards. These backscattered electrons can also be detected to form an image that reveals information about morphology. Because there is only one direction to detect these electrons, it is difficult to get information about the edges of samples. Normally, arc-melted ingots are mounted on an epoxy mold and their surfaces are polished flat to make it easier to detect backscattered electrons (Figure 1-10). The intensities in the image are proportional to the atomic mass, so heavy elements appear brighter. These backscattered images are helpful in quantifying elemental compositions in a sample.

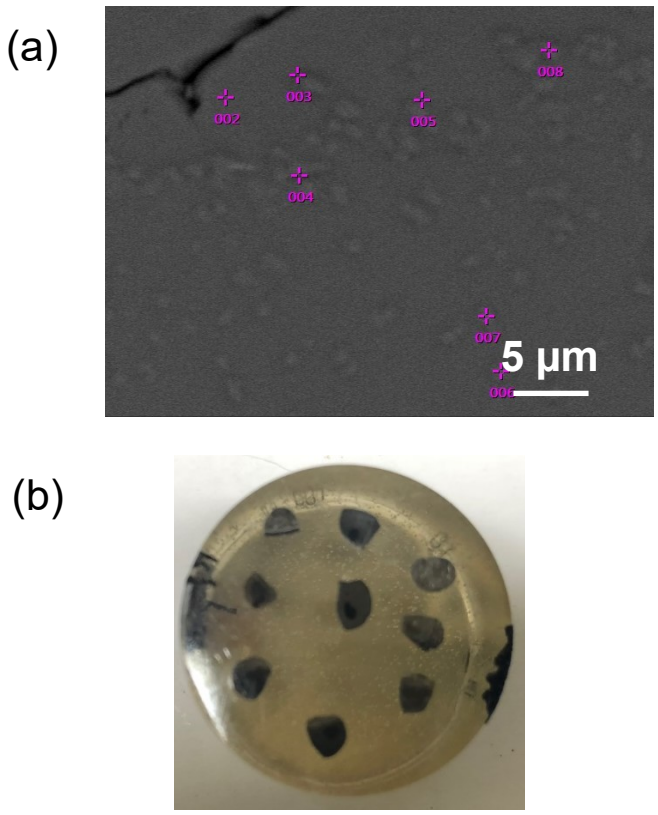

Figure 1-10. (a) Backscattered image of $CeRh_3Ge_2$ with secondary phase. (b) Epoxy mount with polished carbon-coated surface of ingots.

1.4.2 Energy-Dispersive X-ray (EDX) Spectroscopy

In exactly the same way that X-rays are generated in an X-ray tube, they can also be produced when the electron beam in a scanning electron microscope strike the surface of a sample. X-rays that are characteristic of the different elements present in a sample can then be detected to reveal the composition (Figure 1-11).[21] However, the generated X-rays can undergo absorption or may cause fluorescence, and these correction factors need to be taken into account. Light elements (with $Z < 11$) suffer severe absorption effects and are not reliably detected.

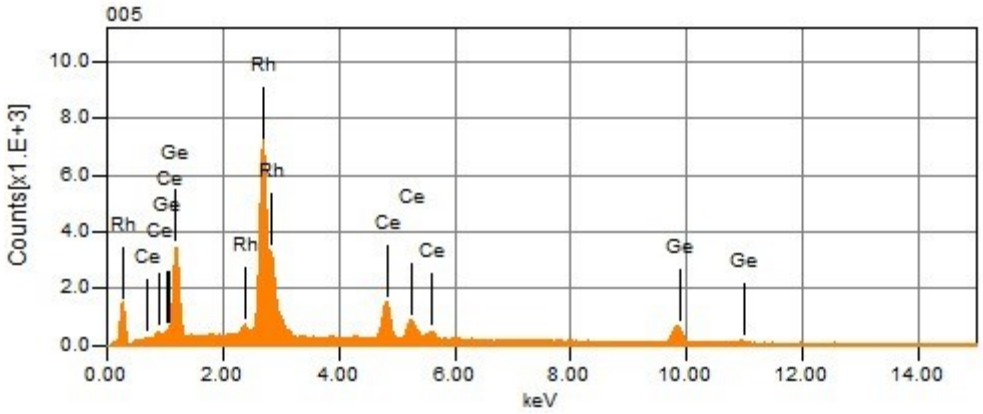

Figure 1-11. An EDX spectrum for sample $CeRh_3Ge_2$.

From the intensities of the peaks, a quantitative analysis can also be performed. It is helpful to perform analyses at different points of a sample to ascertain homogeneity. Although compositions obtained from EDX spectra may show large errors, depending on the application of correction factors, they are still helpful in providing an approximate analysis.

1.5 Electronic Structure Calculations

The electronic structure of solids, which is related to many of their physical properties, results from the interaction of atomic orbitals. The wavefunctions of electrons are evaluated through the Schrödinger equation:[22]

$$\mathcal{H}\psi(\vec{r}) = E\psi(\vec{r})$$

In the tight-binding model, the wavefunctions ψ are expressed as linear combinations of atomic orbitals. Calculations were performed using the tight-binding linear muffin tin orbital (TB-LMTO) program and the Vienna ab initio simulation package.[23] These calculations reveal the density of states (DOS), from which conclusions about electrical conductivity (e.g., metal vs. semiconductor) can be made, and crystal orbital Hamilton population (COHP) curves, which provide information about the nature of bonding between any two specified atoms (Figure 1-12).[24, 25]

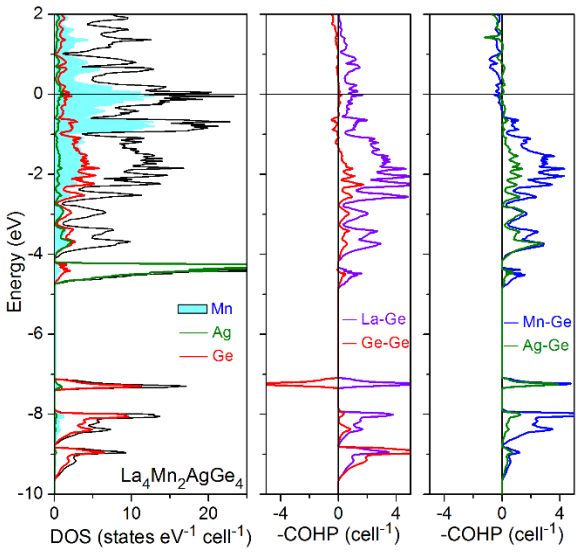

Figure 1-12. DOS and COHP curves for $La_4Mn_2AgGe_4$.

1.6 Thermal Conductivity Measurements

One of the physical property measurements investigated in this thesis is thermal conductivity, which describes how easily heat is transferred within a material through the motion of electrons or phonons (quantized vibrational modes).[26] High thermal conductivity is useful in heat sinks, for example, in electrical devices, while low thermal conductivity is useful in insulation. Thermoelectric materials, which interconvert heat and electricity, require low thermal conductivity. Typically, intermetallic compounds are expected to show high thermal conductivity.

Among various methods to measure thermal conductivity κ, one method is to relate it to density ρ, heat capacity C_p, and thermal diffusivity α:

$$\kappa = \rho C_p \alpha$$

The density can be calculated from the crystal structure. The heat capacity was measured through differential scanning calorimetry (DSC) on a PerkinElmer Pyris 1 instrument. The thermal diffusivity was measured on a Netzsch LFA 457 instrument by using laser flash method (Figure 1-13).[27]

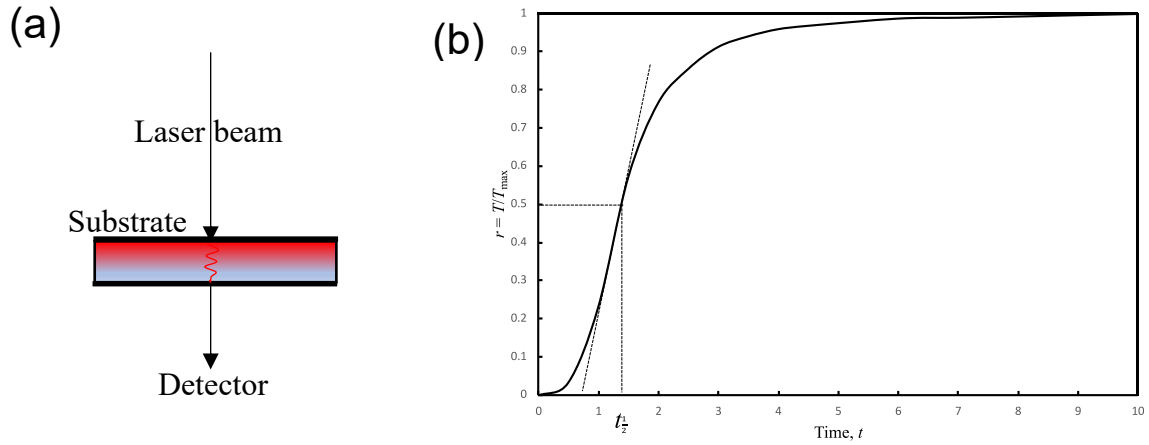

Figure 1-13. (a) Schematic for thermal diffusivity measurement method. (b) Diffusivity model for ideal sample.

The samples were coated with graphite to optimize radiation emission and absorption. A laser beam strikes one side, and the temperature on the other side is monitored until it equilibrates. The temperature is measured as a function of time and the thermal diffusivity is calculated from:

$$\alpha = 1.38 \frac{L^2}{\pi^2 t_{\frac{1}{2}}}$$

where L is the thickness of the sample.[28]

1.7 Research Motivation

Germanides are a large class of intermetallic compounds that have been well studied in the past because of interest in their structures and physical properties, such as magnetism and superconductivity, especially in those compounds containing rare-earth and transition metals. Although ternary *RE–M*–Ge systems are well known with 13026 of identified compounds with 1095 structure types, the Ce–Rh–Ge system is far from complete, and the Rh-rich region has not been thoroughly investigated.[29] The goal is to explore this region to see if ternary Rh-rich phases are present. Another goal is to study the far less investigated quaternary *RE–M–M′*–Ge systems, where only several hundred are known.[29] Previously, the series $RE_4M_2InGe_4$ was identified but it is of interest to see if further substitution can be carried out, particularly for the unusual In site. It is considerably harder to synthesize and characterize these quaternary compounds because of complications with formation of multiple phases and the possibility for disorder of sites. Clarifying the existence of other related quaternary compounds may help us develop trends to understand structure-property relationships.

1.8 References

1. Cinca, N.; Lima, C. R. C.; Guilemany, J. M. An overview of intermetallics research and application: Status of thermal spray coatings. *J. Mater. Res. Technol.* **2013**, *2*, 75–86.
2. Huang, W. M.; Ding, Z.; Wang, C. C.; Wei, J.; Zhao, Y.; Purnawali, H. Shape memory materials. *Mater. Today.* **2010**, *13*, 54–61.
3. Miyazaki, S.; Duerig, T. W.; Melton, K. N. *Engineering Aspects of Shape Memory Alloys*; Butterworth: London, 1990.
4. Lipscomb, I. P.; Nokes, L. D. *The Application of Shape Memory Alloys in Medicine*; Wiley-Blackwell: Sullfork, 1996.

5. Matthias, B. T.; Geballe, T. H.; Geller, S.; Corenzwit, E. Superconductivity of Nb_3Sn. *Phys. Rev.* **1954**, *95*, 1435–1435.

6. Kunzler, J. E.; Buehler, E.; Hsu, F. A.; Wernick, J. H. Superconductivity in Nb_3Sn at high current density in a magnetic field of 88 kgauss. *Phys. Rev. Lett.* **1961**, *6*, 89–91.

7. Han, M. K.; Jin, Y.; Lee, D. H.; Kim, S. J. Thermoelectric properties of Bi_2Te_3: CuI and the effect of its doping with Pb atoms. *Materials*. **2017**, *10*, 1235-1–1235-10.

8. Koehler, W. C. Magnetic properties of rare‐earth metals and alloys. *J. Appl. Phys.* **1965**, *36*, 1078–1087.

9. Szlawska, M.; Majewicz, M.; Kaczorowski, D. Ferromagnetic ordering in single-crystalline U_2RhSi_3 with fully ordered crystal structure. *J. Alloys Compd.* **2016**, *662*, 208–212.

10. Petrovic, C.; Pagliuso, P. G.; Hundley, M. F.; Movshovich, R.; Sarrao, J. L.; Thompson, J. D.; Fisk, Z.; Monthoux, P. Heavy-fermion superconductivity in $CeCoIn_5$ at 2.3 K. *J. Phys. Cond. Mat.* **2001**, *13*, L337–L342.

11. Steglich, F.; Aarts, J.; Bredl, C. D.; Lieke, W.; Meschede, D.; Franz, W.; Schäfer, H. Superconductivity in the presence of strong pauli paramagnetism: $CeCu_2Si_2$. *Phys. Rev. Lett*. **1979**, *43*, 1892–1896.

12. Smigelskas, A. D.; Kirkendall, E. O. Zinc diffusion in alpha brass. *Trans. AIME* **1947**, *171*, 130–142.

13. Schenk, P.; Brauer, G. *Handbook of Preparative Inorganic Chemistry*, 2nd ed.; Academic Press: London, 1963.

14. Moore, D. M.; Reynolds, R. C. *X-ray Diffraction and the Identification and Analysis of Clay Minerals*; Oxford University Press: Oxford, 1989.

15. Ladd, M.; Palmer, R. *Structure Determination by X-ray Crystallography*, 5th ed.; Springer: New York, 2013.

16. West, A. R. *Basic Solid State Chemistry*, 2nd ed.; Wiley: New York, 1999.

17. Eckert, M. Max von Laue and the discovery of X-ray diffraction in 1912. *Ann. Phys.* **2012**, *524*, A83–A85.

18. Bragg, W. H.; Bragg, W. L. The reflection of X-rays by crystals. *Proc. Royal. Soc. A* **1913**, *88*, 428–438.

19. Massa, W. *Crystal Structure Determination*, 2nd ed.; Springer: Berlin, 2004.

20. Goldstein, J. I.; Newbury, D. E.; Echlin, P.; Joy, D. C.; Fiori, C.; Lifshin, E. *Scanning Electron Microscopy and X-Ray Microanalysis*, 3rd ed.; Springer: New York, 2003.

21. Russ, J. C. *Fundamentals of Energy Dispersive X-ray Analysis*; Butterworth: London, 1984.

22. Dronskowski, R. *Computational Chemistry of Solid State Materials*; Wiley-VCH: Weinheim and New York, 2005.

23. Tank, R.; Jepsen, O.; Burkhardt, A.; Andersen, O. K. *TB-LMTO-ASA Program*, version 4.7; Max Planck Institut für Festkörperforschung: Stuttgart, Germany, 1998.

24. Dronskowski, R.; Blöchl, P. E. Crystal orbital Hamilton populations (COHP): Energy-resolved visualization of chemical bonding in solids based on density-functional calculations. *J. Phys. Chem*. **1993**, *97*, 8617–8624.

25. Zhang, D.; Oliynyk, A. O.; Duarte, G. M.; Iyer, A. K.; Ghadbeigi, L.; Kauwe, S. K.; Sparks, T. D.; Mar, A. Not just par for the course: 73 quaternary germanides RE_4M_2XGe$_4$ (*RE* = La–Nd, Sm, Gd–Tm, Lu; *M* = Mn–Ni; *X* = Ag, Cd) and the search for intermetallics with low thermal conductivity. *Inorg. Chem.* **2018**, *57*, 14249–14259.

26. Berman, R. The thermal conductivity of dielectric solids at low temperatures. *Adv. Phys.* **1953**, *2*, 103–140.

27. Cape, J. A.; Lehman, G. W. Temperature and finite pulse-time effects in the flash method for measuring thermal diffusivity. *J. Appl. Phys.* **1963**, *34*, 1909–1913.

28. Parker, W. J.; Jenkins, R. J.; Butler, C. P.; Abbott, G. L. Flash method of determining thermal diffusivity, heat capacity, and thermal conductivity. *J. Appl. Phys.* **1961**, *32*, 1679–1684.

29. Steurer, W.; Dshemuchadse, J. *Intermetallics: Structures, Properties, and Statistics*; Oxford University Press: Oxford, 2016.

Chapter 2 Ternary Rh-rich Germanides in the Ce–Rh-Ge System

2.1 Introduction

Although ternary rare-earth transition-metal germanides *RE*–*M*–Ge have been well studied because of their diverse structures and physical properties, they have largely been limited to *M* components from the first-row or late d-block transition metals. When *M* is a precious metal (Ru, Os, Rh, Ir, Pd, Pt), some common compositions of ternary germanides are frequently encountered. They include superconductors ($La_2Rh_3Ge_5$, T_c = 4.4 K, and $Y_2Ir_3Ge_5$, T_c = 2.5 K) and potential thermoelectric materials ($RE_3Ru_4Ge_{13}$, which shows a positive Seebeck coefficient of 40 μV K^{-1}).[1–3] Phase diagram investigations have been conducted for some of these ternary systems, but they are often incomplete. For example, studies of the Sm–Rh–Ge, Ce–Pd–Ge, and Ce–Ru–Ge systems have been limited to low concentrations of the precious metal, probably because of their material cost.[4–6]

The Ce–Rh–Ge system is an interesting one that has been studied over many years, but surprisingly our understanding of it is still far from complete. In the first attempt in 1993 to construct the phase diagram, Shapiev identified more than 20 ternary phases in his dissertation, but for many of them, full structural characterization is lacking.[7] Ternary phases in this system include CeRhGe (antiferromagnetic with T_N = 9.3 K), $CeRhGe_3$ (antiferomagnetic with three transitions below 14.6 K), and $CeRhGe_2$ (antiferromagnetic with T_N = 7.6 K and superconducting at T_c = 0.45 K at 7.1 GPa).[8–10] The structures of these ternary phases typically consist of Rh–Ge networks built from trigonal prisms, with Ce atoms located with large cages. Most of the well characterized phases have high Ce or Ge content, whereas the existence of those having high Rh content is not clear. To extend this study started over two decades ago, we re-examine here several ternary phases in the Rh-rich region of the Ce–Rh–Ge system at 800 °C.

2.2 Experimental

2.2.1 Synthesis

Starting materials were freshly filed Ce pieces (99.9%, Hefa), Rh powder (99.99%, Alfa), and Ge powder (99.9%, Sigma-Aldrich). Mixtures of these elements were weighed to the desired stoichiometry with a total mass of 0.2 g and pressed into 6-mm-diameter pellets. They were arc-melted twice on a water-cooled copper hearth within an argon-filled chamber of a Centorr 5TA tri-arc furnace. Mass losses after arc-melting were less than 1%. The arc-melted ingots were then placed within evacuated and sealed fused-silica tubes, which were heated at 800 °C for 10 d and then quenched in cold water.

2.2.2 Structure Determination

Irregularly shaped grey single crystals were selected from the samples with nominal compositions $Ce_3Rh_{11}Ge_5$, $CeRh_5Ge_3$, and $CeRh_3Ge_2$. Intensity data were collected on a Bruker PLATFORM diffractometer equipped with a SMART APEX II CCD detector and a graphite-monochromated Mo *K*α radiation source, using ω scans at 6−8 different ϕ angles with a frame width of 0.3° and an exposure time of 30 s per frame. Structure solution and refinement were carried out with use of the SHELXTL suite of programs.[11] The refinements generally proceeded in a straightforward fashion. However, in some cases, residual electron density remained near Ce and Rh atoms, likely as a result of artefacts from absorption problems. Face-indexed absorption correction is applied for $Ce_3Rh_{11}Ge_5$ and $CeRh_5Ge_3$, while a multi-scan absorption correction is applied for $CeRh_3Ge_2$. Both correction methods are useful in crystal solving. Face index Crystal data are summarized in Table 2-1.

Table 2-1. Crystallographic Data for $Ce_3Rh_{11}Ge_5$, $CeRh_5Ge_3$, and $CeRh_3Ge_2$.

formula	$Ce_3Rh_{11}Ge_5$	$CeRh_5Ge_3$	$CeRh_3Ge_2$

formula mass (g mol^{-1})	1842.73	872.44	594.03
space group	$P6_3/mmc$ (No. 194)	$P6_3/m$ (No. 176)	$Fmmm$ (No. 69)
a (Å)	8.6964(12)	22.8480(11)	7.392(6)
b (Å)	8.6964(12)	22.8480(11)	11.341(9)
c (Å)	9.2209(12)	3.9208(2)	19.661(16)
V (Å^3)	603.92(18)	1772.56(19)	1648(2)
Z	2	6	16
ρ_{calc} (g cm^{-3})	10.133	4.904	9.576
T (K)	296(2)	296(2)	296(2)
crystal dimensions (mm^3)	0.054×0.037×0.024	0.068×0.044×0.042	0.01×0.01×0.01 (estimated)
radiation		Mo $K\alpha$, λ = 0.71073 Å	
μ(Mo $K\alpha$) (mm^{-1})	35.339	18.004	36.724
transmission factors	0.299–0.523	0.442–0.598	0.553–0.747
2θ limits	5.41–66.15°	3.57–66.33°	4.14–66.22°
data collected	$-13 \le h \le 13$, $-13 \le k \le 13$, $-14 \le l \le 14$	$-35 \le h \le 35$, $-35 \le k \le 35$, $-5 \le l \le 5$	$-11 \le h \le 11$, $-17 \le k \le 17$, $-30 \le l \le 30$
no. of data collected	17438	52594	8627
no. of unique data, including $F_o^2 < 0$	478	2514	897
no. of unique data, with $F_o^2 > 2\sigma(F_o^2)$	478	2514	897
no. of variables	26	111	40
$R(F)$ for $F_o^2 > 2\sigma(F_o^2)$ [a]	0.0307	0.0649	0.0737
$R_w(F_o^2)$ [b]	0.0792	0.2053	0.1857
goodness of fit	1.133	1.056	0.916
$(\Delta\rho)_{max}$, $(\Delta\rho)_{min}$ (e Å^{-3})	5.911, –5.709	26.607, –4.825	3.969, –8.473

[a] $R(F) = \sum||F_o| - |F_c|| / \sum|F_o|$ for $F_o^2 > 2\sigma(F_o^2)$. [b] $R_w(F_o^2) = [\sum[w(F_o^2 - F_c^2)^2] / \sum wF_o^4]^{1/2}$; $w^{-1} = [\sigma^2(F_o^2) + (Ap)^2 + Bp]$, where $p = [\max(F_o^2,0) + 2F_c^2] / 3$.

Powder X-ray diffraction (XRD) patterns of ground samples were collected on an Inel diffractometer equipped with a curved position-sensitive detector (CPS 120) and a Cu $K\alpha_1$ radiation source operated at 40 kV and 20 mA. The patterns were refined with Pawley fitting using

the TOPAS Academic software package (Figure 2-1).[12] Refinement results are summarized in Table 2-2.

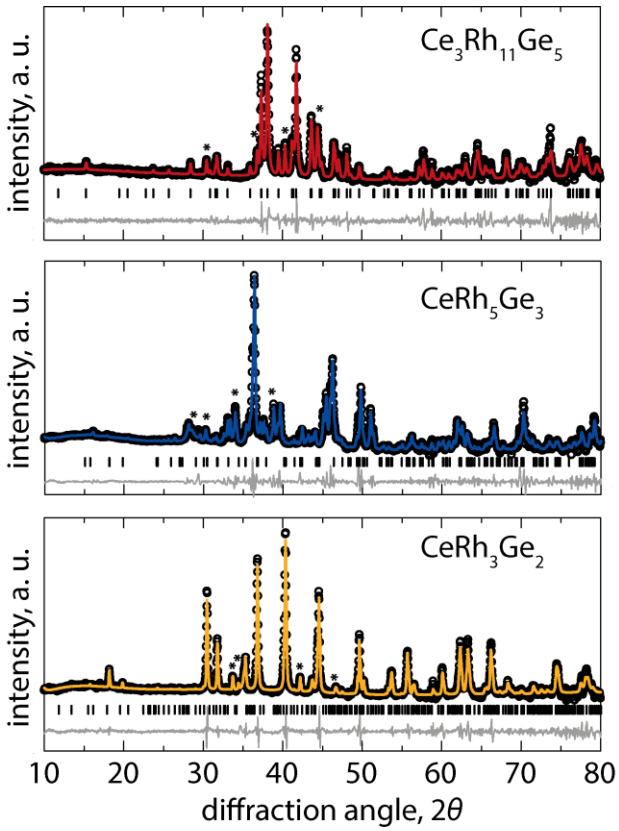

Figure 2-1. Pawley refinement of $Ce_3Rh_{11}Ge_5$, $CeRh_5Ge_2$, and $CeRh_3Ge_2$ samples. Black circles are data points, coloured solid lines are fits, grey lines are difference plots, and asterisks mark peaks from other phases.

Table 2-2. Crystallographic Data for Samples Refinement.

sample	$Ce_3Rh_{11}Ge_5$	$CeRh_5Ge_3$	$CeRh_3Ge_2$
space group	*P6₃/mmc* (No. 194)	*P6₃/m* (No. 176)	*Fmmm* (No. 69)
a (Å)	8.6508(7)	22.8455(12)	7.3402(6)
b(Å)	8.6508(7)	22.8455(12)	11.2573(12)
c (Å)	9.1174(10)	3.9214(4)	19.5644(17)
2θ limits	10.00–80.00°	10.00–80.00°	10.00–80.00°
no. of data collected	2414 data points	2414 data points	2414 data points
no. of Bragg reflections	89	442	158
no. of variables	20	20	21
residuals	R_{wp} = 0.1108	R_{wp} = 0.0849	R_{wp} = 0.1691

2.2.3 SEM and EDX Analysis

Elemental analysis was carried out on selected crystals and polished samples by energy-dispersive X-ray (EDX) analysis on a JEOL JSM-6010LA InTouchScope scanning electron microscope (SEM), operated with accelerating voltage of 20 kV and acquisition time of 70 s (Figure 2-2). The compositions were within 2% of expected values. The crystal shown for $Ce_3Rh_{11}Ge_5$ has the expected composition. The polished $CeRh_5Ge_3$ sample shows a predominant gray area that corresponds to the desired phase, but there are embedded dark areas that give a different composition of $Ce_{0.23}Rh_{0.62}Ge_{0.15}$. The polished $CeRh_3Ge_2$ sample shows a uniform grey area corresponding to the desired phase, with smaller regions that appear to have lower Rh and higher Ge content.

2.2.4 Electronic Calculations

First-principles calculations were performed using the Vienna ab initio simulation package (VASP), and included total energy, density of state, electron localization functions, and chemical-bonding analyses with Bader charge theory.[13–18] A plain-wave basis set with projector-augmented-wave potentials and a cut-off energy of 500 eV were applied. A Monkhorst-Pack *k*-point grid (8 × 8 × 8 for $Ce_3Rh_{11}Ge_5$, 4 × 4 × 12 for $CeRh_5Ge_3$, and 10 × 8 × 4 for $CeRh_3Ge_2$) was used. The convergence criteria were set to 1×10^{-8} eV for electronic optimization and 1×10^{-6} eV for structure optimization. The potentials for Ce atoms were replaced by those for La, to avoid complications associated with f-electrons.

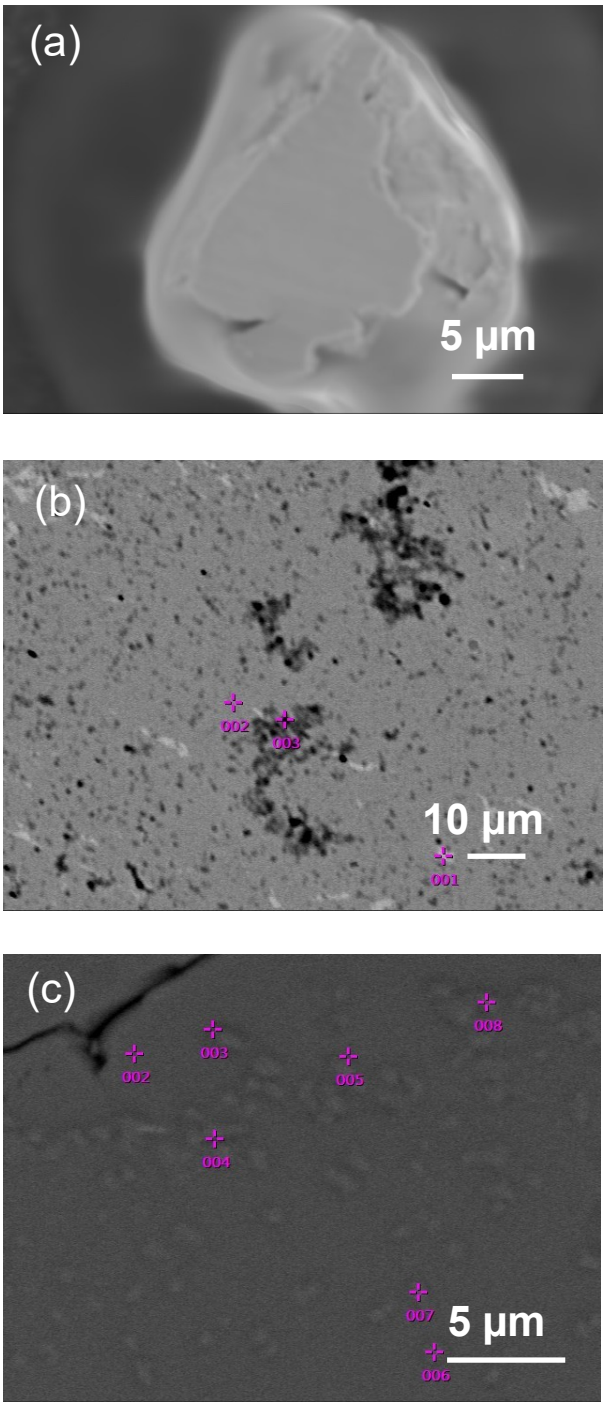

Figure 2-2. Representative SEM images for (a) $Ce_3Rh_{11}Ge_5$, (b) $CeRh_5Ge_3$, (c) $CeRh_3Ge_2$.

2.3 Results and Discussion

$Ce_3Rh_{11}Ge_5$, $CeRh_5Ge_3$, and $CeRh_3Ge_2$ were found to be thermodynamically stable phases within the Ce–Rh–Ge system at 800 °C.

$Ce_3Rh_{11}Ge_5$ adopts the hexagonal $Sc_3Ni_{11}Ge_4$-type structure, which is closely related to the $Gd_3Al_{12}Ru_4$-type structure.[19, 20] These two structure types differ in the occupation of sites 2*a* (0, 0, 0) and 2*b* (0, 0, 0.25) located along the *c*-axis. In the defect structure of $Sc_3Ni_{11}Ge_4$, the 2*a* and 2*b* sites both contain Ge atoms, but they must be partially occupied because the 2.1–2.2 Å distance between these sites is too short for Ge–Ge bonds.[20, 21] In the ordered structure of $Gd_3Al_{12}Ru_4$, these sites are fully occupied by Ru atoms in 2*a* and Al atoms in 2*b*, because the short distance of 2.37 Å is consistent with Ru–Al distances.[20] It is not clear which model – one that contains Ge atoms partially occupying both sites, or one that contains Rh and Ge atoms fully occupying both sites – is correct for $Ce_3Rh_{11}Ge_5$. Close inspection of the electron density map reveals that the electron density is equally distributed over both sites (Figure 2-3), favouring a model containing Ge atoms in both sites. However, the electron density of the Ge sites at 6*g*, which are fully occupied, is similar in magnitude to those at the 2*a* and 2*b* sites. This implies that the 2*a* and 2*b* sites are also fully occupied by Ge atoms. The distance between these sites is 2.31 Å, which is at the lower limits for Ge–Ge contacts, as seen previously in structures of other germanides.[22–24] Thus $Ce_3Rh_{11}Ge_5$ differs from $Sc_3Ni_{11}Ge_4$ in having fully occupied 2*a* and 2*b* sites. Table 2-3 lists atomic coordinates and Table 2-4 lists interatomic distances in $Ce_3Rh_{11}Ge_5$.

Table 2-3. Atomic Coordinates and Bader Charge Analysis for $Ce_3Rh_{11}Ge_5$.

atom	Wyckoff position	*x*	*y*	*z*	U_{eq} (Å^2) [a]	charge per atom
Ce	6*h*	0.18969(6)	0.37938(11)	1/4	0.0120(2)	1.38+
Rh1	12*k*	0.15935(5)	0.31869(10)	0.58765(9)	0.0106(2)	0.40–

Rh2	6*h*	0.55785(7)	0.11570(13)	1/4	0.0094(2)	0.60–
Rh3	4*f*	1/3	2/3	0.00231(16)	0.0099(2)	0.41–
Ge1	6*g*	1/2	0	0	0.0089(3)	0.19+
Ge2	2*b*	0	0	1/4	0.0121(5)	0.14–
Ge3	2*a*	0	0	0	0.0265(9)	0.28–

[a] U_{eq} is defined as one-third of the trace of the orthogonalized U_{ij} tensor.

Table 2-4. Selected Interatomic Distances (Å) in $Ce_3Rh_{11}Ge_5$.

Ce–Ge2	2.8572(9)	Rh1–Rh1 (×2)	2.8938(11)
Ce–Rh2	2.9666(9)	Rh1–Rh1	2.9940(17)
Ce–Rh2	2.9667(9)	Rh1–Rh2 (×2)	2.7386(7)
Ce–Rh1 (×4)	3.0509(7)	Rh1–Rh3	2.7488(9)
Ce–Rh1 (×2)	3.1468(9)	Rh2–Ge1 (×2)	2.4644(5)
Ce–Rh3 (×2)	3.1460(12)	Rh2–Rh2 (×2)	2.8390(18)
Ce–Ge1	3.2964(4)	Rh2–Rh3 (×2)	2.8459(14)
Rh1–Ge3	2.5326(8)	Rh3–Ge1 (×3)	2.5105(4)
Rh1–Ge2 (×2)	2.6916(6)	Ge2–Ge3 (×2)	2.3052(3)

The structure of $Ce_3Rh_{11}Ge_5$ can be visualized in terms of Ge atoms forming tunnels of stacked trigonal prisms, three quarters of which are alternately filled by Ce atoms and Rh–Rh dumbbells and one quarter of which are alternately filled by Ce atoms and Rh_5 trigonal bipyramids (Figure 2-3).[25–27] A different description focuses on stacking of two layers of $[Ce_3Rh_3Ge_3]$ and two layers of $[Rh_4Ge_8]$.[20] The electron localization function shows high values along the *c*-direction, with particularly high concentrations at the Ge2 atom located at 0, 0, ¼ (Figure 2-4).

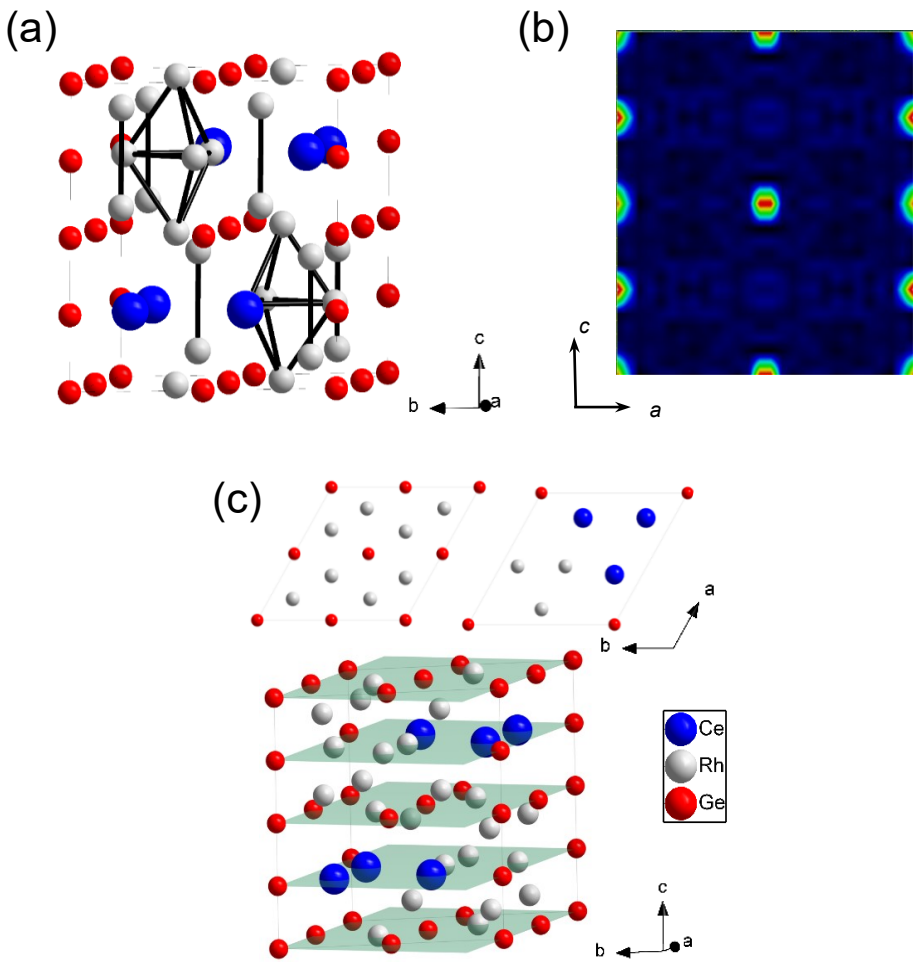

Figure 2-3. (a) $Ce_3Rh_{11}Ge_5$ in terms of Rh_2 dumbbells and [Rh_5] trigonal bipyramids. (b) Electron density map on *bc* plane. (c) Stacked layers of [$Ce_3Rh_3Ge_3$] and [Rh_4Ge_8].

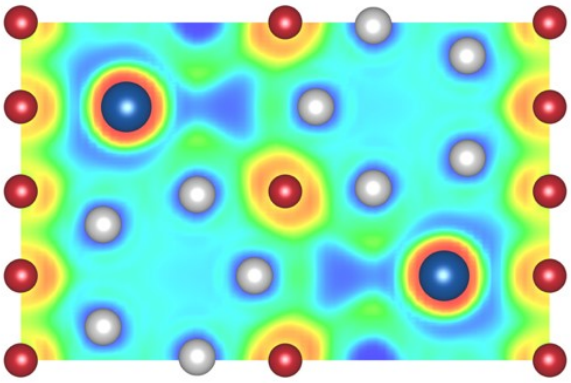

Figure 2-4. Electron localization function for $Ce_3Rh_{11}Ge_5$ on (1 1 0) plane, with Ge atoms aligned along the *c*-direction (vertical).

The structure of $Ce_3Rh_{11}Ge_5$ is also hexagonal, with atomic coordinates listed in Table 2-5 and distances listed in Table 2-6.

Table 2-5. Atomic Coordinates and Bader Charge Analysis for $CeRh_5Ge_3$.

atom	Wyckoff position	*x*	*y*	*z*	U_{eq} (Å^2) [a]	charge per atom
Ce1	6*h*	0.6159(1)	0.1349(1)	1/4	0.0082(2)	1.50+
Ce2	6*h*	0.2673(1)	0.0360(1)	1/4	0.0088(2)	1.50+
Rh1	6*h*	0.0414(1)	0.5487(1)	1/4	0.0057(3)	0.51–
Rh2	6*h*	0.1018(1)	0.0077(1)	1/4	0.0132(3)	0.22–
Rh3	6*h*	0.1398(1)	0.2971(1)	1/4	0.0069(3)	0.53–
Rh4	6*h*	0.1014(1)	0.3952(1)	1/4	0.0059(3)	0.51–
Rh5	6*h*	0.2005(1)	0.1443(1)	1/4	0.0065(3)	0.54–
Rh6	6*h*	0.2538(1)	0.6076(1)	1/4	0.0064(3)	0.48–
Rh7	6*h*	0.3531(1)	0.3567(1)	1/4	0.0062(3)	0.51–
Rh8	6*h*	0.4070(1)	0.2049(1)	1/4	0.0070 (3)	0.39–
Rh9	6*h*	0.4459(1)	0.1040(1)	1/4	0.0067(3)	0.39–
Rh10	6*h*	0.5469(1)	0.2441(1)	1/4	0.0064(3)	0.38–
Ge1	2*d*	0.6667	0.3333	1/4	0.0065(6)	0.25+
Ge2	6*h*	0.0148(1)	0.4298(1)	1/4	0.0056(4)	0.27+
Ge3	6*h*	0.1121(1)	0.1778(1)	1/4	0.0074(4)	0.18+
Ge4	6*h*	0.2220(1)	0.4868(1)	1/4	0.0073(4)	0.18+
Ge5	6*h*	0.2617(1)	0.3864(1)	1/4	0.0077(4)	0.24+
Ge6	6*h*	0.3192(1)	0.2357(1)	1/4	0.0061(4)	0.19+
Ge7	2*c*	0.3626(1)	0.5260(1)	1/4	0.0067(4)	0.43+

[a] U_{eq} is defined as one-third of the trace of the orthogonalized U_{ij} tensor.

Table 2-6. Selected Interatomic Distances (Å) in $CeRh_5Ge_3$.

Ce1–Ge4 (×2)	3.1331(16)	Rh4–Ge6 (×2)	2.5129(14)
Ce1–Rh6 (×2)	3.1334(13)	Rh4–Rh7 (×2)	2.8672(14)
Ce1–Ge7 (×2)	3.1324(16)	Rh4–Rh8 (×2)	2.9301(14)
Ce1–Ge2 (×2)	3.1527(16)	Rh5–Rh6	2.460(2)
Ce1–Rh4 (×2)	3.2059(13)	Rh5–Ge3	2.492(2)
Ce1–Rh1 (×2)	3.2104(13)	Rh5–Ge3 (×2)	2.5310(14)

Ce2–Ge5 (×2)	2.1357(16)	Rh6–Ge4	2.478(2)
Ce2–Ge6 (×2)	3.1384(16)	Rh6–Ge7	2.479(2)
Ce2–Ge3 (×2)	3.1425(17)	Rh6–Ge1 (×2)	2.5521(9)
Ce2–Rh7 (×2)	3.1737(13)	Rh6–Rh6	2.830(2)
Ce2–Rh3 (×2)	3.1776(13)	Rh6–Rh6	2.830(2)
Ce2–Rh5 (×2)	3.2033(13)	Rh6–Rh10 (×2)	2.9227(14)
Rh1–Ge2	2.468(2)	Rh7–Ge6	2.472(2)
Rh1–Ge7	2.494(2)	Rh7–Ge5	2.492(2)
Rh1–Ge2 (×2)	2.5231(14)	Rh7–Ge2 (×2)	2.5210(14)
Rh1–Rh7	2.7786(19)	Rh7–Rh9 (×2)	2.9290(14)
Rh1–Rh1 (×2)	2.8573(19)	Rh8–Ge6	2.435(2)
Rh1–Rh9 (×2)	2.9268(14)	Rh8–Ge4 (×2)	2.5572(15)
Rh2–Ge3	2.433(2)	Rh8–Ge5 (×2)	2.5616(15)
Rh2–Ge3 (×2)	2.5133(16)	Rh8–Rh10	2.855(2)
Rh2–Rh5	2.791(2)	Rh8–Rh9	2.8553(19)
Rh2–Rh5 (×2)	2.8876(15)	Rh9–Ge2	2.440(2)
Rh2–Rh2 (×3)	2.9782(13)	Rh9–Ge7 (×2)	2.5591(15)
Rh2–Ge2 (×2)	2.9783(13)	Rh9–Ge5 (×2)	2.5611(15)
Rh3–Ge3	2.470(2)	Rh9–Rh10	2.8608(19)
Rh3–Ge5	2.496(2)	Rh10–Ge1	2.4630(13)
Rh3–Ge6 (×2)	2.5303(14)	Rh10–Ge7 (×2)	2.5681(15)
Rh3–Rh4	2.7853(19)	Rh10–Ge4 (×2)	2.5694(15)
Rh3–Rh5 (×2)	2.8549(14)	Ge4–Ge5	2.857(3)
Rh3–Rh8 (×2)	2.9331(14)	Ge4–Ge7	2.872(3)
Rh4–Ge2	2.472(2)	Ge5–Ge7	2.853(3)
Rh4–Ge4	2.491(2)		

$CeRh_5Ge_3$ adopts the hexagonal $SmRh_5Ge_3$-type structure, which is also known as the UCo_5Si_3-type structure.[28–30] It has a large unit cell containing isolated columns of confacial $[Rh_6Ge_6]$ hexagonal prisms centred by Ce atoms (Figure 2-5).

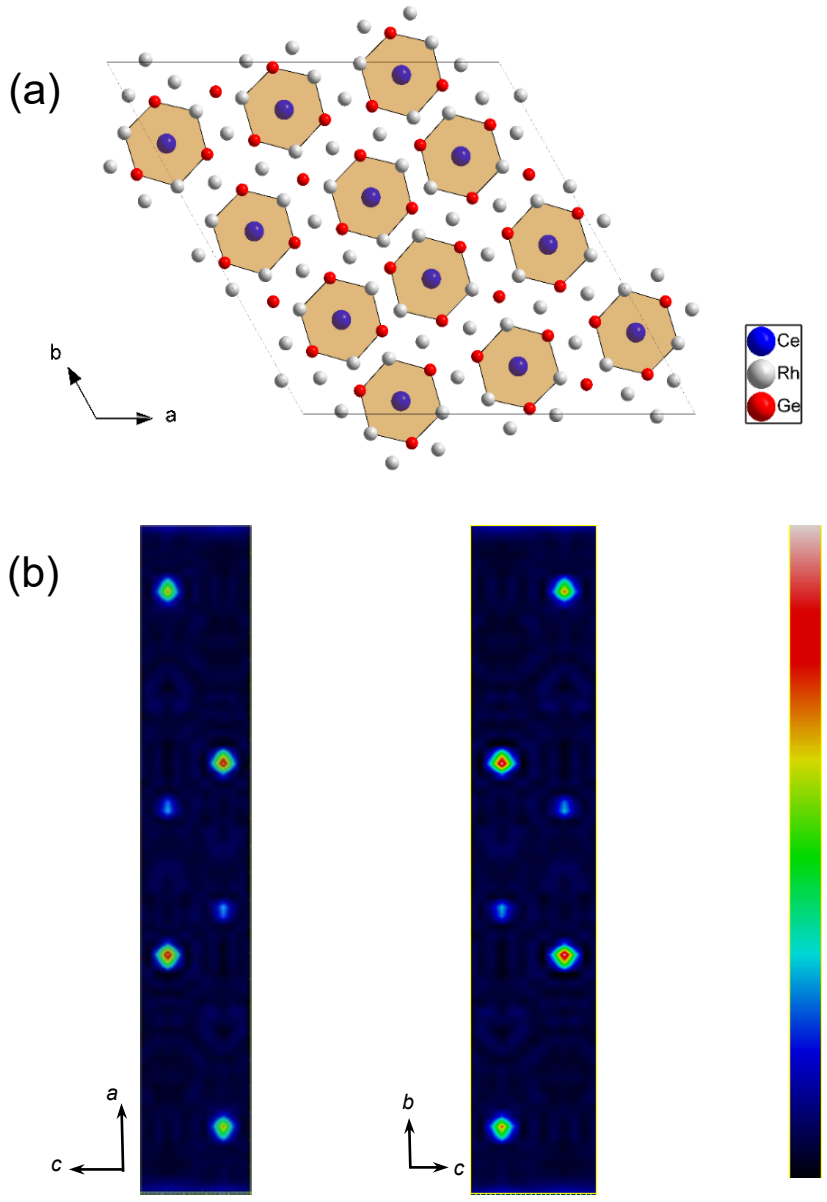

Figure 2-5. (a) Structure of $CeRh_5Ge_3$ highlighting $[CeRh_6Ge_6]$ polyhedra. (b) Electron density map viewed down the *b*-axis (left) and *a*-axis (right).

Some residual electron density is found at 2*b* (0, 0, 1/4), but introduction of lightest atom (Ge) does not improve the model, with the displacement parameters becoming too large to be meaningful. This electron density is about 10% that of the heaviest atom (Ce) and is located too close (2.0 Å) to neighbouring atoms to be physically meaningful; it is probably an artefact from absorption effects. The electron localization function reveals bonding interactions between positively charge Ce atoms with negatively charged Rh atoms (Figure 2-6).

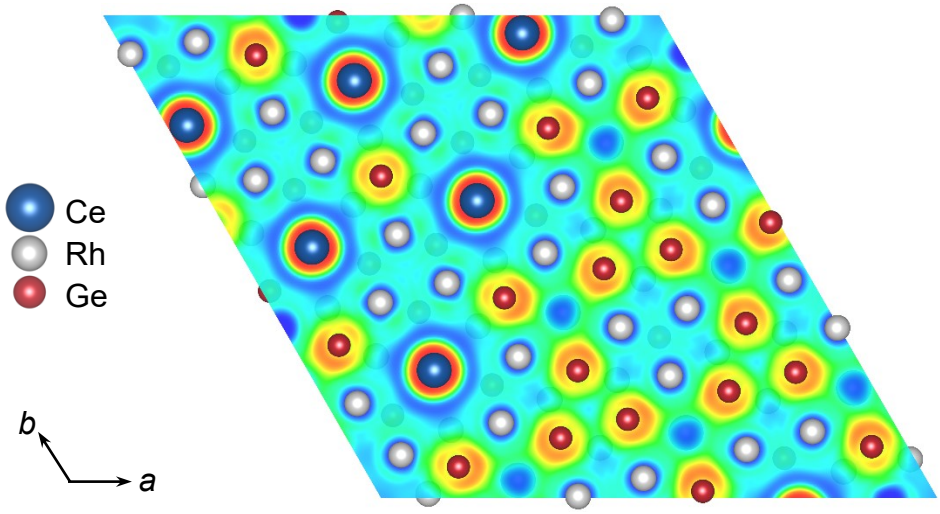

Figure 2-6. Electron localization function for $CeRh_5Ge_3$ parallel to (0 0 1) plane, showing layers of atoms.

$CeRh_3Ge_2$ adopts an orthorhombic structure, with atomic positions listed in Table 2-7 and interatomic distances in Table 2-8.

Table 2-7. Atomic Coordinates and Bader Charge Analysis for $CeRh_3Ge_2$.

atom	Wyckoff position	*x*	*y*	*z*	U_{eq} (Å^2) [a]	charge per atom
Ce1	8*i*	0	0	0.26103(17)	0.0174(9)	1.52+
Ce2	8*h*	0	0.2386(3)	0	0.0246(11)	1.54+

Rh1	32*p*	0.2684(2)	0.1251(4)	0.1250(2)	0.0187(5)	0.62–
Rh2	8*g*	0.2179(6)	0	0	0.0092(8)	0.62–
Rh3	8*f*	1/4	1/4	1/4	0.0266(16)	0.63–
Ge1	16*m*	0	0.2359(4)	0.1666(4)	0.0295(15)	0.18+
Ge2	8*i*	0	0	0.0947(2)	0.0173(14)	0.16+
Ge3	8*i*	0	0	0.4287(3)	0.0137(12)	0.13+

[a] U_{eq} is defined as one-third of the trace of the orthogonalized U_{ij} tensor.

Table 2-8. Selected Interatomic Distances (Å) in $CeRh_3Ge_2$.

Ce1–Rh1 (×4)	3.169(5)	Rh1–Ge1	2.467(5)
Ce1–Ge1 (×2)	3.246(6)	Rh1–Ge1	2.488(5)
Ce1–Ge2	3.252(7)	Rh1–Ge2	2.511(4)
Ce1–Ge3	3.314(7)	Rh1–Rh1	2.837(10)
Ce1–Ge1 (×2)	3.324(6)	Rh1–Rh3	2.841(5)
Ce1–Rh3 (×2)	3.390(2)	Rh1–Rh1	2.847(10)
Ce2–Rh2 (×2)	3.150(4)	Rh1–Rh2	2.861(5)
Ce2–Ge1 (×2)	3.276(7)	Rh2–Ge2 (×2)	2.462(5)
Ce2–Ge3 (×2)	3.279(4)	Rh2–Ge3 (×2)	2.513(5)
Ce2–Ge2 (×2)	3.285(4)	Rh3–Ge1 (×4)	2.475(5)
Ce2–Rh1 (×4)	3.370(4)	Ge3–Ge3	2.804(10)
Rh1–Ge3	2.460(4)		

The structure of $CeRh_3Ge_2$ contains hexagonal coordination environments around the Ce atoms, similar to those found in $CeRh_6Ge_4$ (space group $P\bar{6}m2$).[31] Nevertheless, the true crystal system is not hexagonal, but rather orthorhombic. It is easy to be misled into choosing a hexagonal lattice but in doing so, the intensity data must be integrated as arising from six non-merohedral twins with domains rotated by 60°. Proceeding with this option led to negative displacement parameters for all atoms in the structural model. Instead, the software Cell_now indicated that the lattice can be described as an orthorhombic one without any twin domains,[32] and we believe that

this is the best model. Other related ternary phases in the Ce–Rh–Ge system include orthorhombic ($Ce_2Rh_3Ge_5$, *Ibam*; CeRhGe, *Pnma*) and tetragonal structures ($CeRhGe_3$, *I*4*mm*).[31, 33–35] $CeRh_3Ge_2$ adopts a face-centred orthorhombic structure (*Fmmm*, $Z = 16$) containing a Rh–Ge framework with Ce atoms embedded within (Figure 2-7). There are Rh_6 trigonal prisms centred by Ge atoms that share faces along the *a*-direction and edges within the *bc*-plane. Each Ce atom is coordinated by six Ge atoms. If Rh atoms are included in the coordination environment, two types of polyhedra, [$CeGe_6Rh_8$] and [$CeGe_6Rh_{10}$], build up the structure. Similar to the previous two structures, the electron localization function reveals negatively charge Rh atoms (Figure 2-8).

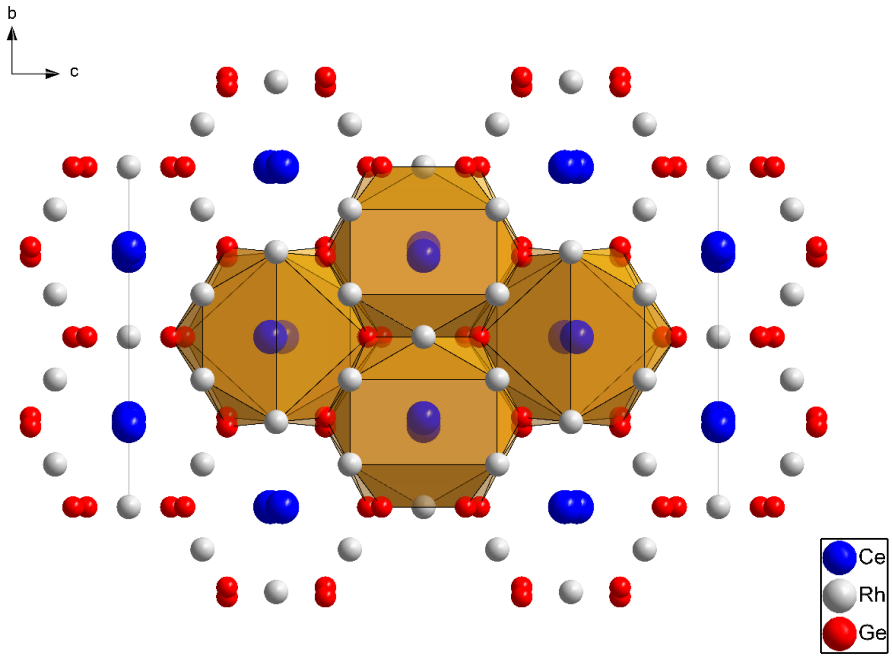

Figure 2-7. Structure of $CeRh_3Ge_2$ with [$CeGe_6Rh_8$] or [$CeGe_6Rh_{10}$] polyhedral.

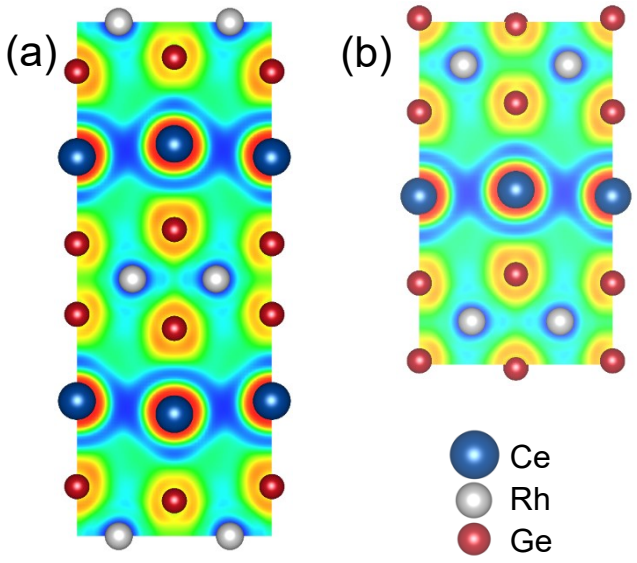

Figure 2-8. Electron localization function for $CeRh_3Ge_2$ at (a) (1 0 1) plane, (b) (0 $\bar{1}$ 3) planes.

The density of states (DOS) plots for $Ce_3Rh_{11}Ge_5$, $CeRh_5Ge_3$, and $CeRh_3Ge_2$ reveal the expected metallic nature of these compounds, with the Fermi level crossing a wide manifold of states extending from –6 to +2 eV (Figure 2-9).[36–39] Rh 5s states are the dominant contribution to this band, but Ce states are found near the top. Ge states are found very deep in energy from –12 to –8 eV (s-states) and above –6 eV (p-states), typical of other related germanides. Interestingly, the short Ge–Ge distance found in $Ce_3Rh_{11}Ge_5$ corresponds to an electronically stable configuration, and arises from the mixing of Ge s- and p-states for atoms in the closely spaced 2*a* and 2*b* sites. (The Ge atoms in the 6*g* site are unaffected.)

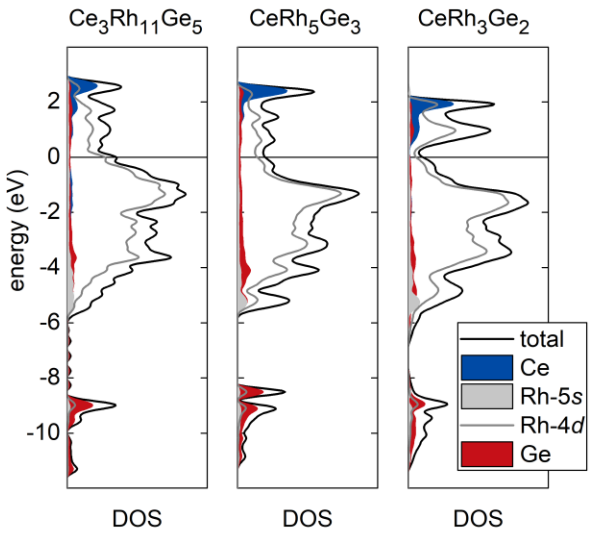

Figure 2-9. Density of states for $Ce_3Rh_{11}Ge_5$, $CeRh_5Ge_3$, and $CeRh_3Ge_2$.

With the addition of these three new phases, Table 2-9 lists all ternary Ce–Rh–Ge compounds identified to date, in order of increasing Rh content. There remain several other phases for which structural characterization is still lacking. Figure 2-10 gives a composition map of ternary phases known so far.

Table 2-9. Ternary Phases in the Ce–Rh–Ge System.

compound	structure type	space group	*a* (Å)	*b* (Å)	*c* (Å)	Reference
Ce_5RhGe_2	Y_2HfS_5	*Pnma*	12.342(2)	8.932(1)	7.985(1)	35
$CeRh_{0.675}Ge_{2.325}$	$CeRh_{0.675}Ge_{2.325}$	*Pmmn*	4.322(2)	4.339(2)	17.101(7)	40
$CeRhGe_2$	$CeNiSi_2$	*Cmcm*	4.3335(13)	17.115(5)	4.3196(11)	4
$Ce_3Rh_2Ge_2$	$La_3Ni_2Ga_2$	*Pbcm*	5.7001(9)	8.099(1)	13.461(3)	41
$Ce_2Rh_3Ge_5$	$U_2Co_3Ge_5$	*Ibam*	10.101(2)	12.104(2)	5.991(1)	1
CeRhGe	TiNiSi	*Pmma*	7.424(2)	4.468(8)	7.120(3)	8, 42
$Ce_3Rh_4Ge_4$	$U_3Ni_4Si_4$	*Immm*	4.0915(5)	4.2400(19)	25.0673(82)	43
$Ce_4Rh_{13}Ge_9$	$Ho_4Ir_{13}Ge_9$	*Pmmn*	3.989(1)	11.250(3)	19.446(5)	44
$CeRh_3Ge_2$	$CeRh_3Ge_2$	*Fmmm*	7.392(6)	11.341(9)	19.661(16)	This work
$CeRhGe_3$	$BaNiSn_3$	*I4mm*	4.3976(3)	-	10.0322(7)	9, 34, 45

$CeRh_2Ge_2$	$CeAl_2Ge_2$	*I*4/*mmm*	4.160(4)	-	10.438(8)	31, 46
$CeRh_{0.5}Ge_{1.5}$	AlB_2	*I*6/*mmm*	4.2615(7)	-	4.1813(9)	47
$CeRh_{1.4}Ge_{0.6}$	$MgZn_2$	$P6_3/mmc$	5.310(3)	-	8.950(5)	7
$CeRh_6Ge_4$	$LiCo_6P_4$	$P\bar{6}m2$	7.154(2)	-	3.855(1)	31
$CeRh_5Ge_3$	$SmRh_5Ge_3$	$P6_3/m$	22.8480(11)	-	3.9208(2)	This work
$Ce_3Rh_{11}Ge_5$	$Sc_3Ni_{11}Ge_4$	$P6_3/mmc$	8.6964(12)	-	9.2209(12)	This work
$Ce_3Rh_4Ge_{13}$	$Y_3Co_4Ge_{13}$	*Pm*-3*n*	9.08(2)	-	-	7
$Ce_{0.70}Rh_{0.10}Ge_{0.20}$	unknown	-	-	-	-	7
$Ce_{0.40}Rh_{0.20}Ge_{0.40}$	unknown	-	-	-	-	7
$Ce_{0.50}Rh_{0.27}Ge_{0.23}$	unknown	-	-	-	-	7
$Ce_{0.225}Rh_{0.45}Ge_{0.325}$	unknown	-	-	-	-	7
$Ce_{0.075}Rh_{0.50}Ge_{0.425}$	unknown	-	-	-	-	7
$CeRh_2Ge$	unknown	-	-	-	-	7
$Ce_{0.18}Rh_{0.52}Ge_{0.30}$	unknown	-	-	-	-	7
$Ce_{0.12}Rh_{0.53}Ge_{0.35}$	unknown	-	-	-	-	7
$Ce_{0.215}Rh_{0.57}Ge_{0.215}$	unknown	-	-	-	-	7
$Ce_{0.115}Rh_{0.685}Ge_{0.20}$	unknown	-	-	-	-	7

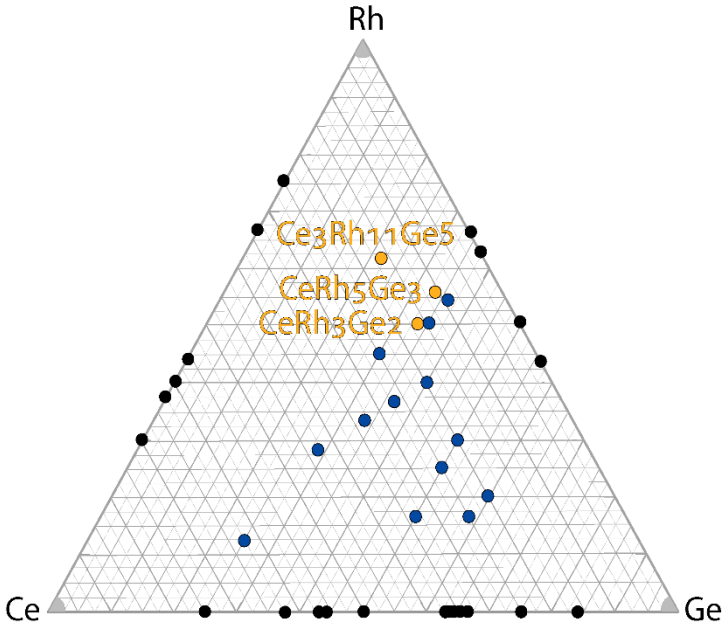

Figure 2-10. Composition map showing previously identified binary (black) and ternary phases (blue), and newly identified ternary phases (yellow).

2.4 Conclusion

Three new Rh-rich ternary phases in the Ce–Rh–Ge system were synthesized at 800 °C and structurally characterized. $Ce_3Rh_{11}Ge_5$ and $CeRh_5Ge_3$ adopt hexagonal structures whereas $CeRh_3Ge_2$ has an orthorhombic structure. All have similar motifs with Ce surrounded by Rh and Ge atoms in hexagonal prisms, distorted to some degree depending on the structure. Although electron density maps reveal residual features, the proposed structures are the best models developed so far for compounds that had remained unsolved for over twenty years. These Rh-rich compounds are interesting because they are expected to show negatively charged Rh atoms, similar to the situation in aurides (such as CsAu).[48–50] Electron localization functions and Bader charge analysis support this proposal, in which the electropositive Ce atoms are embedded within an anionic network of Rh and Ge atoms.

2.5 References

1. Venturini, G.; Méot-Meyer, M.; Marêché, J. F.; Malaman, B.; Roques, B. De nouveaux isotypes de $U_2Co_3Si_5$ ou $Lu_2Co_3Si_5$ dans les systems *R*–*T*–Ge (*R* = elements des terres rares; *T* = Ru, Co, Rh, Ir). Supraconductivite de $Y_2Ir_3Ge_5$. *Mater. Res. Bull.* **1986**, *21*, 33–39.
2. Singh, Y.; Ramakrishnan, S. Magnetic ordering and superconductivity in the $R_2Ir_3Ge_5$ (*R* = Y, La, Ce–Nd, Gd–Tm, Lu) system. *Phys. Rev. B* **2004**, *69*, 174423-1–174423-13.
3. Kong, H.; Shi, X.; Uher, C.; Morelli, D. T. Thermoelectric properties of rare earth–ruthenium–germanium compounds. *J. Appl. Phys.* **2007**, *102*, 023702-1–023702-5.
4. Morozkin, A. V.; Seropegin, Y. D.; Bodak, O. I. Phase equilibria in the Sm–{Ru, Rh}–{Si, Ge} systems at 870 K. *J. Alloys Compd.* **1996**, *234*, 143–150.
5. Seropegin, Y. D.; Gribanov, A. V.; Bodak, O. I. Isothermal cross-section of the Ce–Pd–Ge phase diagram at 600 °C. *J. Alloys Compd.* **1998**, *269*, 157–161.

6. Bodak, O. I.; Pecharskij, V. K.; Sologub, O. L.; Rybakov, V. B. New ternary ruthenium germanides. *Izv. Akad. Nauk SSSR, Met.* **1990**, *5*, 217–219.

7. Shapiev, B. I. *Dissertation*; Moscow State University: Moscow, 1993.

8. Rogl, P.; Chevalier, B.; Besnus, M. J.; Etourneau, J. Magnetic and electrical properties of the equiatomic cerium germanides Ce*M*Ge (*M* = Rh, Ir, Pd, Pt). *J. Magn. Magn. Mater.* **1989**, *80*, 305–310.

9. Muro, Y.; Eom, D.; Takeda, N.; Ishikawa, M. Contrasting Kondo-lattice behavior in Ce*T*Si_3 and Ce*T*Ge_3 (*T* = Rh and Ir). *J. Phys. Soc. Jpn.* **1998**, *67*, 3601–3604.

10. Hirose, Y.; Nishimura, N.; Honda, F.; Sugiyama, K.; Hagiwara, M.; Kindo, K.; Takeuchi, T.; Yamamoto, E.; Haga, Y.; Matsuura, M.; Hirota, K.; Yasui, A.; Yamagami, H.; Settai, R.; Ōnuki, Y. Magnetic and superconducting properties of $CeRhGe_2$ and $CePtSi_2$. *J. Phys. Soc. Jpn.* **2011**, *80*, 024711-1–024711-12.

11. Sheldrick, G. M. *SHELXTL*, version 6.12; Bruker AXS Inc.: Madison, WI, 2001.

12. Bruker AXS (2008): *TOPAS* V4: General profile and structure analysis software for powder diffraction data. - User's Manual, Bruker AXS, Karlsruhe, Germany.

13. Kresse, G.; Furthmüller, J. Efficient iterative schemes for Ab Initio total-energy calculations using a plane-wave basis set. *Phys. Rev. B* **1996**, *54*, 11169−11186.

14. Kresse, G.; Joubert, D. From ultrasoft pseudopotentials to the projector augmented-wave method. *Phys. Rev. B* **1999**, *59*, 1758−1775.

15. Kohout, M.; Wagner, F. R.; Grin, Y. Electron localization function for transition-metal compounds. *Theor. Chem. Acc*. **2002**, *108*, 150−156.

16. Grin, Y.; Savin, A.; Silvi, B. The ELF perspective of chemical bonding. In *The Chemical Bond: Fundamental Aspects of Chemical Bonding*; Frenking, G., Shaik, S., Eds.; Wiley-VCH Verlag GmbH & Co. KGaA: Weinheim, Germany, 2014, 345−382.

17. Kohout, M.; Savin, A. Influence of core-valence separation of electron localization function. *J. Comput. Chem.* **1997**, *18*, 1431−1439.

18. Tang, W.; Sanville, E.; Henkelman, G. A grid-based bader analysis algorithm without lattice bias. *J. Phys.: Condens. Matter*. **2009**, *21*, 84204-1–84204-7.

19. Andrusyak, R. I. *Sov. Phys. Crystallogr*. **1988**, *33*, 599–600.

20. Gladyshevskii, R. E.; Strusievicz, O. R.; Cenzual, K.; Parthé, E. Structure of $Gd_3Ru_4Al_{12}$, a new member of the $EuMg_{5.2}$ structure family with minority-atom clusters. *Acta Crystallogr., Sect. B* **1993**, *49*, 474–478.

21. Morozkin, A. V.; Knotko, A. V.; Yapaskurt, V. O.; Yuan, F.; Mozharivskyj, Y.; Pani, M.; Provino, A.; Manfrinetti, P. The Ho–Ni–Ge system: Isothermal section and new rare-earth nickel germanides. *J. Solid State Chem.* **2015**, *225*, 193–201.

22. Gladyshevskii, E. I. Crystal structure of the digermanide of rare earth elements. *J. Struct. Chem.* **1964**, *5*, 523–529.

23. Yakinthos, J. K. Crystal and magnetic structures of $TmFe_2Si_2$ and $TmNi_2Ge_2$ compounds. Influence of the d-metal charge on the anisotropy direction of the RT_2X_2 (R = rare earth, T = 3d or 4d metal and X = Si, Ge) compounds. *J. Magn. Magn. Mater.* **1991**, *99*, 123–132.

24. Marazza, R.; Ferro, R.; Rambaldi, G.; Zanicchi, G. Some phases in ternary alloys of thorium and uranium with the Al_4Ba-$ThCu_2Si_2$-type structure. *J. Less. Common Met.* **1977**, *53*, 193–197.

25. Mishra, V.; Oliynyk, A. O.; Subbarao, U.; Sarma, S. C.; Mumbaraddi, D.; Roy, S.; Peter, S. C. Complex crystal chemistry of $Yb_6(CuGa)_{50}$ and $Yb_6(CuGa)_{51}$ grown at different synthetic conditions. *Cryst. Growth Des*. **2018**, *18*, 6091–6099.

26. Oliynyk, A. O.; Mar, A. Rare-earth manganese germanides $RE_{2+x}MnGe_{2+y}$ (*RE* = La, Ce) built from four-membered rings and *stellae quadrangulae* of Mn-centred tetrahedra. *J. Solid State Chem*. **2013**, *206*, 60–65.

27. Oliynyk, A. O.; Sparks, T. D.; Gaultois, M. W.; Ghadbeigi, L.; Mar, A. $Gd_{12}Co_{5.3}Bi$ and $Gd_{12}Co_5Bi$, crystalline doppelgänger with low thermal conductivities. *Inorg. Chem.* **2016**, *55*, 6625–6633.

28. Morozkin, A. V.; Bogdanov, A. E.; Welter, R. New RRh_5Ge_3 compounds of the new $SmRh_5Ge_3$ structure type and their magnetic properties (*R* = Sm, Gd, Tb). *J. Alloys Compd*. **2002**, *340*, 49–53.

29. Yarmolyuk, Y. P.; Akselrud, L. G.; Gladyshevskii, E. I. Crystal structures of UCo_5Si_3 and $ZrCo_5Si_3$. *Sov. Phys.Crystallogr.* **1978**, *23*, 942–945.

30. Morozkin, A. V.; Seropegin, Y. D.; Sviridov, I. A.; Bodak, O. I. Crystallographic data for new ternary UCo_5Si_3-type RRh_5Si_3 (*R* = Sm, Gd–Tm) compounds. *J. Alloys Compd*. **1998**, *274*, L1–L5.

31. Vosswinkel, D.; Niehaus, O.; Rodewald, U. C.; Poettgen, R. Bismuth flux growth of $CeRh_6Ge_4$ and $CeRh_2Ge_2$ single crystals. *Z. Nat. Forsch. B* **2012**, *67*, 1241–1247.

32. Sheldrick, G. M. (2008). *CELL_NOW*. Version 2008/4. Georg-August-Universität Göttingen, Göttingen, Germany.

33. Vosswinkel, D.; Poettgen, R. Synthesis of $Ce_2Rh_3Ge_5$ crystals from a bismuth flux. *Z. Nat. Forsch. B* **2013**, *68*, 301–305.

34. Kawai, T.; Muranaka, H.; Measson, M. A.; Shimoda, T.; Doi, Y.; Matsuda, T. D.; Haga, Y.; Knebel, G.; Lapertot, G.; Aoki, D.; Flouquet, J.; Takeuchi, T.; Settai, R.; Ōnuki, Y. Magnetic and superconducting properties of CeTX_3 (T: transition metal and X: Si and Ge) with non-centrosymmetric crystal structure. *J. Phys. Soc. Jpn*. **2008**, *77*, 064716-1–064716-9.

35. Sologub, O. L.; Salamakha, P. S.; Godart, C. Formation, crystal structure and magnetism of ternary compounds Ce_5MGe_2 (M = Co, Ni, Ru, Rh, Pd, Ir, Pt). *J. Alloys Compd.* **2000**, *307*, 31–39.

36. Zhang, D.; Oliynyk, A. O.; Duarte, G. M.; Iyer, A. K.; Ghadbeigi, L.; Kauwe, S. K.; Sparks, T. D.; Mar, A. Not just par for the course: 73 quaternary germanides $RE_4M_2XGe_4$ (RE = La–Nd, Sm, Gd–Tm, Lu; M = Mn–Ni; X = Ag, Cd) and the search for intermetallics with low thermal conductivity. *Inorg. Chem.* **2018**, *57*, 14249–14259.

37. Oliynyk, A. O.; Stoyko, S. S.; Mar, A. Many metals make the cut: quaternary rare-earth germanides $RE_4M_2InGe_4$ (M = Fe, Co, Ni, Ru, Rh, Ir) and $RE_4RhInGe_4$ derived from excision of slabs in RE_2InGe_2. *Inorg. Chem*. **2015**, *54*, 2780–2792.

38. Oliynyk, A. O.; Stoyko, S. S.; Mar, A. Quaternary germanides $RE_4Mn_2InGe_4$ (RE = La–Nd, Sm, Gd–Tm, Lu). *Inorg. Chem*. **2013**, *52*, 8264–8271.

39. Oliynyk, A. O.; Stoyko, S. S.; Mar, A. Ternary rare-earth ruthenium and iridium germanides $RE_3M_2Ge_3$ (RE = Y, Gd–Tm, Lu; M = Ru, Ir). *J. Solid State Chem*. **2013**, *202*, 241–249.

40. Shapiev, B. I.; Sologub, O. L.; Seropegin, J. D.; Bodak, O. I.; Salamakha, P. S. Crystal structure of the compound $CeRh_{1-x}Ge_{2+x}$ (x = 0.325). *J. Less. Common Met.* **1991**, *175*, L1–L4.

41. Gladyshevskii, R. E.; Zhao, J. T.; Parthé, E. $Ce_3Rh_2Ge_2$ and isotypes with the orthorhombic $La_3Ni_2Ga_2$ type. *Acta Crystallogr., Sect. C* **1992**, *48*, 10–13.

42. Hovestreydt, E.; Engel, N.; Klepp, K.; Chabot, B.; Parthé, E. Equiatomic ternary rare earth-transition metal silicides, germanides and gallides. *J. Less. Common Met.* **1982**, *85*, 247–274.

43. Rogl, P.; Chevalier, B.; Etourneau, J. Structural chemistry and magnetic properties of ternary germanides $Ce_3Rh_4Ge_4$ and $Ce_3Rh_3IrGe_4$. *J. Solid State Chem.* **1990**, *88*, 429–434.

44. Salamakha, P. S.; Sologub, O. L. New ternary rare earth–rhodium–germanides: $Ce_4Rh_{13}Ge_9$ and Ho_2RhGe_2. *J. Alloys Compd.* **1999**, *287*, L1–L3.

45. Venturini, G.; Méot-Meyer, M.; Malaman, B.; Roques, B. De nouvelles séries de germaniures, isotypes de $Yb_3Rh_4Sn_{13}$ et $BaNiSn_3$, dans les systèmes ternaires *TR*–*T*–Ge où *TR* est un élément des terres rares et *T* ≡ Co, Rh, Ir, Ru, Os. *J. Less. Common Met.* **1985**, *113*, 197–204.

46. Francois, M.; Venturini, G.; Marêché, J. F.; Malaman, B.; Roques, B. De nouvelles séries de germaniures, isotypes de $U_4Re_7Si_6$, $ThCr_2Si_2$ et $CaBe_2Ge_2$, dans les systèmes ternaires *R*–*T*–Ge où *R* est un élément des terres rares et *T* ≡ Ru, Os, Rh, Ir: supraconductivité de $LaIr_2Ge_2$. *J. Less. Common Met*. **1985**, *113*, 231–237.

47. Kalsi, D.; Subbarao, U.; Rayaprol, S.; Peter, S. C. Structural and magnetic properties in the polymorphs of $CeRh_{0.5}Ge_{1.5}$. *J. Solid State Chem.* **2014**, *212*, 73–80.

48. Oliynyk, A. O.; Adutwum, L. A.; Harynuk J. J.; Mar, A. Classifying crystal structures of binary compounds *AB* through cluster resolution feature selection and support vector machine analysis. *Chem. Mater*. **2016**, *28*, 6672–6681.

49. Lotfi, S.; Oliynyk, A. O.; Brgoch, J. Polyanionic gold–tin bonding and crystal structure preference in $REAu_{1.5}Sn_{0.5}$ (*RE* = La, Ce, Pr, Nd). *Inorg. Chem.* **2018**, *57*, 10736–10743.

50. Smetana, V.; Corbett, J. D.; Miller, G. J. Four polyanionic compounds in the K−Au−Ga system: A case study in exploratory synthesis and of the art of structural analysis. *Inorg. Chem.* **2012**, *51*, 1695–1702.

Chapter 3 Not Just Par for the Course: 73 Quaternary Germanides RE_4M_2XGe$_4$ (RE = La–Nd, Sm, Gd–Tm, Lu; M = Mn–Ni; X = Ag, Cd) and the Search for Intermetallics with Low Thermal Conductivity

A version of this chapter has been published. Zhang, D.; Oliynyk, A. O.; Duarte, G. M.; Iyer, A. K.; Ghadbeigi, L.; Kauwe, S. K.; Sparks, T. D.; Mar, A. Inorg. Chem. 2018, 57, 14249—14259.

3.1 Introduction

Intermetallic germanides exhibit a rich structural chemistry having many similarities to silicides, but with a more pronounced tendency for dense and complex atomic arrangements that reflect the greater metallic character of the bonding. They are especially plentiful in combination with rare-earth metals.[1] Many ternary rare-earth germanides *RE*–*M*–Ge (where *M* is a d-block metal or p-block metalloid) show interesting physical properties such as superconductivity (e.g., YM_2Ge$_2$, RE_2Ir$_3$Ge$_5$)[2–4] and magnetocaloric effects (e.g., Gd$_5$Si$_2$Ge$_2$).[5] The number of quaternary rare-earth germanides *RE*–*M*–*M*′–Ge is potentially very large, with several thousand possible combinations of elements, but only a few hundred compounds have been identified so far.[6] Many previously known quaternary germanides, such as REAuAl$_4$Ge$_2$,[7] RE_3CoAl$_3$Ge$_2$,[8] REMGa$_3$Ge (M = Co, Ni),[9] RE_2MGa$_9$Ge$_2$ (M = Co, Ni),[10] Yb$_7$Ni$_4$InGe$_{12}$,[11] and Yb$_3$AuIn$_3$Ge$_2$,[12] were inadvertently obtained in the presence of Al, Ga, or In reactive fluxes. Site disorder of metal components is frequently observed in the structures of these quaternary germanides. However, an ordered arrangement of all four elements is found in the versatile Ho$_4$Ni$_2$InGe$_4$-type structure.[13] Through

systematic investigations, we have recently expanded the number of representatives in this structure type so that it is currently the most prevalent among quaternary rare-earth germanides known to date. About 60 compounds $RE_4M_2InGe_4$ (M = Mn, Fe, Co, Ni, Ru, Rh, Ir) were synthesized,[14,15] and they were established to be thermodynamically stable phases that do not require a flux to be prepared.[16] Moreover, the analysis of this quaternary structure type in terms of cutting strips out of a parent ternary germanide RE_2InGe_2 led to the derivation of a different quaternary germanide $RE_4RhInGe_4$.[15,17]

In general, the metallic behaviour of intermetallic compounds renders them unfavourable for applications such as good thermoelectric materials unless they fall into a special category in which a hybridization gap forms.[18–21] Identifying new intermetallic compounds which exhibit inherent structural features that give rise to low thermal conductivity is thus important in gaining insight for designing thermoelectric materials. We have been interested in applying machine-learning approaches to discover intermetallic compounds with specific structures and properties.[22,23] These methods show promise in aiding the accelerated search for new materials and guiding synthetic efforts by suggesting candidates different from existing ones. These models are built by applying various algorithms (e.g., support vector machine, random forest) to relate experimental crystal data and physical property measurements to chemical descriptors, enabling predictions of new materials to be made. In particular, machine-learning models have been developed to recommend new candidates for thermoelectric materials and to predict relevant properties such as thermal conductivity and heat capacity.[24–27] Although machine learning has become exceedingly popular for predicting new materials, experimental validation of these models remains sparse.[28–33]

In this study, we address further questions engendered by the previous work on $RE_4M_2InGe_4$ and by the desire to apply machine-learning methods to identify novel candidates for thermoelectric materials. First, given that the substitutional ranges for *RE* and *M* components are quite broad, would the same versatility be extended to substitution for the In and Ge components to expand the scope of these quaternary germanides to $RE_4M_2XTt_4$? Thus, we explore the possibility that In can be substituted by neighbouring d-block elements (*X* = Ag, Cd), and Ge by a lighter tetrel (*Tt* = Si). These changes are more drastic and are expected to be more difficult than the previous substitutions of *RE* and *M* components. In particular, it is not obvious if the unusual feature of square planar coordination of Ge atoms around the In centres observed in $RE_4M_2InGe_4$ can be retained by substitutions of these components. Second, and perhaps more bold, does the encapsulation of the square planar centre within a large cage in the structure lead to atomic rattling, thereby enhancing the possibility of obtaining low thermal conductivity within an intermetallic compound? These germanides serve as a fascinating test case to validate the machine-learning models for predicting thermal conductivities and heat capacities of inorganic solids.

3.2 Experimental Section

3.2.1 Synthesis

Starting materials were freshly filed pieces of normally trivalent rare-earth metals (*RE* = La–Nd, Sm, Gd–Tm, Lu; 99.9%, Hefa), powders of transition metals (*M* = Mn, Fe, Co, Ni; >99%, Cerac or Alfa; and *X* = Ag, Cd; 99.95%, Alfa or Mackay), and elemental Ge (powder, 99.999%, Aldrich; or ingot, 99.9999%, Alfa). Mixtures of the components in the stoichiometric ratio of *RE*:*M*:*X*:Ge = 4:2:1:4 with a total mass of 0.20 g were pressed into pellets. The Ag-containing samples were arc-melted twice in a Centorr 5TA tri-arc furnace on a water-cooled copper hearth under an argon atmosphere. The mass loss of all arc-melted samples was less than 5%, and for

most samples, it was less than 1%. Arc-melting of the Cd-containing samples was not attempted because the high vapour pressure of Cd would be anticipated to cause difficulties in maintaining the correct stoichiometry. The arc-melted ingots of the Ag-containing samples and the cold-pressed pellets of the Cd-containing samples were then placed in fused-silica tubes, which were evacuated and sealed. The tubes were heated at 800 °C for 10 d, after which they were quenched in cold water for the Ag-containing samples or allowed to cool to room temperature for the Cd-containing samples.

Formation of the solid solution $Nd_4Mn_2Cd(Ge_{1-y}Si_y)_4$ was investigated. In addition to the end-member $Nd_4Mn_2CdGe_4$ already obtained as described above, additional Si-containing samples were prepared with nominal compositions $Nd_4Mn_2CdGe_2Si_2$, $Nd_4Mn_2CdGe_{1.5}Si_{2.5}$, and $Nd_4Mn_2CdSi_4$. Si powder (>99%, Alfa) was combined with the other elements, the mixtures were cold-pressed into pellets and placed into evacuated fused-silica tubes, and the same heat treatment at 800 °C was used as before.

Powder X-ray diffraction (XRD) patterns of the ground samples were collected on an Inel diffractometer equipped with a curved position-sensitive detector (CPS 120) and a Cu $K\alpha_1$ radiation source operated at 40 kV and 20 mA. The patterns were analyzed with the CSD suite of programs.[34] Table A1-1 in Supporting Information lists the phases and their relative amounts (estimated from peak heights) obtained in the samples. Table 3-1 summarizes the results and identifies which reactions were successful in forming the quaternary germanides, and Table 3-2 lists their cell parameters refined from the powder XRD data. Energy-dispersive X-ray (EDX) analysis was carried out on a JEOL JSM-6010LA InTouchScope scanning electron microscope operated with an accelerating voltage of 20 kV and acquisition times of 70 s, to determine the compositions of selected crystals or establish the phase equilibria of polished samples.

Table 3-1. Formation of Quaternary Germanides $RE_4M_2AgGe_4$ and $RE_4M_2CdGe_4$ [a].

compound	La	Ce	Pr	Nd	Sm	Gd	Tb	Dy	Ho	Er	Tm	Lu
$RE_4Mn_2AgGe_4$	+	+	+	+	+	+	+	+	+	–	–	–
$RE_4Fe_2AgGe_4$	–	+	+	+	+	+	+	+	+	+	+	+
$RE_4Co_2AgGe_4$	–	–	+	+	+	+	+	+	+	+	+	–
$RE_4Ni_2AgGe_4$	–	–	+	+	+	+	+	+	+	–	–	–
$RE_4Mn_2CdGe_4$	+	+	+	+	+	+	+	+	+	+	+	+
$RE_4Fe_2CdGe_4$	–	–	–	+	+	+	+	+	+	+	+	+
$RE_4Co_2CdGe_4$	–	+	+	+	+	+	+	+	+	+	+	–
$RE_4Ni_2CdGe_4$	–	–	–	–	+	+	+	+	+	+	–	–

[a] Legend: formed (+), unknown (–).

Table 3-2. Cell Parameters for RE_4M_2XGe$_4$ Refined from Powder XRD Data.

compound	*a* (Å)	*b* (Å)	*c* (Å)	β (°)	*V* (Å^3)
***RE*$_4$Mn$_2$AgGe$_4$**					
La$_4$Mn$_2$AgGe$_4$	16.561(6)	4.560(2)	7.489(2)	106.204(7)	543.1(6)
Ce$_4$Mn$_2$AgGe$_4$	16.366(6)	4.356(2)	7.347(1)	106.63(2)	501.9(6)
Pr$_4$Mn$_2$AgGe$_4$	16.378(2)	4.347(1)	7.339(2)	106.73(1)	500.4(4)
Nd$_4$Mn$_2$AgGe$_4$	16.307(3)	4.326(3)	7.301(2)	106.62(3)	493.5(6)
Sm$_4$Mn$_2$AgGe$_4$	16.138(2)	4.278(1)	7.2221(6)	106.46(1)	478.2(3)
Gd$_4$Mn$_2$AgGe$_4$	15.983(2)	4.236(2)	7.110(1)	106.31(1)	462.0(4)
Tb$_4$Mn$_2$AgGe$_4$	15.937(2)	4.230(2)	7.1158(10)	106.05(1)	461.0(4)
Dy$_4$Mn$_2$AgGe$_4$	15.806(9)	4.187(6)	7.070(7)	106.17(8)	449.4(9)
Ho$_4$Mn$_2$AgGe$_4$	15.590(4)	4.169(1)	7.231(1)	108.58(2)	445.8(4)
***RE*$_4$Fe$_2$AgGe$_4$**					
Ce$_4$Fe$_2$AgGe$_4$	16.089(4)	4.191(1)	7.249(1)	106.81(2)	467.9(4)
Pr$_4$Fe$_2$AgGe$_4$	15.976(5)	4.170(2)	7.2141(8)	106.77(3)	460.2(5)
Nd$_4$Fe$_2$AgGe$_4$	15.595(3)	4.1894(8)	7.085(1)	106.17(2)	444.6(3)
Sm$_4$Fe$_2$AgGe$_4$	15.595(4)	4.124(2)	7.129(3)	106.55(8)	439.5(7)
Gd$_4$Fe$_2$AgGe$_4$	15.657(3)	4.224(2)	6.863(2)	106.48(3)	435.3(4)
Tb$_4$Fe$_2$AgGe$_4$	15.356(8)	4.203(2)	7.025(4)	106.12(2)	435.6(7)
Dy$_4$Fe$_2$AgGe$_4$	15.411(8)	4.171(3)	7.039(3)	106.30(8)	433.9(9)
Ho$_4$Fe$_2$AgGe$_4$	15.377(3)	4.178(1)	7.024(1)	106.28(3)	433.2(3)
Er$_4$Fe$_2$AgGe$_4$	15.230(4)	4.232(2)	6.948(2)	107.41(3)	427.3(5)
Tm$_4$Fe$_2$AgGe$_4$	15.181(4)	4.219(2)	6.909(2)	107.90(5)	421.1(6)
Lu$_4$Fe$_2$AgGe$_4$	15.106(6)	4.183(3)	6.849(4)	108.34(5)	410.8(8)
***RE*$_4$Co$_2$AgGe$_4$**					
Pr$_4$Co$_2$AgGe$_4$	16.124(5)	4.151(2)	7.346(2)	106.23(3)	472.1(5)
Nd$_4$Co$_2$AgGe$_4$	15.878(9)	4.252(3)	7.155(3)	106.45(2)	463.2(8)
Sm$_4$Co$_2$AgGe$_4$	14.841(5)	4.256(3)	7.17(1)	106.14(5)	435.0(9)
Gd$_4$Co$_2$AgGe$_4$	14.79(2)	4.306(6)	7.137(3)	108.50(2)	431.1(9)
Tb$_4$Co$_2$AgGe$_4$	14.578(3)	4.311(1)	7.193(3)	108.148(9)	429.5(4)
Dy$_4$Co$_2$AgGe$_4$	14.706(5)	4.179(2)	7.225(5)	108.39(2)	421.3(7)
Ho$_4$Co$_2$AgGe$_4$	14.601(4)	4.176(1)	7.1087(9)	108.13(2)	411.9(3)

$Er_4Co_2AgGe_4$	14.410(7)	4.160(1)	6.972(3)	108.80(3)	395.6(5)
$Tm_4Co_2AgGe_4$	14.228(4)	4.150(8)	6.817(2)	107.21(3)	384.5(9)
***RE*$_4$Ni$_2$AgGe$_4$**					
$Pr_4Ni_2AgGe_4$	16.271(5)	4.330(4)	7.181(5)	108.30(4)	480.3(9)
$Nd_4Ni_2AgGe_4$	16.01(1)	4.070(5)	7.346(4)	108.11(5)	454.9(9)
$Sm_4Ni_2AgGe_4$	15.605(3)	4.123(2)	7.215(4)	108.01(4)	441.5(7)
$Gd_4Ni_2AgGe_4$	15.243(8)	4.103(3)	7.238(3)	107.97(4)	430.6(8)
$Tb_4Ni_2AgGe_4$	15.138(4)	4.089(2)	7.252(2)	107.78(3)	427.5(5)
$Dy_4Ni_2AgGe_4$	14.874(4)	4.021(2)	6.947(9)	107.11(4)	397.1(9)
$Ho_4Ni_2AgGe_4$	14.819(4)	4.015(2)	6.916(2)	108.25(3)	390.8(5)
***RE*$_4$Mn$_2$CdGe$_4$**					
$La_4Mn_2CdGe_4$	16.732(4)	4.403(2)	7.539(2)	107.16(2)	530.7(6)
$Ce_4Mn_2CdGe_4$	16.508(4)	4.353(1)	7.448(1)	107.13(2)	511.5(4)
$Pr_4Mn_2Cd_2Ge_4$	16.467(2)	4.340(2)	7.412(2)	106.78(2)	507.2(5)
$Nd_4Mn_2CdGe_4$	16.372(4)	4.314(3)	7.382(3)	107.04(6)	498.5(8)
$Sm_4Mn_2CdGe_4$	16.142(5)	4.243(2)	7.251(2)	106.61(1)	475.9(6)
$Gd_4Mn_2CdGe_4$	16.110(7)	4.246(5)	7.237(2)	106.36(4)	475.0(9)
$Tb_4Mn_2CdGe_4$	16.034(8)	4.267(3)	7.186(4)	106.08(2)	472.4(9)
$Dy_4Mn_2CdGe_4$	15.775(7)	4.156(2)	7.079(2)	106.22(2)	445.6(6)
$Ho_4Mn_2CdGe_4$	15.817(4)	4.141(1)	7.089(2)	106.106(6)	446.1(4)
$Er_4Mn_2CdGe_4$	15.746(5)	4.120(2)	7.048(2)	106.081(8)	439.3(5)
$Tm_4Mn_2CdGe_4$	15.670(4)	4.112(2)	7.022(2)	106.06(2)	434.8(5)
$Lu_4Mn_2CdGe_4$	15.586(3)	4.074(1)	6.975(2)	105.799(6)	426.2(3)
***RE*$_4$Fe$_2$CdGe$_4$**					
$Nd_4Fe_2CdGe_4$	16.168(2)	4.333(1)	7.292(2)	107.31(1)	487.7(4)
$Sm_4Fe_2CdGe_4$	15.793(9)	4.242(3)	7.153(4)	107.34(3)	457.4(9)
$Gd_4Fe_2CdGe_4$	15.691(6)	4.207(2)	7.081(3)	107.102(7)	446.8(6)
$Tb_4Fe_2CdGe_4$	15.645(6)	4.202(3)	7.061(4)	107.18(4)	443.5(9)
$Dy_4Fe_2CdGe_4$	15.60(2)	4.179(5)	7.047(7)	107.15(2)	439.0(9)
$Ho_4Fe_2CdGe_4$	15.50(2)	4.148(6)	6.96(1)	107.25(2)	427.4(9)
$Er_4Fe_2CdGe_4$	15.478(6)	4.143(2)	6.966(3)	107.058(8)	427.0(6)
$Tm_4Fe_2CdGe_4$	15.392(9)	4.123(2)	6.924(4)	107.052(5)	420.1(7)

$Lu_4Fe_2CdGe_4$	15.290(5)	4.092(3)	6.882(3)	106.86(1)	412.1(7)
***RE*$_4$Co$_2$CdGe$_4$**					
$Ce_4Co_2CdGe_4$	15.993(8)	4.306(3)	7.274(4)	107.33(1)	478.1(9)
$Pr_4Co_2CdGe_4$	15.862(2)	4.292(1)	7.231(1)	107.51(1)	469.5(3)
$Nd_4Co_2CdGe_4$	15.778(2)	4.272(1)	7.2031(6)	107.42(4)	463.2(3)
$Sm_4Co_2CdGe_4$	15.671(2)	4.237(2)	7.108(3)	107.41(2)	450.3(5)
$Gd_4Co_2CdGe_4$	15.587(5)	4.203(3)	7.053(2)	107.32(2)	441.1(8)
$Tb_4Co_2CdGe_4$	15.586(9)	4.202(3)	7.053(5)	107.38(3)	440.8(9)
$Dy_4Co_2CdGe_4$	15.436(3)	4.177(2)	6.987(1)	107.42(2)	429.8(4)
$Ho_4Co_2CdGe_4$	15.375(2)	4.158(2)	6.956(1)	107.42(2)	424.3(4)
$Er_4Co_2CdGe_4$	15.304(2)	4.1418(9)	6.9278(8)	107.43(2)	419.0(3)
$Tm_4Co_2CdGe_4$	15.229(2)	4.123(2)	6.8896(9)	107.38(2)	412.8(4)
***RE*$_4$Ni$_2$CdGe$_4$**					
$Sm_4Ni_2CdGe_4$	15.708(3)	4.227(1)	7.111(1)	108.39(1)	448.0(3)
$Gd_4Ni_2CdGe_4$	15.593(3)	4.2154(7)	7.081(2)	108.21(2)	442.1(4)
$Tb_4Ni_2CdGe_4$	15.521(2)	4.1915(8)	7.028(1)	108.29(1)	434.1(2)
$Dy_4Ni_2CdGe_4$	15.366(10)	4.164(4)	6.966(5)	108.10(4)	423.7(9)
$Ho_4Ni_2CdGe_4$	15.373(6)	4.162(1)	6.966(2)	108.23(2)	423.3(5)
$Er_4Ni_2CdGe_4$	15.281(4)	4.155(2)	6.945(2)	108.18(2)	418.9(5)

3.2.2 Structure Determination

Suitable single crystals of the quaternary germanides were difficult to extract from the samples prepared above because they tended to be small (typically less than 10 μm in their longest dimension) and irregularly shaped. Considerable effort was expended to select crystals from the Nd-containing samples because these compounds were eventually used for property measurements and for investigating the solid solubility with Si. Representative single crystals were selected from the $Nd_2Mn_2AgGe_4$ ingots and $Nd_2Mn_2Cd(Ge_{1-y}Si_y)_4$ bulk samples. Intensity data were collected at room temperature on a Bruker PLATFORM diffractometer equipped with a SMART APEX II CCD detector and a graphite-monochromated Mo $K\alpha$ radiation source, using ω scans at 6–8 different ϕ angles with a frame width of 0.3º and an exposure time of 12 s per frame. Face-indexed numerical absorption corrections were applied. Structure solution and refinement were carried out with use of the SHELXTL (version 6.12) program package.[35] The monoclinic centrosymmetric space group *C*2/*m* was chosen on the basis of Laue symmetry and intensity statistics, and direct methods confirmed models in agreement with the expected $Ho_4Ni_2InGe_4$-type structure.[13] Atomic positions and labels were standardized with the program STRUCTURE TIDY.[36]

The main challenges in the structure determinations related to the treatment of partial occupancy and site disorder. Because substoichiometry on the square planar In site has been observed in many previously known $RE_4M_2InGe_4$ compounds,[14,15] this possibility was also considered for the analogous Ag and Cd sites in $Nd_2Mn_2AgGe_4$ and $Nd_2Mn_2Cd(Ge_{1-y}Si_y)_4$. Zn was considered at the beginning, but no successful compound was synthesized. When the occupancies of these sites were refined, they converged to values of 0.83(1) Ag in $Nd_4Mn_2AgGe_4$ and 0.86(1)–0.97(3) Cd in $Nd_2Mn_2Cd(Ge_{1-x}Si_x)_4$. We assume that the square planar site is occupied strictly by Ag or Cd atoms, and undergoes no mixing with Mn atoms, because the

distances to the surrounding Ge atoms (3.0 Å or longer) would be far too long for Mn–Ge bonds. The remaining sites in these structures are generally well behaved and were found to be fully occupied. However, in the case of $Nd_4Mn_2AgGe_4$, the displacement parameters for the tetrahedral Mn site were anomalous low (U_{eq} = 0.0034(4) Å^2) compared to those for the other sites (U_{eq} = 0.0116(2)–0.0197(7) Å^2). A possible explanation is that this site contains a disordered mixture of Mn and Ag atoms. When such a model was refined, the occupancies converged to 0.78(1) Mn and 0.22(1) Ag, the displacement parameters became more reasonable (U_{eq} = 0.0116(4) Å^2), and the agreement factors improved slightly (conventional $R(F)$ decreasing from 0.043 to 0.038).

For different members of the $Nd_4Mn_2Cd(Ge_{1-y}Si_y)_4$ solid solution, the two available tetrel (group-14 element, *Tt* = Si, Ge) sites were allowed to be fully occupied with a mixture of Si and Ge atoms, with no constraints placed on the overall composition. The refined compositions agreed well with the nominal compositions. In two of the structure determinations, the checkCIF reports gave alerts detected by the TwinRotMat algorithm in PLATON that twinning may be present.[37] When the suggested twin laws were applied, the BASF values converged to 0.016(2) or 0.047(3) in $Nd_4Mn_2CdGe_4$ and $Nd_4Mn_2CdGe_{1.5}Si_{2.5}$, respectively, with the conventional $R(F)$ values showing a small improvement.

Tables A1-2–A1-4 in Supporting Information lists full crystallographic data. Table 3-3 lists abbreviated crystallographic data and Table 3-4 lists ranges of interatomic distances.

Table 3-3. Crystallographic Data for $Nd_4Mn_2AgGe_4$ and $Nd_4Mn_2Cd(Ge_{1-y}Si_y)_4$ [a].

	$Nd_4Mn_{1.55(2)}Ag_{1.25(2)}Ge_4$	$Nd_4Mn_2Cd_{0.86(1)}Ge_4$	$Nd_4Mn_2Cd_{0.92(1)}Ge_{2.22(1)}Si_{1.78(1)}$	$Nd_4Mn_2Cd_{0.98(1)}Ge_{1.46(3)}Si_{2.54(3)}$	$Nd_4Mn_2Cd_{0.97(1)}Si_4$
fw (amu)	1087.31	1073.86	1001.40	976.12	908.79
a (Å)	16.281(5)	16.016(2)	16.224(12)	16.182(2)	16.0991(10)
b (Å)	4.3473(12)	4.2263(5)	4.305(3)	4.2870(5)	4.2746(3)
c (Å)	7.319(2)	7.1880(9)	7.305(5)	7.2859(9)	7.2517(5)
β (°)	106.855(4)	106.4057(18)	107.023(10)	107.1243(17)	107.2161(10)
V (Å^3)	495.8(2)	466.74(10)	487.9(6)	483.02(10)	476.68(6)
ρ_c (g cm^{-3})	7.284	7.641	6.816	6.712	6.332
μ (mm^{-1})	36.69	38.92	32.20	30.44	26.49
$R(F)$ [b]	0.038	0.036	0.021	0.042	0.020
$R_w(F_o^2)$ [c]	0.091	0.099	0.041	0.127	0.035

[a] For all structures, space group $C2/m$ (No. 12), $Z = 2$, $T = 296(2)$ K, $\lambda = 0.71073$ Å. [b] $R(F) = \sum||F_o| - |F_c|| / \sum|F_o|$ for $F_o^2 > 2\sigma(F_o^2)$. [c] $R_w(F_o^2) = [\sum[w(F_o^2 - F_c^2)^2] / \sum wF_o^4]^{1/2}$; $w^{-1} = [\sigma^2(F_o^2) + (Ap)^2 + Bp]$, where $p = [\max(F_o^2,0) + 2F_c^2] / 3$.

Table 3-4. Ranges of Interatomic Distances (Å) for $Nd_4Mn_2AgGe_4$ and $Nd_4Mn_2Cd(Ge_{(1-y)}Si_y)_4$.

compound	$Nd_4Mn_{1.55(2)}Ag_{1.25(2)}Ge_4$	$Nd_4Mn_2Cd_{0.86(1)}Ge_4$	$Nd_4Mn_2Cd_{0.92(1)}Ge_{2.22(1)}Si_{1.78(1)}$	$Nd_4Mn_2Cd_{0.98(1)}Ge_{1.46(3)}Si_{2.54(3)}$	$Nd_4Mn_2Cd_{0.97(1)}Si_4$
*RE*1–*Tt*	3.018(1)–3.116(2)	2.961(1)–3.042(1)	3.022(2)–3.123(2)	3.021(2)–3.121(2)	3.022(1)–3.129(1)
*RE*1–*M*	3.371(2)–3.506(1)	3.333(2)–3.432(2)	3.349(2)–3.485(2)	3.339(2)–3.472(2)	3.318(1)–3.460(1)
*RE*1–*X*	3.427(1)	3.399(1)	3.437(2)	3.426(1)	3.412(1)
*RE*2–*Tt*	3.122(1)–3.152(1)	3.020(1)–3.094(1)	3.066(2)–3.145(2)	3.045(2)–3.139(2)	3.022(1)–3.132(1)
*RE*2–*M*	3.247(2)–3.276(1)	3.178(2)–3.221(2)	3.224(3)–3.234(2)	3.213(2)–3.218(2)	3.192(1)–3.195(1)
*RE*2–*X*	3.410(1)	3.348(1)	3.409(2)	3.398(1)	3.386(1)
M–*Tt*	2.621(1)–2.692(2)	2.573(1)–2.607(2)	2.575(2)–2.625(2)	2.556(2)–2.606(3)	2.528(1)–2.568(2)
X–*Tt*	2.958(1)–3.166(2)	2.930(1)–3.099(2)	2.990(2)–3.196(2)	2.999(3)–3.206(2)	3.002(2)–3.223(2)
Tt–*Tt*	2.548(3)	2.553(3)	2.515(2)	2.479(5)	2.433(3)

3.2.3 Band Structure Calculations

Tight-binding linear muffin tin orbital band structure calculations were performed for fully stoichiometric and ordered models for $La_4Mn_2AgGe_4$ and $La_4Mn_2CdGe_4$ within the local density and atomic spheres approximation with use of the Stuttgart TB-LMTO-ASA program (version 4.7).[38] The basis sets consisted of La 6s/6p/5d/4f, Mn 4s/4p/3d, Ag or Cd 5s/5p/4d/4f, and Ge 4s/4p/4d orbitals, with the La 6p/4f, Ag or Cd 4f, and Ge 4d orbitals being downfolded. Integrations in reciprocal space were carried out with an improved tetrahedron method over 132 irreducible *k* points within the first Brillouin zone. Bonding characteristics were evaluated through an energy-resolved visualization as quantified by crystal orbital Hamilton populations (COHP).[39]

3.2.4 Machine-Learning Predictions

Within a thermoelectrics recommendation engine developed previously and available online,[25] any arbitrary chemical formula can be entered and the probability that such a composition will exhibit a thermal conductivity lower than 10 W m^{-1} K^{-1} can be computed. Various members of $RE_4M_2XGe_4$ were evaluated in this manner, revealing probabilities greater than 95% for all of them. Similarly, a machine-learning model for predicting heat capacities solely from a chemical formula was previously developed by Sparks et al. based on a training set of thermochemical data obtained from NIST:JANAF tables.[27] The heat capacity of $Nd_4Mn_2InGe_4$ and $Nd_4Mn_2AgGe_4$ was predicted using this model at various temperatures.

3.2.5 Thermal Conductivity

Samples of the previously known compound $Nd_4Mn_2InGe_4$ [14] and the new compound $Nd_4Mn_2AgGe_4$ were available in the form of annealed arc-melted ingots. These Nd-containing samples were chosen for measurement based on the earlier success in preparing $Nd_4Mn_2InGe_4$ in high purity and large quantities. The thermal conductivities κ of these samples were determined

from the standard relationship $\kappa = \rho\alpha C_{p,}$ where ρ is the density, α is the thermal diffusivity, and C_p is the heat capacity at constant pressure. The ingots do not show any large pores and based on similar types of samples measured previously, their density was estimated to be no less than 95% of that calculated from the single-crystal diffraction data. The thermal diffusivity was measured using the laser flash method with a Netzsch LFA 457 instrument with a Cape-Lehman pulse length and heat loss correction model.[40] The samples were polished to become coplanar with a thickness of 3 mm, cut into disc shapes with 8–12 mm diameter via electrical discharge machining, and then coated with graphite on both sides to promote uniform absorption and emission. Measurements were taken from room temperature to 600 °C in increments of 100 °C. Heat capacity values were obtained from high accuracy predictions [27] and verified on a Perkin Elmer Pyris 1 DSC instrument. The samples were small fragments cut from the ingots. Calorimetry measurements were taken from 200 to 600 °C.

3.3 Results and Discussion

3.3.1 Phase Analysis

Given the existence of the quaternary In-containing germanides $RE_4M_2InGe_4$,[13–15] synthetic investigations were focused on replacing In with either Ag or Cd. The targeted compounds belong to 8 series $RE_4M_2XGe_4$ (M = Mn, Fe, Co, Ni; X = Ag, Cd), with the RE components being limited to 12 normally trivalent members (RE = La–Nd, Sm, Gd–Tm, Lu). In total, 96 samples were prepared through reactions of the elements at 800 °C for 10 d, with a preliminary arc-melting step applied to the Ag-containing samples. Out of these samples, 73 contained the desired quaternary phase (Table 1). Multiphase samples were the norm, with the quaternary compound typically being accompanied by two or three other phases (Table A1-1 in Supporting Information). Some samples contained small amounts of oxide impurities, possibly as a result of brief exposure to air

during the transfer of the arc-melted ingots to fused-silica tubes. Oxide phases within some of the Ni-containing samples in $RE_4Ni_2CdGe_4$ series were eventually traced to impurities within the Ni metal source used. In a few favourable cases, nearly phase-pure samples were obtained, as indicated by powder XRD patterns and backscattered SEM images on representative samples (Figure A1-1 in Supporting Information). To be sure, optimizing the preparation of phase-pure samples will depend on a case-by-case basis for individual compounds. As detailed below, there is evidence that these compounds are substoichiometric. Maintaining a specific composition is also tricky because of volatilization losses of elements such as Cd, which are difficult to control. However, pressing the components into pellets before arc-melting helps minimize these volatilization losses.

The powder XRD patterns for all quaternary germanides $RE_4M_2XGe_4$ (X = Ag, Cd) prepared here were fit to monoclinic unit cells, with refined parameters listed in Table 2. Plots of the unit cell volumes as a function of *RE* generally show the expected decrease due to the lanthanide contraction (Figure 3-1). However, the trends are not as regular as in the previously reported In-containing series $RE_4M_2InGe_4$,[13–15] likely because the compounds show substantial variability in the levels of Ag or Cd deficiencies (x in the substoichiometric compositions $RE_4M_2X_{1-x}Ge_4$). The existence of these deficiencies was confirmed in selected compounds examined with single-crystal X-ray diffraction, as described later. In fact, the trends are quite irregular for the Ag-containing series, consistent with the tendency of Ag to exhibit such deficiencies in many of its compounds. On progressing along different series varying with *M*, the cell volumes generally decrease, following the trend in atomic sizes from Mn to Ni; the range of *RE* substitution also becomes more restricted so that the Ni-containing series forms only for the mid-lanthanides. These observations suggest that size factors limit the formation of these

quaternary germanides. A plot of radius ratios r_M/r_X and r_{RE}/r_X, where Pauling metallic radii R_1 were taken to evaluate these ratios,[41] supports this proposal (Figure 3-2), although the regions of formation differ for the Ag- vs. Cd-containing series. It should be possible to prepare the analogous germanides with the *M* component being substituted by heavier congeners (e.g., Ru, Rh, Ir), which would be predicted to be compatible with larger *RE* components.

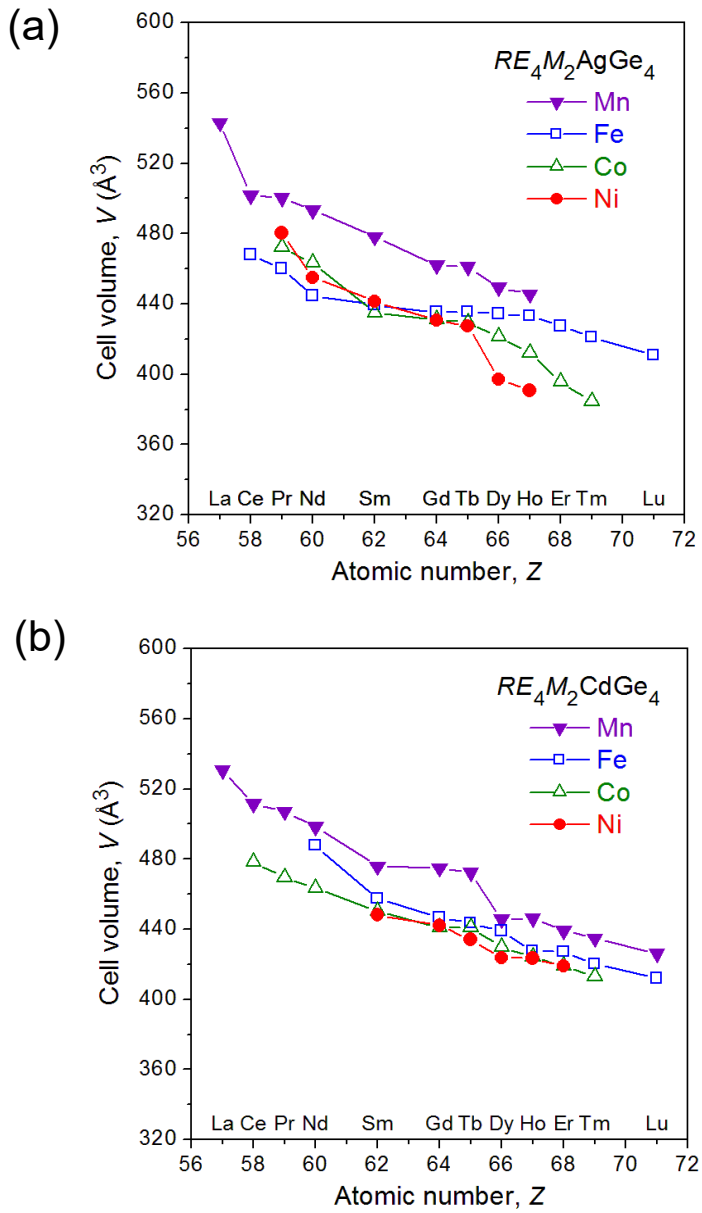

Figure 3-1. Plots of unit cell volumes for (a) $RE_4M_2AgGe_4$ and (b) $RE_4M_2CdGe_4$ (M = Mn–Ni).

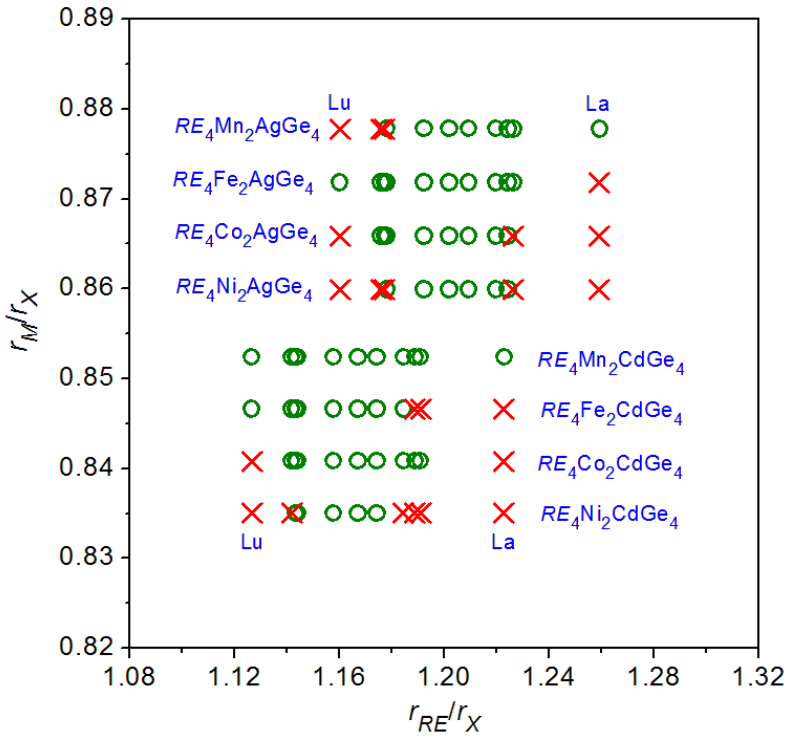

Figure 3-2. Structure map for $RE_4M_2AgGe_4$ and $RE_4M_2CdGe_4$ based on ratios of Pauling metallic radii (green circles are known phases; red crosses are unknown phases).

3.3.2 Structure of $RE_4M_2XGe_4$

The crystal structures of $Nd_4Mn_2AgGe_4$ and $Nd_4Mn_2CdGe_4$, selected as representative examples of $RE_4M_2XGe_4$, were determined from single-crystal X-ray diffraction data, and confirmed to be the monoclinic $Ho_4Ni_2InGe_4$-type structure.[13] This structure has been described in detail previously, including its relationships to ternary structures,[15] and we review here the salient features. This versatile structure, which is remarkable for exhibiting well-ordered sites within a quaternary intermetallic compound, can be viewed in different ways (Figure 3-3). It can be derived by cutting slabs from the tetragonal Mo_2FeB_2-type structure (which is adopted by many ternary germanides, such as RE_2CdGe_2 and RE_2InGe_2, and is built up of a stacking of 3^2434 nets) and shifting these slabs relative to each other.[14,15,17,42] This viewpoint highlights the presence of

Ge-centred trigonal prisms, which are commonly found in many intermetallic germanides, and *X*-centred tetragonal prisms. Alternatively, the structure can be regarded in terms of cationic *RE* atoms embedded within the tunnels of an anionic [M_2XGe$_4$] framework, which is built up of ladders of edge-sharing *M*Ge$_4$ tetrahedra extending along the *b*-direction and *X*Ge$_4$ square planes. Adjacent ladders are linked together via Ge$_2$ pairs (yellow bonds) to form infinite layers [M_2Ge$_4$] lying parallel to (001), and these layers in turn are connected through the *X* atoms. The coordination environment of 4 Ge and 8 *RE* atoms around the *X* atoms also generates a cuboctahedron, which share opposite square faces with neighbouring cuboctahedra to form a stack along the *b*-direction.

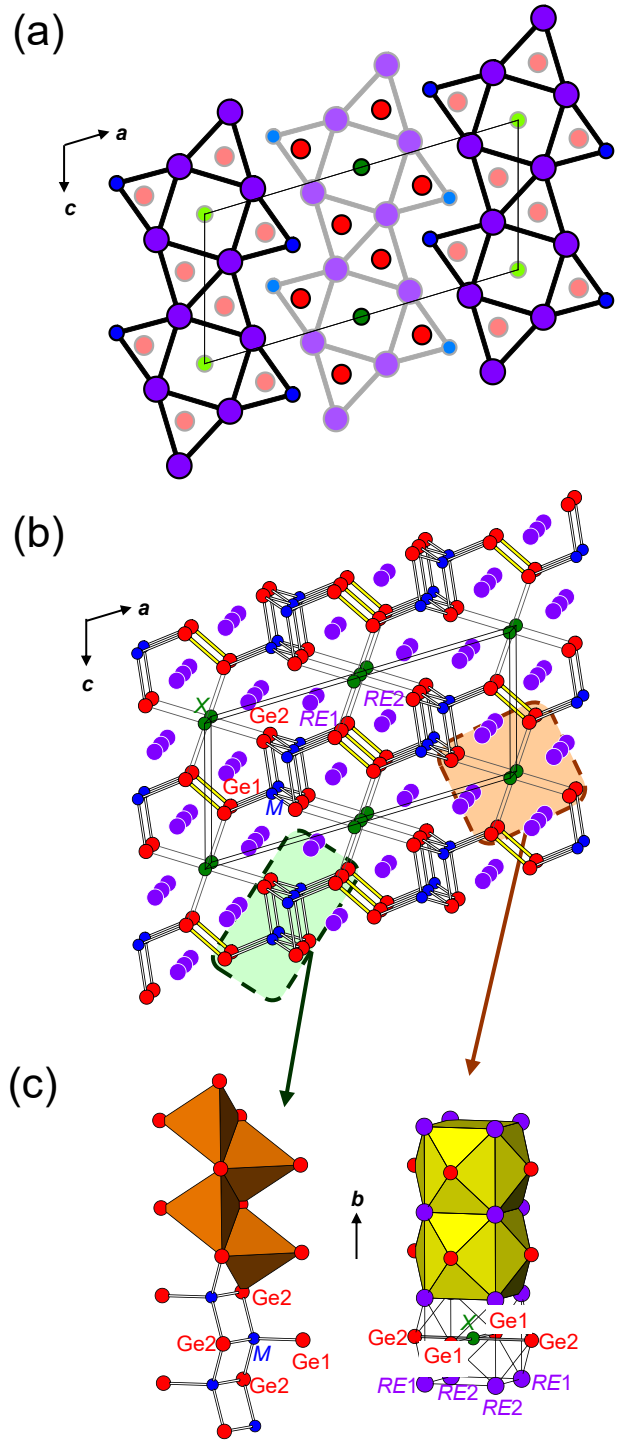

Figure 3-3. Structure of $RE_4M_2XGe_4$ (M = Mn–Ni; X = Ag, Cd). (a) Ge-centred trigonal prisms and X-centred tetragonal prisms. (b) Covalent $[M_2XGe_4]$ framework with RE atoms situated within tunnels. (c) Ladders of edge-sharing M-centred tetrahedra and stacks of X-centred cuboctahedra.

The structures of RE_4M_2XGe$_4$ are susceptible to additional complications. First, these compounds are definitely substoichiometric in X, as seen in Nd$_4$Mn$_2$Cd$_{0.86(1)}$Ge$_4$, but the level of deficiency is more pronounced than in the In-containing series (RE_4M_2In$_{0.93(2)–0.99(2)}$Ge$_4$).[14,15] The substoichiometry persists in the solid solutions with Si, as described below. Although further structure determinations are desirable, the persistent observation of the substoichiometry in the X site suggests that it is an inherent feature in all RE_4M_2XGe$_4$ compounds. Second, the M and X atoms may be disordered. The square planar coordination geometry of Ag or Cd atoms is certainly unusual, but it is not unprecedented.[43] Nevertheless, it is possible that such atoms may also occupy the tetrahedral sites. The structure determination of Nd$_4$Mn$_2$AgGe$_4$ reveals that not only do Ag atoms reside within the larger square planar site (with an occupancy of 0.83(1) Ag and distances of 2.958(1)–3.166(2) Å to surrounding Ge atoms), but they also mix with the Mn atoms within the smaller tetrahedral site (with occupancies of 0.78(1) Mn and 0.22(1) Ag, and distances of 2.621(1)–2.692(2) Å to surrounding Ge atoms). This phenomenon can be rationalized by the propensity of Ag to exhibit quite variable bond lengths; specifically, Ag–Ge bonds can range widely from 2.4 to 3.0 Å.[44] With both site deficiency and site disorder occurring, the resulting formula for this compound is Nd$_4$Mn$_{1.55(2)}$Ag$_{1.25(2)}$Ge$_4$, although for simplicity, we will continue to use the ideal formula RE_4M_2XGe$_4$ in subsequent discussion.

3.3.3 Disorder of Ge and Si

Silicides and germanides share many similarities, but it is not a truism that they always form isostructural compounds. In fact, solid solutions of silicides and germanides are not as common as one thinks.[45,46] To explore whether Si can substitute for Ge within the quaternary germanides RE_4M_2XGe$_4$, the mixed system Nd$_4$Mn$_2$Cd(Ge$_{1-y}$Si$_y$)$_4$ was chosen for investigation. Two intermediate members with nominal compositions Nd$_4$Mn$_2$CdGe$_2$Si$_2$ and

$Nd_4Mn_2CdGe_{1.5}Si_{2.5}$, as well as the silicide $Nd_4Mn_2CdSi_4$ were targeted, using the same preparative conditions as before. The desired compounds were obtained and single-crystal structure determinations confirmed that they adopt the monoclinic $Ho_4Ni_2InGe_4$-type structure as well. As in the parent germanides, all members examined in this solid solution also exhibit substoichiometry in the *X* site, so the formulas should strictly be written as $Nd_4Mn_2Cd_{1-x}(Ge_{1-y}Si_y)_4$. As the Si content is increased in $Nd_4Mn_2Cd(Ge_{1-y}Si_y)_4$, the structure evolves in an interesting way (Figure 3-4). Vegard's law is not followed, with the cell parameters for the intermediate members being greater than those for the end members. The unit cell volume first expands on progressing from $Nd_4Mn_2CdGe_4$ to $Nd_4Mn_2CdGe_2Si_2$, counter to expectations, and then contracts on progressing further to $Nd_4Mn_2CdSi_4$. Preferential site occupation is a typical reason for deviations from Vegard's law.[47] However, the refined occupancies of Ge and Si atoms within the two tetrel sites in the structure, *Tt*1 and *Tt*2, are close to the nominal compositions and vary nearly linearly with the loaded Si content. The gradual increase in the occupancy of the Cd site, from 0.86(1) in the all-Ge member to 0.97(1) in the all-Si member, may contribute to the expansion in the unit cell. The most compelling observation, however, comes from inspecting key interatomic distances in the structures. As smaller Si atoms are introduced in place of Ge atoms, the bonds within the *Tt*1–*Tt*1 pairs in the structure shorten, as do the average Mn–*Tt* distances within the Mn-centred tetrahedra, but to a lesser extent. In contrast, the Cd–*Tt* distances within the Cd-centred square planes lengthen. In an analysis of the previous In-containing series $RE_4M_2InGe_4$, we had proposed that the bonds within the $InGe_4$ square planes are weak and highly susceptible to distortion.[15] In a similar way, within the solid solution $Nd_4Mn_2Cd(Ge_{1-y}Si_y)_4$, it is important to satisfy the requirements of the stronger Mn–*Tt* and *Tt*–*Tt* bonds foremost, at the expense of the weaker Cd–*Tt* bonds. That is, as Si substitutes for Ge atoms, there is a contraction

of the individual [M_2Tt_2] layers that lie parallel to (001), but this effect is counteracted by an expansion accompanying the greater separation of these layers.

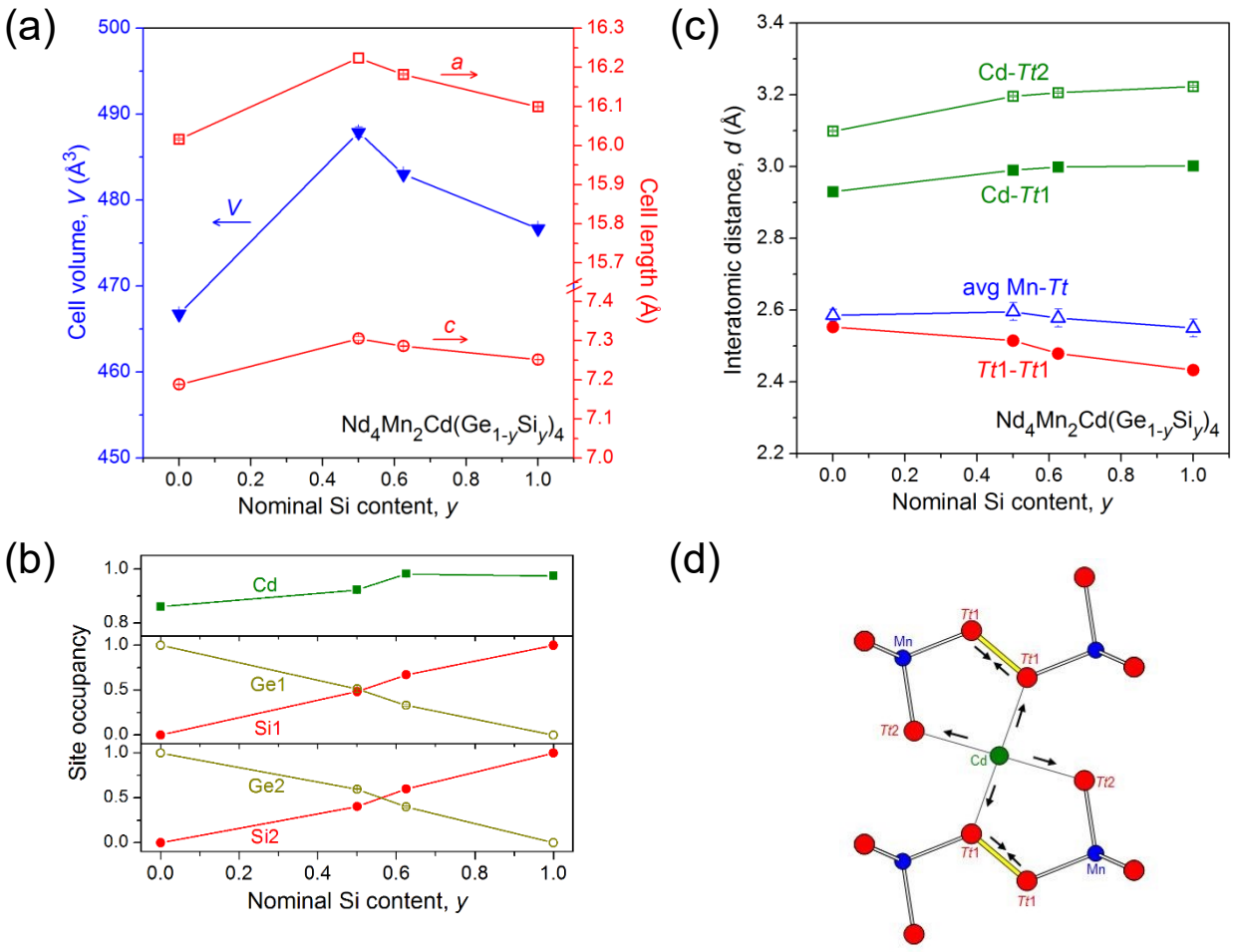

Figure 3-4. Plots of (a) selected cell parameters, (b) site occupancies, and (c) interatomic distances as a function of nominal Si content in the solid solution $Nd_4Mn_2Cd(Ge_{1-y}Si_y)_4$. (d) As the Si content increases, the $Tt1$–$Tt1$ pair shortens while the CdTt_4 square plane expands.

3.3.4 Electronic Structure

To examine the bonding in more detail in these new quaternary germanides and to draw comparisons to the previous In-containing compounds, non-spin-polarized electronic band structure calculations were carried out on idealized stoichiometric, ordered models of $La_4Mn_2AgGe_4$ and $La_4Mn_2CdGe_4$. These La-containing members were chosen to avoid

complications associated with partially occupied 4f orbitals. The density of states and crystal orbital Hamilton population curves are shown in Figure 3-5. The Fermi level lies within a broad manifold (from around –4 eV upwards in energy) characterized by significant mixing of Mn 3d, Ag or Cd 5s/5p, and Ge 4p states. The position of the Fermi level near a local maximum composed primarily of Mn 3d states suggests that, at least for these Mn-containing compounds, magnetic ordering is likely. Most of the La-based states lie well above the Fermi level, but they do contribute to the DOS below, especially around –2 eV. The 4d states of the Ag or Cd atoms are much more localized and completely filled within the narrow sharp spikes in the DOS, which lie quite deep in energy below the Fermi level at –4.3 or –8.8 eV, respectively, so they cannot influence the electrical properties significantly. Moreover, these 4d states participate little in bonding to the surrounding Ge atoms, as seen in the Ag–Ge or Cd–Ge COHP curves. Although many of the features of the electronic structures within the series $La_4Mn_2AgGe_4$, $La_4Mn_2CdGe_4$, and $La_4Mn_2InGe_4$ are similar, it is not a simple matter of raising the Fermi level by increasing the electron count, as a rigid band approximation would imply. As seen in the COHP curves and quantified by the integrated COHP values (Table 3-5), the Mn–Ge and Ge–Ge bonds are inherently the strongest ones within the structure and it is important to optimize them by ensuring that all bonding levels are occupied. In contrast, the Ag–Ge or Cd–Ge bonds are the weakest, corroborating the description above of how the structure can evolve by allowing these bonds to distort. Near the Fermi level, the Mn–Ge, Ag–Ge or Cd–Ge, and Ge–Ge interactions are nonbonding or only weakly antibonding. Depopulation of these levels (counterbalanced by the weakening of La–Ge bonding) thus provides a possible rationalization for why deficiencies readily occur in these compounds.

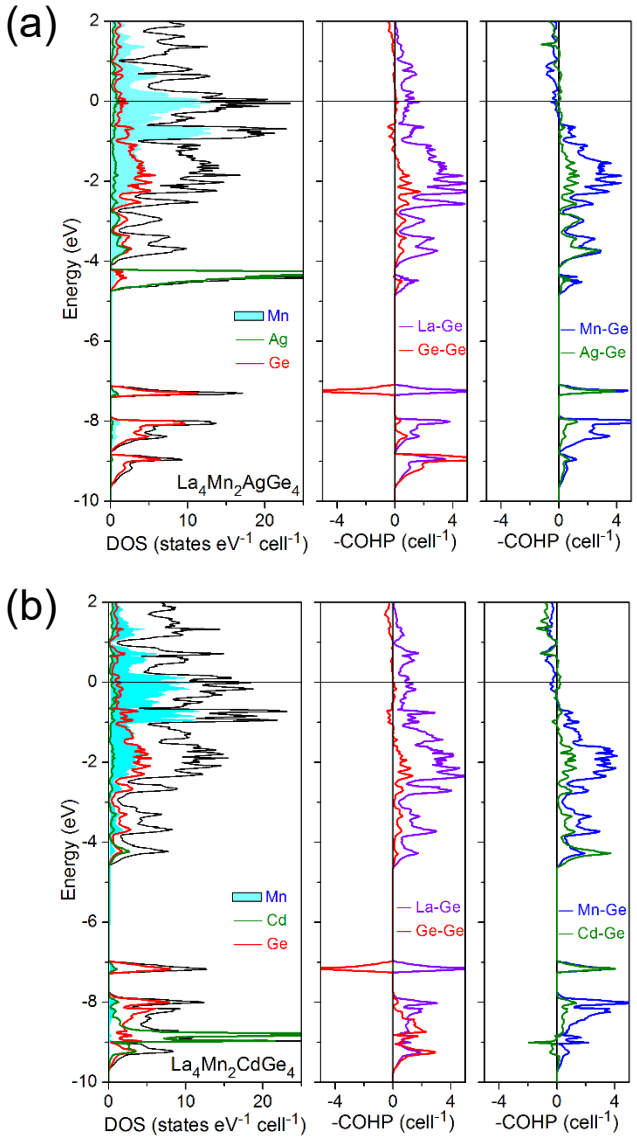

Figure 3-5. Density of states (DOS) and crystal orbital Hamilton population (COHP) curves for (a) $La_4Mn_2AgGe_4$ and (b) $La_4Mn_2CdGe_4$.

Table 3-5. –ICOHP Values for $La_4Mn_2AgGe_4$ and $La_4Cd_2AgGe_4$.

contact	–ICOHP (eV bond^{-1})	–ICOHP (eV cell^{-1})	contribution (%)
$La_4Mn_2AgGe_4$			
La–Ge	0.95	10.43	42.2
Mn–Ge	2.19	8.75	35.4
Ag–Ge	0.85	3.40	13.8
Ge–Ge	2.12	2.12	8.6
$La_4Mn_2CdGe_4$			
La–Ge	0.94	10.33	42.0
Mn–Ge	2.25	9.01	36.6
Cd–Ge	0.80	3.21	13.0
Ge–Ge	2.07	2.07	8.4

3.3.5 Thermal Conductivity

Intermetallic compounds typically exhibit high thermal conductivities (on the order of 10^2 W m^{-1} K^{-1}), which make them useful in applications such as high-temperature structural materials in which heat must be efficiently transferred.[48] On the other hand, this very characteristic normally rules them out as viable thermoelectric materials, which require low thermal conductivities. Although experimental measurements of thermal properties of intermetallics remain quite limited, the general trends are that the thermal conductivity tends to decrease with greater chemical complexity, deviations from ideal stoichiometry, and occurrence of disorder and defects, all of which are exhibited by these quaternary germanides $RE_4M_2XGe_4$. In a separate approach, machine-learning models have been recently developed for thermal conductivities and temperature-dependent heat capacities of inorganic solids.[24–27] With use of a random forest algorithm and an experimental data set of known materials, a thermoelectrics recommendation engine was built in which, among various properties, the thermal conductivity of new materials could be predicted solely based on their composition;[25] in particular, using these tools, we were

able to predict with high confidence (>95% probability) that any of these quaternary germanides would exhibit thermal conductivities lower than 10 W m^{-1} K^{-1}, so it is of interest to test these predictions. Because $Nd_4Mn_2InGe_4$ and $Nd_4Mn_2AgGe_4$ could be prepared in high purity, thermal measurements were made on these samples (Figure 3-6). The thermal conductivity was evaluated from temperature-dependent measurements of the thermal diffusivity and heat capacity through the relationship $\kappa = \rho\alpha C_p$. At elevated temperatures, the heat capacities of the samples are very nearly equal to the Dulong-Petit limits of 3*R* (0.251 J g^{-1} K^{-1} for $Nd_4Mn_2InGe_4$ and 0.253 J g^{-1} K^{-1} for $Nd_4Mn_2AgGe_4$). The baselines shown for the temperature-dependent heat capacities are predicted from machine learning [27] and the data points come from experimental measurements. Given the error and difficulty in measuring heat capacity, it has become common practice to simply use the 3*R* approximation over all temperatures when calculating the temperature-dependent thermal conductivity. On the other hand, in a recent work by Kauwe et al.,[27] it was shown that machine-learning predictions of heat capacity introduce significantly less error than the Dulong-Petit approximation as well as standard approaches such as Neumann-Kopp or cation/anion constituents calculations of heat capacity. In fact, the error of machine-learning predictions was less than 10% over all temperature ranges modeled, suggesting that it is on par with experimental determinations. Although the temperature dependence of the machine-learning results and experimental measurements may appear to be contrasting, they are within experimental error of each other. To calculate the thermal conductivities below 200 °C, the baseline values for heat capacity were used. As the temperature increases from 100 °C to 600 °C, the thermal conductivity gradually increases from 3.5 W m^{-1} K^{-1} to reach a plateau of about 7 W m^{-1} K^{-1} for both compounds.

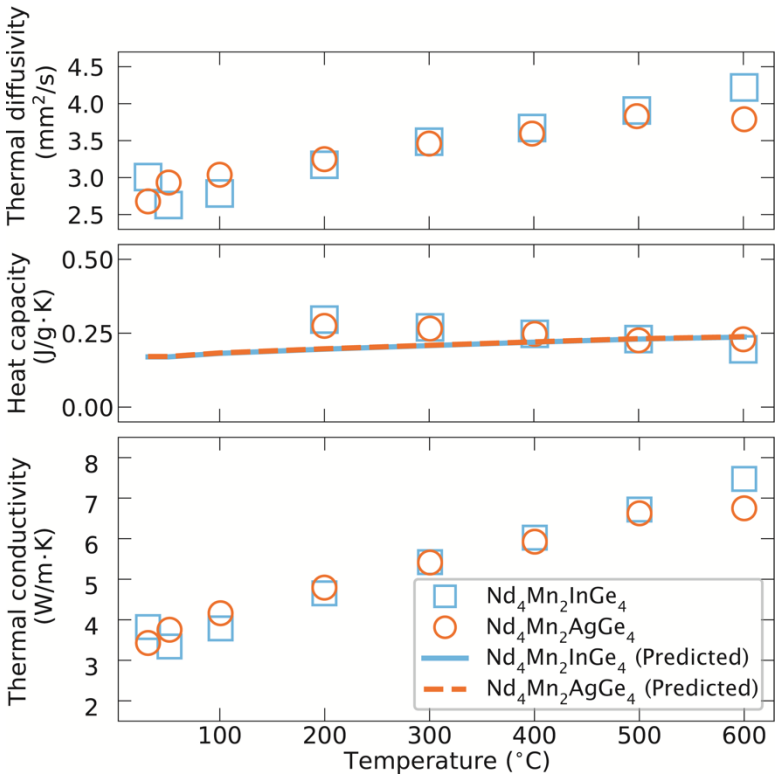

Figure 3-6. Thermal properties for $Nd_4Mn_2InGe_4$ and $Nd_4Mn_2AgGe_4$.

3.4 Conclusions

The number of quaternary germanides $RE_4M_2XGe_4$ adopting the ordered $Ho_4Ni_2InGe_4$-type structure has been more than doubled through the substitution of the *X* component, previously limited to In, with the late d-block elements Ag and Cd. Moreover, the elucidation of the complete solid solution $Nd_2Mn_2Cd(Ge_{1-x}Si_x)_4$ indicates that the corresponding quaternary silicides can be prepared. These results fulfill expectations that the $Ho_4Ni_2InGe_4$-type can accommodate considerable compositional versatility, which remains to be fully realized. Some of the key insights gained from the structural study of these germanides are that deficiencies in square planar *X* site persist and in fact, become more pronounced in the Ag- and Cd-containing members; that disorder of the *M* and *X* atoms within the tetrahedral site may occur if size factors permit, as

observed in $Nd_4Mn_{1.55(2)}Ag_{1.25(2)}Ge_4$ (which could also be represented as $Nd_4(Mn_{0.78(1)}Ag_{0.22(1)})_2Ag_{0.83(1)}Ge_4$); and that maintenance of strong *M*–*Tt* and *Tt*–*Tt* bonding within [M_2Tt_2] layers, at the expense of weak *X*–*Tt* bonding within the square planes, is an important driving force in the evolution of the solid solution $Nd_4Mn_2Cd(Ge_{1-y}Si_y)_4$. The hypothesis that atomic rattling may be occurring within the square planar *X* sites is not fulfilled: the displacement parameters of the *X* atoms are not overwhelmingly larger than those of the other sites. Nevertheless, electronic structure calculations indicate that the bonds to these *X* atoms are the weakest in the structure, which accounts for their flexibility. Low thermal conductivities were observed in $Nd_4Mn_2InGe_4$ and $Nd_4Mn_2AgGe_4$, in agreement with predictions from a machine-learning model, but this behaviour may originate not only from the large cage-like geometry around the *X* atoms, but also from the complexity of the structure and the occurrence of defects and disorder. The next steps in this investigation would be to optimize synthetic conditions of these germanides to improve crystal growth so that further single-crystal structures can be determined to verify that the substoichiometry in the *X* site is a general phenomenon, and to obtain pure phases for confirming predictions that low thermal conductivity should be observed in other $RE_4M_2XGe_4$ members.

3.5 References

1. Salamakha, P. S. Crystal structures and crystal chemistry of ternary rare-earth germanides. In *Handbook on the Physics and Chemistry of Rare Earths*; Gschneidner, K. A., Jr., Eyring, L., Eds.; Elsevier: Amsterdam, 1999; Vol. 27, 225–338.
2. Chen, J.; Semeniuk, K.; Feng, Z.; Reiss, P.; Brown, P.; Zou, Y.; Logg, P. W.; Lampronti, G. I.; Grosche, F. M. Unconventional superconductivity in the layered iron germanide YFe_2Ge_2. *Phys. Rev. Lett.* **2016**, *116*, 127001-1–127001-5.

3. Chajewski, G.; Samsel-Czekała, M.; Hackemer, A.; Wiśniewski, P.; Pikul, A. P.; Kaczorowski, D. Superconductivity in Y*TE*$_2$Ge$_2$ compounds (*TE* = d-electron transition metal). *Physica B* **2018**, *536*, 767–772.

4. Singh, Y.; Ramakrishnan, S. Magnetic ordering and superconductivity in the $R_2Ir_3Ge_5$ (*R* = Y, La, Ce–Nd, Gd–Tm, Lu) system. *Phys. Rev. B* **2004**, *69*, 174423-1–174423-13.

5. Pecharsky, V. K.; Gschneidner, K. A. Jr. Giant magnetocaloric effect in $Gd_5(Si_2Ge_2)$. *Phys. Rev. Lett.* **1997**, *78*, 4494–4497.

6. Steurer, W.; Dshemuchadse, J. *Intermetallics: Structures, Properties, and Statistics*; Oxford University Press: Oxford, 2016.

7. Wu, X.; Kanatzidis, M. G. *RE*AuAl$_4$Ge$_2$ and *RE*AuAl$_4$(Au$_x$Ge$_{1-x}$)$_2$ (*RE* = rare earth element): Quaternary intermetallics grown in liquid aluminum. *J. Solid State Chem.* **2005**, *178*, 3233–3242.

8. He, W.; Zeng, W.; Lin, G. Crystal structures of new $R_3CoAl_3Ge_2$ (*R* = Gd–Er) quaternary compounds and magnetic properties and lattice thermal expansion of $Gd_3CoAl_3Ge_2$. *J. Alloys Compd.* **2015**, *627*, 307–312.

9. Zhuravleva, M. A.; Pcionek, R. J.; Wang, X.; Schultz, A. J.; Kanatzidis, M. G. *REM*Ga$_3$Ge and $RE_3Ni_3Ga_8Ge_3$ (*M* = Ni, Co; *RE* = rare-earth element): New intermetallics synthesized in liquid gallium. X-ray, electron, and neutron structure determination and magnetism. *Inorg. Chem.* **2003**, *42*, 6412–6424.

10. Zhuravleva, M. A.; Kanatzidis, M. G. Polygallide $RE_2MGa_9Ge_2$ (*RE* = Ce, Sm; *M* = Ni, Co) phases grown in molten gallium. *Inorg. Chem.* **2008**, *47*, 9471–9477.

11. Subbarao, U.; Jana, R.; Chondroudi, M.; Balasubramanian, M.; Kanatzidis, M. G.; Peter, S. C. $Yb_7Ni_4InGe_{12}$: a quaternary compound having mixed valent Yb atoms grown from indium flux. *Dalton Trans.* **2015**, *44*, 5797–5804.

12. Chondroudi, M.; Peter, S. C.; Malliakas, C. D.; Balasubramanian, M.; Li, Q.; Kanatzidis, M. G. $Yb_3AuGe_2In_3$: An ordered variant of the YbAuIn structure exhibiting mixed-valent Yb behavior. *Inorg. Chem.* **2011**, *50*, 1184–1193.

13. Salvador, J. R.; Kanatzidis, M. G. Indium flux synthesis of $RE_4Ni_2InGe_4$ (*RE* = Dy, Ho, Er, and Tm): An ordered quaternary variation on the binary phase Mg_5Si_6. *Inorg. Chem.* **2006**, *45*, 7091–7099.

14. Oliynyk, A. O.; Stoyko, S. S.; Mar, A. Quaternary germanides $RE_4Mn_2InGe_4$ (*RE* = La–Nd, Sm, Gd–Tm, Lu). *Inorg. Chem.* **2013**, *52*, 8264–8271.

15. Oliynyk, A. O.; Stoyko, S. S.; Mar, A. Many metals make the cut: quaternary rare-earth germanides $RE_4M_2InGe_4$ (*M* = Fe, Co, Ni, Ru, Rh, Ir) and $RE_4RhInGe_4$ derived from excision of slabs in RE_2InGe_2. *Inorg. Chem.* **2015**, *54*, 2780–2792.

16. Oliynyk, A. O.; Djama-Kayad, K.; Mar, A. Investigation of phase equilibria in the quaternary Ce–Mn–In–Ge system and isothermal sections of the boundary ternary systems at 800 °C. *J. Alloys Compd.* **2015**, *622*, 837–841.

17. Tobash, P. H.; Lins, D.; Bobev, S.; Lima, A.; Hundley, M. F.; Thompson, J. D.; Sarrao, J. L. Crystal growth, structural, and property studies on a family of ternary rare-earth phases RE_2InGe_2 (*RE* = Sm, Gd, Tb, Dy, Ho, Yb). *Chem. Mater.* **2005**, *17*, 5567–5573.

18. Graf, T.; Felser, C.; Parkin, S. S. P. Simple rules for the understanding of Heusler compounds. *Prog. Solid State Chem.* **2011**, *39*, 1–50.

19. Sales, B. C.; May, A. F.; McGuire, M. A.; Stone, M. B.; Singh, D. J.; Mandrus, D. Transport, thermal, and magnetic properties of the narrow-gap semiconductor $CrSb_2$. *Phys. Rev. B* **2012**, *86*, 235136-1–235136-7.

20. Calta, N. P.; Im, J.; Rodriguez, A. P.; Fang, L.; Bulgaris, D. E.; Chasapis, T. C.; Freeman, A. J.; Kanatzidis, M. G. Hybridization gap and Dresselhaus spin splitting in $EuIr_4In_2Ge_4$. *Angew. Chem. Int. Ed.* **2015**, *54*, 9186–9191.

21. Calta, N. P.; Im, J.; Fang, L.; Chasapis, T. C.; Bulgaris, D. E.; Chung, D. Y.; Kwok, W.-K.; Kanatzidis, M. G. Hybridization gap in the semiconducting compound $SrIr_4In_2Ge_4$. *Inorg. Chem.* **2016**, *55*, 12477–12481.

22. Oliynyk, A. O.; Mar, A. Discovery of intermetallic compounds from traditional to machine-learning approaches. *Acc. Chem. Res.* **2018**, *51*, 59–68.

23. Graser, J.; Kauwe, S. K.; Sparks, T. D. Machine learning and energy minimization approaches for crystal structure predictions: A review and new horizons. *Chem. Mater.* **2018**, *30*, 3601–3612.

24. Sparks, T. D.; Gaultois, M. W.; Oliynyk, A.; Brgoch, J.; Meredig, B. Data mining our way to the next generation of thermoelectrics. *Scr. Mater.* **2016**, *111*, 10–15.

25. Gaultois, M. W.; Oliynyk, A. O.; Mar, A.; Sparks, T. D.; Mulholland, G. J.; Meredig, B. Perspective: Web-based machine learning models for real-time screening of thermoelectric materials properties. *APL Mater.* **2016**, *4*, 053213-1–053213-11. For the implementation of these tools, see *http://thermoelectrics.citrination.com*.

26. Oliynyk, A. O.; Sparks, T. D.; Gaultois, M. W.; Ghadbeigi, L.; Mar, A. $Gd_{12}Co_{5.3}Bi$ and $Gd_{12}Co_5Bi$, crystalline Doppelgänger with low thermal conductivities. *Inorg. Chem.* **2016**, *55*, 6625–6633.

27. Kauwe, S. K.; Graser, J.; Vazquez, A.; Sparks, T. D. Machine learning prediction of heat capacity for solid inorganics. *Integr. Mater. Manuf. Innov.* **2018**, *7*, 43–51.

28. Xue, D.; Balachandran, P. V.; Hogden, J.; Theiler, J.; Xue, D.; Lookman, T. Accelerated search for materials with targeted properties by adaptive design. *Nat. Commun.* **2016**, *7*, 11241-1–11241-9.

29. Balachandran, P. V.; Kowalski, B.; Sehirlioglu, A.; Lookman, T. Experimental search for high-temperature ferroelectric perovskites guided by two-step machine learning. *Nat. Commun.* **2018**, *9*, 1668-1–1668-9.

30. Zhuo, Y.; Mansouri Tehrani, A.; Brgoch, J. Predicting the band gaps of inorganic solids by machine learning. *J. Phys. Chem. Lett.* **2018**, *9*, 1668–1673.

31. Oliynyk, A. O.; Gaultois, M. W.; Hermus, M.; Morris, A. J.; Mar, A.; Brgoch, J. Searching for missing binary equiatomic phases: Complex crystal chemistry in the Hf–In system. *Inorg. Chem.* **2018**, *57*, 7966–7974.

32. Cao, B.; Adutwum, L. A.; Oliynyk, A. O.; Luber, E. J.; Olsen, B. C.; Mar, A.; Buriak, J. M. How to optimize materials and devices *via* design of experiments and machine learning: Demonstration using organic photovoltaics. *ACS Nano* **2018**, *12*, 7434–7444.

33. Mansouri Tehrani, A.; Oliynyk, A. O.; Parry, M.; Rizvi, Z.; Couper, S.; Lin, F.; Miyagi, L.; Sparks, T. D.; Brgoch, J. Machine learning directed search for ultraincompressible, superhard materials. *J. Am. Chem. Soc.* **2018**, *140*, 9844–9853.

34. Akselrud, L.; Grin, Yu. *WinCSD*: Software package for crystallographic calculations (Version 4). *J. Appl. Crystallogr.* **2014**, *47*, 803–805.

35. Sheldrick, G. M. *SHELXTL*, version 6.12; Bruker AXS Inc.: Madison, WI, 2001.

36. Gelato, L. M.; Parthé, E. *STRUCTURE TIDY* – a computer program to standardize crystal structure data. *J. Appl. Crystallogr.* **1987**, *20*, 139–143.

37. Spek, A. L. Structure validation in chemical crystallography. *Acta Crystallogr., Sect. D* **2009**, *65*, 148–155.

38. Tank, R.; Jepsen, O.; Burkhardt, A.; Andersen, O. K. *TB-LMTO-ASA Program*, version 4.7; Max Planck Institut für Festkörperforschung: Stuttgart, Germany, 1998.

39. Dronskowski, R.; Blöchl, P. E. Crystal orbital Hamilton populations (COHP). Energy-resolved visualization of chemical bonding in solids based on density-functional calculations. *J. Phys. Chem.* **1993**, *97*, 8617–8624.

40. Cape, J. A.; Lehman, G. W. Temperature and finite pulse-time effects in the flash method for measuring thermal diffusivity. *J. Appl. Phys.* **1963**, *34*, 1909–1913.

41. Pauling, L. *The Nature of the Chemical Bond*, 3rd ed.; Cornell University Press: Ithaca, NY, 1960.

42. Guo, S. P.; Meyers, J. J.; Tobash, P. H.; Bobev, S. Eleven new compounds in the *RE*–Cd–Ge systems (*RE* = Pr, Nd, Sm, Gd–Yb; Y): Crystal chemistry of the RE_2CdGe_2 series. *J. Solid State Chem.* **2012**, *192*, 16–32.

43. Young, A. G.; Hanton, L. R. Square planar silver(I) complexes: A rare but increasingly observed stereochemistry for silver(I). *Coord. Chem. Rev.* **2008**, *252*, 1346–1386.

44. *Pearson's Crystal Data: Crystal Structure Database for Inorganic Compounds (on DVD)*, release 2015/16; ASM International: Materials Park, OH, 2016.

45. Bażela, W.; Szytuła, A.; Todorović, J.; Zięba, A. Crystal and magnetic structure of the $NiMnGe_{1-n}Si_n$ system. *Phys. Status Solidi A* **1981**, *64*, 367–378.

46. Cordruwisch, E.; Kaczorowski, D.; Saccone, A.; Rogl, P.; Ferro, R. Constitution, structural chemistry, and magnetism of the ternary system Ce–Ag–Ge. *J. Phase Equilib.* **1999**, *20*, 407–422.

47. Castellanos, M.; West, A. R. Deviations from Vegard's law in oxide solid solutions. *J. Chem. Soc., Faraday Trans. 1* **1980**, *76*, 2159–2169.

48. Terada, Y.; Okhubo, K.; Mohri, T.; Suzuki, T. Thermal conductivity of intermetallic compounds with metallic bonding. *Mater. Trans.* **2002**, *43*, 3167–3176.

Chapter 4 Conclusion

4.1 Ternary Germanides

Ternary germanides in the *RE*–*M*–Ge systems have been previously investigated largely with first-row transition metals for the *M* component, and less so for the second- and third-row metals. As part of the goal to extend these studies, the Ce–Rh–Ge system has been further investigated, and three new Rh-rich phases $Ce_3Rh_{11}Ge_5$, $CeRh_5Ge_3$, and $CeRh_3Ge_2$ were identified. $Ce_3Rh_{11}Ge_5$ and $CeRh_5Ge_3$ adopt hexagonal structures whereas $CeRh_3Ge_2$ adopts an orthorhombic structure. The common motif in these structures are hexagonal prisms of Rh and Ge atoms, centred by Ce atoms. An important finding in this work was the verification of anionic Rh species within these structures, as confirmed by Bader charge analysis. Some of the difficulties in the structure determination related to residual electron density in these heavy-atom structures, but the atom assignments were confirmed with the aid of electron localization functions.

4.2 Quaternary Germanides

Ternary germanides that contain various combinations of rare-earth, transition metals, and p-block metalloids are well known to exhibit various interesting physical properties. As more components are introduced, the complexity of the structures may increase, allowing greater control over properties. However, synthesizing an ordered quaternary compound is not so easy to accomplish. As part of the effort to explore new quaternary germanides, arc-melting has been applied as an effective means of synthesis. Previously, a large family of quaternary rare-earth germanides $RE_4M_2InGe_4$, with over 60 members, were prepared in this manner. In this thesis, 73 new quaternary germanides $RE_4M_2XGe_4$ (*M* = Mn–Ni; *X* = Ag, Cd) were prepared which adopt the same monoclinic $Ho_4Ni_2InGe_4$-type structure. This investigation confirms that the structure type can be extended to Ag and Cd can replace In as the *X*-component. Also, given the similar size of

Si and Ge, a complete solid solution $Nd_4Mn_2Cd(Ge_{1-x}Si_x)_4$ was prepared, indicating that the corresponding quaternary silicides are likely to exist for other combinations of elements. From single-crystal diffraction data, a pronounced deficiency in the square planar *X* site was established. Furthermore, if *M* and *X* are similar in size, they may disorder, as occurs in $Nd_4(Mn_{0.78(1)}Ag_{0.22(1)})_2Ag_{0.83(1)}Ge_4$. Electronic structure calculations demonstrate that the bonds to the *X* atoms are the weakest in the structure and adapt to the rest of the framework. Unlike other intermetallic compounds, which typically show high thermal conductivity, $Nd_4Mn_2InGe_4$ was found to exhibit relatively low thermal conductivity, in agreement with predictions from a machine-learning model. The hypothesis of rattling of *X* atoms within a large cage, which could explain the low thermal conductivity behaviour, is not fulfilled because the displacement parameter for this site is not overwhelmingly larger than in the other sites. The low thermal conductivity probably arises from other factors, such as the structural complexity and the presence of defects.

4.3 Future Work

The next steps in the investigation of the ternary Ce–Rh–Ge system are to synthesize phase-pure samples to conduct physical property measurements, because interesting magnetic properties are anticipated, and to continue exploring other parts of the phase diagram. At this stage, a complete phase diagram for this system will require much more work because the number of ternary phases is extremely large.

Extension to other ternary systems such as *RE*–Co–Ge has been initiated, in which *RE* is replaced by other rare-earth metals and Rh with other transition metals. Because Co-containing intermetallics are frequently ferromagnetic, combining them with *RE* metals is likely to lead to strong ferromagnetism. Preliminary results suggest the formation of a series of compounds with

hexagonal structures, and phase-pure samples have been obtained for $CeCo_{4.6}Ge_{0.4}$ and $TbCo_{4.6}Ge_{0.4}$. Magnetic measurements on $TbCo_{4.6}Ge_{0.4}$ reveal the occurrence of several complex transitions.

Extension of the quaternary germanides will require optimization of the synthesis and crystal growth, but this is difficult because the substoichiometry of the *X* site needs to be established for each specific member. It will be interesting to prepare phase-pure samples for the other members to confirm if low thermal conductivity is also found more generally within this series. Preparation of the quaternary silicides $RE_4M_2X\mathrm{Si}_4$ is also now underway.

Bibliography

1. Cinca, N.; Lima, C. R. C.; Guilemany, J. M. An overview of intermetallics research and application: Status of thermal spray coatings. *J. Mater. Res. Technol.* **2013**, *2*, 75–86.
2. Huang, W. M.; Ding, Z.; Wang, C. C.; Wei, J.; Zhao, Y.; Purnawali, H. Shape memory materials. *Mater. Today.* **2010**, *13*, 54–61.
3. Miyazaki, S.; Duerig, T. W.; Melton, K. N. *Engineering Aspects of Shape Memory Alloys*; Butterworth: London, 1990.
4. Lipscomb, I. P.; Nokes, L. D. *The Application of Shape Memory Alloys in Medicine*; Wiley-Blackwell: Sullfork, 1996.
5. Matthias, B. T.; Geballe, T. H.; Geller, S.; Corenzwit, E. Superconductivity of Nb_3Sn. *Phys. Rev.* **1954**, *95*, 1435–1435.
6. Kunzler, J. E.; Buehler, E.; Hsu, F. A.; Wernick, J. H. Superconductivity in Nb_3Sn at high current density in a magnetic field of 88 kgauss. *Phys. Rev. Lett.* **1961**, *6*, 89–91.
7. Han, M. K.; Jin, Y.; Lee, D. H.; Kim, S. J. Thermoelectric properties of Bi_2Te_3: CuI and the effect of its doping with Pb atoms. *Materials*. **2017**, *10*, 1235-1–1235-10.
8. Koehler, W. C. Magnetic properties of rare-earth metals and alloys. *J. Appl. Phys.* **1965**, *36*, 1078–1087.
9. Szlawska, M.; Majewicz, M.; Kaczorowski, D. Ferromagnetic ordering in single-crystalline U_2RhSi_3 with fully ordered crystal structure. *J. Alloys Compd.* **2016**, *662*, 208–212.
10. Petrovic, C.; Pagliuso, P. G.; Hundley, M. F.; Movshovich, R.; Sarrao, J. L.; Thompson, J. D.; Fisk, Z.; Monthoux, P. Heavy-fermion superconductivity in $CeCoIn_5$ at 2.3 K. *J. Phys. Cond. Mat.* **2001**, *13*, L337–L342.

11. Steglich, F.; Aarts, J.; Bredl, C. D.; Lieke, W.; Meschede, D.; Franz, W.; Schäfer, H. Superconductivity in the presence of strong pauli paramagnetism: $CeCu_2Si_2$. *Phys. Rev. Lett*. **1979**, *43*, 1892–1896.

12. Smigelskas, A. D.; Kirkendall, E. O. Zinc diffusion in alpha brass. *Trans. AIME* **1947**, *171*, 130–142.

13. Schenk, P.; Brauer, G. *Handbook of Preparative Inorganic Chemistry*, 2nd ed.; Academic Press: London, 1963.

14. Moore, D. M.; Reynolds, R. C. *X-ray Diffraction and the Identification and Analysis of Clay Minerals*; Oxford University Press: Oxford, 1989.

15. Ladd, M.; Palmer, R. *Structure Determination by X-ray Crystallography*, 5th ed.; Springer: New York, 2013.

16. West, A. R. *Basic Solid State Chemistry*, 2nd ed.; Wiley: New York, 1999.

17. Eckert, M. Max von Laue and the discovery of X-ray diffraction in 1912. *Ann. Phys.* **2012**, *524*, A83–A85.

18. Bragg, W. H.; Bragg, W. L. The reflection of X-rays by crystals. *Proc. Royal. Soc. A* **1913**, *88*, 428–438.

19. Massa, W. *Crystal Structure Determination*, 2nd ed.; Springer: Berlin, 2004.

20. Goldstein, J. I.; Newbury, D. E.; Echlin, P.; Joy, D. C.; Fiori, C.; Lifshin, E. *Scanning Electron Microscopy and X-Ray Microanalysis*, 3rd ed.; Springer: New York, 2003.

21. Russ, J. C. *Fundamentals of Energy Dispersive X-ray Analysis*; Butterworth: London, 1984.

22. Dronskowski, R. *Computational Chemistry of Solid State Materials*; Wiley-VCH: Weinheim and New York, 2005.

23. Tank, R.; Jepsen, O.; Burkhardt, A.; Andersen, O. K. *TB-LMTO-ASA Program*, version 4.7; Max Planck Institut für Festkörperforschung: Stuttgart, Germany, 1998.

24. Dronskowski, R.; Blöchl, P. E. Crystal orbital Hamilton populations (COHP): Energy-resolved visualization of chemical bonding in solids based on density-functional calculations. *J. Phys. Chem*. **1993**, *97*, 8617–8624.

25. Zhang, D.; Oliynyk, A. O.; Duarte, G. M.; Iyer, A. K.; Ghadbeigi, L.; Kauwe, S. K.; Sparks, T. D.; Mar, A. Not just par for the course: 73 quaternary germanides RE_4M_2XGe$_4$ (*RE* = La–Nd, Sm, Gd–Tm, Lu; *M* = Mn–Ni; *X* = Ag, Cd) and the search for intermetallics with low thermal conductivity. *Inorg. Chem.* **2018**, *57*, 14249–14259.

26. Berman, R. The thermal conductivity of dielectric solids at low temperatures. *Adv. Phys.* **1953**, *2*, 103–140.

27. Cape, J. A.; Lehman, G. W. Temperature and finite pulse-time effects in the flash method for measuring thermal diffusivity. *J. Appl. Phys.* **1963**, *34*, 1909–1913.

28. Parker, W. J.; Jenkins, R. J.; Butler, C. P.; Abbott, G. L. Flash method of determining thermal diffusivity, heat capacity, and thermal conductivity. *J. Appl. Phys.* **1961**, *32*, 1679–1684.

29. Steurer, W.; Dshemuchadse, J. *Intermetallics: Structures, Properties, and Statistics*; Oxford University Press: Oxford, 2016.

30. Venturini, G.; Méot-Meyer, M.; Marêché, J. F.; Malaman, B.; Roques, B. De nouveaux isotypes de $U_2Co_3Si_5$ ou $Lu_2Co_3Si_5$ dans les systems *R*–*T*–Ge (*R* = elements des terres rares; *T* = Ru, Co, Rh, Ir). Supraconductivite de $Y_2Ir_3Ge_5$. *Mater. Res. Bull.* **1986**, *21*, 33–39.

31. Singh, Y.; Ramakrishnan, S. Magnetic ordering and superconductivity in the $R_2Ir_3Ge_5$ (*R* = Y, La, Ce–Nd, Gd–Tm, Lu) system. *Phys. Rev. B* **2004**, *69*, 174423-1–174423-13.

32. Kong, H.; Shi, X.; Uher, C.; Morelli, D. T. Thermoelectric properties of rare earth–ruthenium–germanium compounds. *J. Appl. Phys.* **2007**, *102*, 023702-1–023702-5.

33. Morozkin, A. V.; Seropegin, Y. D.; Bodak, O. I. Phase equilibria in the Sm–{Ru, Rh}–{Si, Ge} systems at 870 K. *J. Alloys Compd.* **1996**, *234*, 143–150.

34. Seropegin, Y. D.; Gribanov, A. V.; Bodak, O. I. Isothermal cross-section of the Ce–Pd–Ge phase diagram at 600 °C. *J. Alloys Compd.* **1998**, *269*, 157–161.

35. Bodak, O. I.; Pecharskij, V. K.; Sologub, O. L.; Rybakov, V. B. New ternary ruthenium germanides. *Izv. Akad. Nauk SSSR, Met.* **1990**, *5*, 217–219.

36. Shapiev, B. I. *Dissertation*; Moscow State University: Moscow, 1993.

37. Rogl, P.; Chevalier, B.; Besnus, M. J.; Etourneau, J. Magnetic and electrical properties of the equiatomic cerium germanides Ce*M*Ge (*M* = Rh, Ir, Pd, Pt). *J. Magn. Magn. Mater.* **1989**, *80*, 305–310.

38. Muro, Y.; Eom, D.; Takeda, N.; Ishikawa, M. Contrasting Kondo-lattice behavior in Ce*T*Si_3 and Ce*T*Ge_3 (*T* = Rh and Ir). *J. Phys. Soc. Jpn.* **1998**, *67*, 3601–3604.

39. Hirose, Y.; Nishimura, N.; Honda, F.; Sugiyama, K.; Hagiwara, M.; Kindo, K.; Takeuchi, T.; Yamamoto, E.; Haga, Y.; Matsuura, M.; Hirota, K.; Yasui, A.; Yamagami, H.; Settai, R.; Ōnuki, Y. Magnetic and superconducting properties of $CeRhGe_2$ and $CePtSi_2$. *J. Phys. Soc. Jpn.* **2011**, *80*, 024711-1–024711-12.

40. Sheldrick, G. M. *SHELXTL*, version 6.12; Bruker AXS Inc.: Madison, WI, 2001.

41. Bruker AXS (2008): *TOPAS* V4: General profile and structure analysis software for powder diffraction data. - User's Manual, Bruker AXS, Karlsruhe, Germany.

42. Kresse, G.; Furthmüller, J. Efficient iterative schemes for Ab Initio total-energy calculations using a plane-wave basis set. *Phys. Rev. B* **1996**, *54*, 11169−11186.

43. Kresse, G.; Joubert, D. From ultrasoft pseudopotentials to the projector augmented-wave method. *Phys. Rev. B* **1999**, *59*, 1758−1775.

44. Kohout, M.; Wagner, F. R.; Grin, Y. Electron localization function for transition-metal compounds. *Theor. Chem. Acc*. **2002**, *108*, 150−156.

45. Grin, Y.; Savin, A.; Silvi, B. The ELF perspective of chemical bonding. In *The Chemical Bond: Fundamental Aspects of Chemical Bonding*; Frenking, G., Shaik, S., Eds.; Wiley-VCH Verlag GmbH & Co. KGaA: Weinheim, Germany, 2014, 345−382.

46. Kohout, M.; Savin, A. Influence of core-valence separation of electron localization function. *J. Comput. Chem.* **1997**, *18*, 1431−1439.

47. Tang, W.; Sanville, E.; Henkelman, G. A grid-based bader analysis algorithm without lattice bias. *J. Phys.: Condens. Matter*. **2009**, *21*, 84204-1–84204-7.

48. Andrusyak, R. I. *Sov. Phys. Crystallogr*. **1988**, *33*, 599–600.

49. Gladyshevskii, R. E.; Strusievicz, O. R.; Cenzual, K.; Parthé, E. Structure of $Gd_3Ru_4Al_{12}$, a new member of the $EuMg_{5.2}$ structure family with minority-atom clusters. *Acta Crystallogr., Sect. B* **1993**, *49*, 474–478.

50. Morozkin, A. V.; Knotko, A. V.; Yapaskurt, V. O.; Yuan, F.; Mozharivskyj, Y.; Pani, M.; Provino, A.; Manfrinetti, P. The Ho–Ni–Ge system: Isothermal section and new rare-earth nickel germanides. *J. Solid State Chem.* **2015**, *225*, 193–201.

51. Gladyshevskii, E. I. Crystal structure of the digermanide of rare earth elements. *J. Struct. Chem.* **1964**, *5*, 523–529.

52. Yakinthos, J. K. Crystal and magnetic structures of $TmFe_2Si_2$ and $TmNi_2Ge_2$ compounds. Influence of the d-metal charge on the anisotropy direction of the RT_2X_2 (R = rare earth, T = 3d or 4d metal and X = Si, Ge) compounds. *J. Magn. Magn. Mater.* **1991**, *99*, 123–132.

53. Marazza, R.; Ferro, R.; Rambaldi, G.; Zanicchi, G. Some phases in ternary alloys of thorium and uranium with the Al_4Ba-$ThCu_2Si_2$-type structure. *J. Less. Common Met.* **1977**, *53*, 193–197.

54. Mishra, V.; Oliynyk, A. O.; Subbarao, U.; Sarma, S. C.; Mumbaraddi, D.; Roy, S.; Peter, S. C. Complex crystal chemistry of $Yb_6(CuGa)_{50}$ and $Yb_6(CuGa)_{51}$ grown at different synthetic conditions. *Cryst. Growth Des*. **2018**, *18*, 6091–6099.

55. Oliynyk, A. O.; Mar, A. Rare-earth manganese germanides $RE_{2+x}MnGe_{2+y}$ (*RE* = La, Ce) built from four-membered rings and *stellae quadrangulae* of Mn-centred tetrahedra. *J. Solid State Chem*. **2013**, *206*, 60–65.

56. Oliynyk, A. O.; Sparks, T. D.; Gaultois, M. W.; Ghadbeigi, L.; Mar, A. $Gd_{12}Co_{5.3}Bi$ and $Gd_{12}Co_5Bi$, crystalline doppelgänger with low thermal conductivities. *Inorg. Chem.* **2016**, *55*, 6625–6633.

57. Morozkin, A. V.; Bogdanov, A. E.; Welter, R. New RRh_5Ge_3 compounds of the new $SmRh_5Ge_3$ structure type and their magnetic properties (*R* = Sm, Gd, Tb). *J. Alloys Compd*. **2002**, *340*, 49–53.

58. Yarmolyuk, Y. P.; Akselrud, L. G.; Gladyshevskii, E. I. Crystal structures of UCo_5Si_3 and $ZrCo_5Si_3$. *Sov. Phys.Crystallogr.* **1978**, *23*, 942–945.

59. Morozkin, A. V.; Seropegin, Y. D.; Sviridov, I. A.; Bodak, O. I. Crystallographic data for new ternary UCo_5Si_3-type RRh_5Si_3 (*R* = Sm, Gd–Tm) compounds. *J. Alloys Compd*. **1998**, *274*, L1–L5.

60. Vosswinkel, D.; Niehaus, O.; Rodewald, U. C.; Poettgen, R. Bismuth flux growth of $CeRh_6Ge_4$ and $CeRh_2Ge_2$ single crystals. *Z. Nat. Forsch. B* **2012**, *67*, 1241–1247.

61. Sheldrick, G. M. (2008). *CELL_NOW*. Version 2008/4. Georg-August-Universität Göttingen, Göttingen, Germany.

62. Vosswinkel, D.; Poettgen, R. Synthesis of $Ce_2Rh_3Ge_5$ crystals from a bismuth flux. *Z. Nat. Forsch. B* **2013**, *68*, 301–305.

63. Kawai, T.; Muranaka, H.; Measson, M. A.; Shimoda, T.; Doi, Y.; Matsuda, T. D.; Haga, Y.; Knebel, G.; Lapertot, G.; Aoki, D.; Flouquet, J.; Takeuchi, T.; Settai, R.; Ōnuki, Y. Magnetic and superconducting properties of Ce*TX*$_3$ (*T*: transition metal and *X*: Si and Ge) with non-centrosymmetric crystal structure. *J. Phys. Soc. Jpn*. **2008**, *77*, 064716-1–064716-9.

64. Sologub, O. L.; Salamakha, P. S.; Godart, C. Formation, crystal structure and magnetism of ternary compounds Ce_5MGe_2 (*M* = Co, Ni, Ru, Rh, Pd, Ir, Pt). *J. Alloys Compd.* **2000**, *307*, 31–39.

65. Oliynyk, A. O.; Stoyko, S. S.; Mar, A. Many metals make the cut: quaternary rare-earth germanides $RE_4M_2InGe_4$ (*M* = Fe, Co, Ni, Ru, Rh, Ir) and $RE_4RhInGe_4$ derived from excision of slabs in RE_2InGe_2. *Inorg. Chem*. **2015**, *54*, 2780–2792.

66. Oliynyk, A. O.; Stoyko, S. S.; Mar, A. Quaternary germanides $RE_4Mn_2InGe_4$ (*RE* = La–Nd, Sm, Gd–Tm, Lu). *Inorg. Chem*. **2013**, *52*, 8264–8271.

67. Oliynyk, A. O.; Stoyko, S. S.; Mar, A. Ternary rare-earth ruthenium and iridium germanides $RE_3M_2Ge_3$ (*RE* = Y, Gd–Tm, Lu; *M* = Ru, Ir). *J. Solid State Chem*. **2013**, *202*, 241–249.

68. Shapiev, B. I.; Sologub, O. L.; Seropegin, J. D.; Bodak, O. I.; Salamakha, P. S. Crystal structure of the compound $CeRh_{1-x}Ge_{2+x}$ (x = 0.325). *J. Less. Common Met.* **1991**, *175*, L1–L4.

69. Gladyshevskii, R. E.; Zhao, J. T.; Parthé, E. $Ce_3Rh_2Ge_2$ and isotypes with the orthorhombic $La_3Ni_2Ga_2$ type. *Acta Crystallogr., Sect. C* **1992**, *48*, 10–13.

70. Hovestreydt, E.; Engel, N.; Klepp, K.; Chabot, B.; Parthé, E. Equiatomic ternary rare earth-transition metal silicides, germanides and gallides. *J. Less. Common Met.* **1982**, *85*, 247–274.

71. Rogl, P.; Chevalier, B.; Etourneau, J. Structural chemistry and magnetic properties of ternary germanides $Ce_3Rh_4Ge_4$ and $Ce_3Rh_3IrGe_4$. *J. Solid State Chem.* **1990**, *88*, 429–434.

72. Salamakha, P. S.; Sologub, O. L. New ternary rare earth–rhodium–germanides: $Ce_4Rh_{13}Ge_9$ and Ho_2RhGe_2. *J. Alloys Compd.* **1999**, *287*, L1–L3.

73. Venturini, G.; Méot-Meyer, M.; Malaman, B.; Roques, B. De nouvelles séries de germaniures, isotypes de $Yb_3Rh_4Sn_{13}$ et $BaNiSn_3$, dans les systèmes ternaires *TR*–*T*–Ge où *TR* est un élément des terres rares et *T* ≡ Co, Rh, Ir, Ru, Os. *J. Less. Common Met.* **1985**, *113*, 197–204.

74. Francois, M.; Venturini, G.; Marêché, J. F.; Malaman, B.; Roques, B. De nouvelles séries de germaniures, isotypes de $U_4Re_7Si_6$, $ThCr_2Si_2$ et $CaBe_2Ge_2$, dans les systèmes ternaires *R*–*T*–Ge où *R* est un élément des terres rares et *T* ≡ Ru, Os, Rh, Ir: supraconductivité de $LaIr_2Ge_2$. *J. Less. Common Met*. **1985**, *113*, 231–237.

75. Kalsi, D.; Subbarao, U.; Rayaprol, S.; Peter, S. C. Structural and magnetic properties in the polymorphs of $CeRh_{0.5}Ge_{1.5}$. *J. Solid State Chem.* **2014**, *212*, 73–80.

76. Oliynyk, A. O.; Adutwum, L. A.; Harynuk J. J.; Mar, A. Classifying crystal structures of binary compounds *AB* through cluster resolution feature selection and support vector machine analysis. *Chem. Mater*. **2016**, *28*, 6672–6681.

77. Lotfi, S.; Oliynyk, A. O.; Brgoch, J. Polyanionic gold–tin bonding and crystal structure preference in $REAu_{1.5}Sn_{0.5}$ (*RE* = La, Ce, Pr, Nd). *Inorg. Chem.* **2018**, *57*, 10736–10743.

78. Smetana, V.; Corbett, J. D.; Miller, G. J. Four polyanionic compounds in the K−Au−Ga system: A case study in exploratory synthesis and of the art of structural analysis. *Inorg. Chem.* **2012**, *51*, 1695–1702.

79. Salamakha, P. S. Crystal structures and crystal chemistry of ternary rare-earth germanides. In *Handbook on the Physics and Chemistry of Rare Earths*; Gschneidner, K. A., Jr., Eyring, L., Eds.; Elsevier: Amsterdam, 1999; Vol. 27, 225–338.

80. Chen, J.; Semeniuk, K.; Feng, Z.; Reiss, P.; Brown, P.; Zou, Y.; Logg, P. W.; Lampronti, G. I.; Grosche, F. M. Unconventional superconductivity in the layered iron germanide YFe_2Ge_2. *Phys. Rev. Lett.* **2016**, *116*, 127001-1–127001-5.

81. Chajewski, G.; Samsel-Czekała, M.; Hackemer, A.; Wiśniewski, P.; Pikul, A. P.; Kaczorowski, D. Superconductivity in YTE_2Ge_2 compounds (*TE* = d-electron transition metal). *Physica B* **2018**, *536*, 767–772.

82. Pecharsky, V. K.; Gschneidner, K. A. Jr. Giant magnetocaloric effect in $Gd_5(Si_2Ge_2)$. *Phys. Rev. Lett.* **1997**, *78*, 4494–4497.

83. Wu, X.; Kanatzidis, M. G. $REAuAl_4Ge_2$ and $REAuAl_4(Au_xGe_{1-x})_2$ (*RE* = rare earth element): Quaternary intermetallics grown in liquid aluminum. *J. Solid State Chem.* **2005**, *178*, 3233–3242.

84. He, W.; Zeng, W.; Lin, G. Crystal structures of new $R_3CoAl_3Ge_2$ (*R* = Gd–Er) quaternary compounds and magnetic properties and lattice thermal expansion of $Gd_3CoAl_3Ge_2$. *J. Alloys Compd.* **2015**, *627*, 307–312.

85. Zhuravleva, M. A.; Pcionek, R. J.; Wang, X.; Schultz, A. J.; Kanatzidis, M. G. $REMGa_3Ge$ and $RE_3Ni_3Ga_8Ge_3$ (*M* = Ni, Co; *RE* = rare-earth element): New intermetallics synthesized

in liquid gallium. X-ray, electron, and neutron structure determination and magnetism. *Inorg. Chem.* **2003**, *42*, 6412–6424.

86. Zhuravleva, M. A.; Kanatzidis, M. G. Polygallide RE_2MGa$_9$Ge$_2$ (*RE* = Ce, Sm; *M* = Ni, Co) phases grown in molten gallium. *Inorg. Chem.* **2008**, *47*, 9471–9477.

87. Subbarao, U.; Jana, R.; Chondroudi, M.; Balasubramanian, M.; Kanatzidis, M. G.; Peter, S. C. Yb$_7$Ni$_4$InGe$_{12}$: a quaternary compound having mixed valent Yb atoms grown from indium flux. *Dalton Trans.* **2015**, *44*, 5797–5804.

88. Chondroudi, M.; Peter, S. C.; Malliakas, C. D.; Balasubramanian, M.; Li, Q.; Kanatzidis, M. G. Yb$_3$AuGe$_2$In$_3$: An ordered variant of the YbAuIn structure exhibiting mixed-valent Yb behavior. *Inorg. Chem.* **2011**, *50*, 1184–1193.

89. Salvador, J. R.; Kanatzidis, M. G. Indium flux synthesis of RE_4Ni$_2$InGe$_4$ (*RE* = Dy, Ho, Er, and Tm): An ordered quaternary variation on the binary phase Mg$_5$Si$_6$. *Inorg. Chem.* **2006**, *45*, 7091–7099.

90. Oliynyk, A. O.; Djama-Kayad, K.; Mar, A. Investigation of phase equilibria in the quaternary Ce–Mn–In–Ge system and isothermal sections of the boundary ternary systems at 800 °C. *J. Alloys Compd.* **2015**, *622*, 837–841.

91. Tobash, P. H.; Lins, D.; Bobev, S.; Lima, A.; Hundley, M. F.; Thompson, J. D.; Sarrao, J. L. Crystal growth, structural, and property studies on a family of ternary rare-earth phases RE_2InGe$_2$ (*RE* = Sm, Gd, Tb, Dy, Ho, Yb). *Chem. Mater.* **2005**, *17*, 5567–5573.

92. Graf, T.; Felser, C.; Parkin, S. S. P. Simple rules for the understanding of Heusler compounds. *Prog. Solid State Chem.* **2011**, *39*, 1–50.

93. Sales, B. C.; May, A. F.; McGuire, M. A.; Stone, M. B.; Singh, D. J.; Mandrus, D. Transport, thermal, and magnetic properties of the narrow-gap semiconductor $CrSb_2$. *Phys. Rev. B* **2012**, *86*, 235136-1–235136-7.

94. Calta, N. P.; Im, J.; Rodriguez, A. P.; Fang, L.; Bulgaris, D. E.; Chasapis, T. C.; Freeman, A. J.; Kanatzidis, M. G. Hybridization gap and Dresselhaus spin splitting in $EuIr_4In_2Ge_4$. *Angew. Chem. Int. Ed.* **2015**, *54*, 9186–9191.

95. Calta, N. P.; Im, J.; Fang, L.; Chasapis, T. C.; Bulgaris, D. E.; Chung, D. Y.; Kwok, W.-K.; Kanatzidis, M. G. Hybridization gap in the semiconducting compound $SrIr_4In_2Ge_4$. *Inorg. Chem.* **2016**, *55*, 12477–12481.

96. Oliynyk, A. O.; Mar, A. Discovery of intermetallic compounds from traditional to machine-learning approaches. *Acc. Chem. Res.* **2018**, *51*, 59–68.

97. Graser, J.; Kauwe, S. K.; Sparks, T. D. Machine learning and energy minimization approaches for crystal structure predictions: A review and new horizons. *Chem. Mater.* **2018**, *30*, 3601–3612.

98. Sparks, T. D.; Gaultois, M. W.; Oliynyk, A.; Brgoch, J.; Meredig, B. Data mining our way to the next generation of thermoelectrics. *Scr. Mater.* **2016**, *111*, 10–15.

99. Gaultois, M. W.; Oliynyk, A. O.; Mar, A.; Sparks, T. D.; Mulholland, G. J.; Meredig, B. Perspective: Web-based machine learning models for real-time screening of thermoelectric materials properties. *APL Mater.* **2016**, *4*, 053213-1–053213-11. For the implementation of these tools, see *http://thermoelectrics.citrination.com*.

100. Kauwe, S. K.; Graser, J.; Vazquez, A.; Sparks, T. D. Machine learning prediction of heat capacity for solid inorganics. *Integr. Mater. Manuf. Innov.* **2018**, *7*, 43–51.

101. Xue, D.; Balachandran, P. V.; Hogden, J.; Theiler, J.; Xue, D.; Lookman, T. Accelerated search for materials with targeted properties by adaptive design. *Nat. Commun.* **2016**, *7*, 11241-1–11241-9.

102. Balachandran, P. V.; Kowalski, B.; Sehirlioglu, A.; Lookman, T. Experimental search for high-temperature ferroelectric perovskites guided by two-step machine learning. *Nat. Commun.* **2018**, *9*, 1668-1–1668-9.

103. Zhuo, Y.; Mansouri Tehrani, A.; Brgoch, J. Predicting the band gaps of inorganic solids by machine learning. *J. Phys. Chem. Lett.* **2018**, *9*, 1668–1673.

104. Oliynyk, A. O.; Gaultois, M. W.; Hermus, M.; Morris, A. J.; Mar, A.; Brgoch, J. Searching for missing binary equiatomic phases: Complex crystal chemistry in the Hf–In system. *Inorg. Chem.* **2018**, *57*, 7966–7974.

105. Cao, B.; Adutwum, L. A.; Oliynyk, A. O.; Luber, E. J.; Olsen, B. C.; Mar, A.; Buriak, J. M. How to optimize materials and devices *via* design of experiments and machine learning: Demonstration using organic photovoltaics. *ACS Nano* **2018**, *12*, 7434–7444.

106. Mansouri Tehrani, A.; Oliynyk, A. O.; Parry, M.; Rizvi, Z.; Couper, S.; Lin, F.; Miyagi, L.; Sparks, T. D.; Brgoch, J. Machine learning directed search for ultraincompressible, superhard materials. *J. Am. Chem. Soc.* **2018**, *140*, 9844–9853.

107. Akselrud, L.; Grin, Yu. *WinCSD*: Software package for crystallographic calculations (Version 4). *J. Appl. Crystallogr.* **2014**, *47*, 803–805.

108. Gelato, L. M.; Parthé, E. *STRUCTURE TIDY* – a computer program to standardize crystal structure data. *J. Appl. Crystallogr.* **1987**, *20*, 139–143.

109. Spek, A. L. Structure validation in chemical crystallography. *Acta Crystallogr., Sect. D* **2009**, *65*, 148–155.

110. Pauling, L. *The Nature of the Chemical Bond*, 3rd ed.; Cornell University Press: Ithaca, NY, 1960.

111. Guo, S. P.; Meyers, J. J.; Tobash, P. H.; Bobev, S. Eleven new compounds in the *RE*–Cd–Ge systems (*RE* = Pr, Nd, Sm, Gd–Yb; Y): Crystal chemistry of the RE_2CdGe_2 series. *J. Solid State Chem.* **2012**, *192*, 16–32.

112. Young, A. G.; Hanton, L. R. Square planar silver(I) complexes: A rare but increasingly observed stereochemistry for silver(I). *Coord. Chem. Rev.* **2008**, *252*, 1346–1386.

113. *Pearson's Crystal Data: Crystal Structure Database for Inorganic Compounds (on DVD)*, release 2015/16; ASM International: Materials Park, OH, 2016.

114. Bażela, W.; Szytuła, A.; Todorović, J.; Zięba, A. Crystal and magnetic structure of the $NiMnGe_{1-n}Si_n$ system. *Phys. Status Solidi A* **1981**, *64*, 367–378.

115. Cordruwisch, E.; Kaczorowski, D.; Saccone, A.; Rogl, P.; Ferro, R. Constitution, structural chemistry, and magnetism of the ternary system Ce–Ag–Ge. *J. Phase Equilib.* **1999**, *20*, 407–422.

116. Castellanos, M.; West, A. R. Deviations from Vegard's law in oxide solid solutions. *J. Chem. Soc., Faraday Trans. 1* **1980**, *76*, 2159–2169.

117. Terada, Y.; Okhubo, K.; Mohri, T.; Suzuki, T. Thermal conductivity of intermetallic compounds with metallic bonding. *Mater. Trans.* **2002**, *43*, 3167–3176.

Appendix 1. Supplementary Data for Chapter 3

Table A1-1. Estimated Amounts of Phases (mol %) Found in Arc-melted Samples with Nominal Compositions $RE_4M_2AgGe_4$ and $RE_4M_2CdGe_4$.

***RE*$_4$Mn$_2$AgGe$_4$**	**La**	**Ce**	**Pr**	**Nd**	**Sm**	**Gd**	**Tb**	**Dy**	**Ho**	**Er**	**Tm**	**Lu**
RE$_4$Mn$_2$AgGe$_4$	63	47	100	95	93	68	80	72	80			
*RE*Mn$_2$Ge$_2$	22	33				27	16					
*RE*MnGe	5				4					41	20	
RE$_2$AgGe$_2$	10	20										
*RE*AgGe									16	48	66	94
RE$_5$Ge$_3$										11	14	6
*RE*Ge								24				
RE$_2$O$_3$				5			4	4	4			
*RE*O					3	5						
***RE*$_4$Fe$_2$AgGe$_4$**	**La**	**Ce**	**Pr**	**Nd**	**Sm**	**Gd**	**Tb**	**Dy**	**Ho**	**Er**	**Tm**	**Lu**
RE$_4$Fe$_2$AgGe$_4$		55	63	58	62	69	76	68	62	76	91	90
*RE*Fe$_2$Ge$_2$								21		15		
RE$_2$AgGe$_2$	40			20	8	12						
*RE*AgGe	60	12	15	18			16		19			
RE$_3$Ag$_4$Ge$_4$					13	12						
RE$_3$Ge$_5$				4	17	7	8	5				
RE$_5$Ge$_3$									19	4	6	
RE$_2$Ge$_3$												7
RE$_2$O$_3$								6		5	3	3
Fe$_3$O$_4$		33	22									
***RE*$_4$Co$_2$AgGe$_4$**	**La**	**Ce**	**Pr**	**Nd**	**Sm**	**Gd**	**Tb**	**Dy**	**Ho**	**Er**	**Tm**	**Lu**
RE$_4$Co$_2$AgGe$_4$			71	81	50	77	62	80	57	51	53	
*RE*Co$_2$Ge$_2$			12		10	23			22	33	21	

RE$_3$Co$_2$Ge$_4$					30		25					
*RE*CoGe												33
*RE*AgGe	48	41			10			20		16	26	56
*RE*Ag$_2$Ge$_2$	20	39										
RE$_5$Ge$_4$	32											
RE$_2$Ge$_3$									17			
*RE*Ag$_2$			17	11			13					
RE$_2$O$_3$		20		8					4			11
***RE*$_4$Ni$_2$AgGe$_4$**	**La**	**Ce**	**Pr**	**Nd**	**Sm**	**Gd**	**Tb**	**Dy**	**Ho**	**Er**	**Tm**	**Lu**
RE$_4$Ni$_2$AgGe$_4$			43	74	67	80	70	37	49			
*RE*NiGe			29	12	20		30	40	40		70	45
*RE*NiGe$_2$										26		25
*RE*AgGe	10		28	14	13	20		23	11	65	30	30
*RE*Ag$_2$		25										
RE$_3$Ge$_5$	90	75										
RE$_2$O$_3$										9		
***RE*$_4$Mn$_2$CdGe$_4$**	**La**	**Ce**	**Pr**	**Nd**	**Sm**	**Gd**	**Tb**	**Dy**	**Ho**	**Er**	**Tm**	**Lu**
RE$_4$Mn$_2$CdGe$_4$	75	88	91	72	90	24	54	73	98	98	98	98
*RE*Mn$_2$Ge$_2$	25	12	9	28		9	14					
RE$_2$CdGe$_2$					10	67	32					
RE$_3$Ge$_4$								27				
RE$_2$O$_3$									2	2	2	2
***RE*$_4$Fe$_2$CdGe$_4$**	**La**	**Ce**	**Pr**	**Nd**	**Sm**	**Gd**	**Tb**	**Dy**	**Ho**	**Er**	**Tm**	**Lu**
RE$_4$Fe$_2$CdGe$_4$				83	100	95	30	77	90	77	79	70
*RE*Fe$_2$Ge$_2$	50	75	20				17			12		28
RE$_2$CdGe$_2$			80	17			53	23	10	11	16	
*RE*Cd$_2$	50	25										

RE_2O_3						5					5	2
$RE_4Co_2CdGe_4$	**La**	**Ce**	**Pr**	**Nd**	**Sm**	**Gd**	**Tb**	**Dy**	**Ho**	**Er**	**Tm**	**Lu**
$RE_4Co_2CdGe_4$		85	83	77	100	95	77	86	89	86	74	
$RECo_2Ge_2$	65	15	9					10				
*RE*CoGe											10	67
RE_2CdGe_2			8	11								
$RECd_2$	35											
RE_2Ge_3									7	10	12	33
CoGe				12		5	23					
RE_2O_3								4	4	4	4	
$RE_4Ni_2CdGe_4$	**La**	**Ce**	**Pr**	**Nd**	**Sm**	**Gd**	**Tb**	**Dy**	**Ho**	**Er**	**Tm**	**Lu**
$RE_4Ni_2CdGe_4$					63	63	58	70	59	69		
$RENi_2Ge_2$												64
RE_2NiGe_3		35										
*RE*NiGe		42		30							70	15
RE_2CdGe_2									29	14	23	
RE_2CdNi_2	30		25	30			30	17				
$RECd_2Ni_2$	70											
RE_2Ge_3								13	12	17		
*RE*Ge		23										
RE_3Ge_2												21
*RE*Cd			30									
$NiGe_3$			45	25	12	12	12				7	
$RENiO_3$				15	25	25						

Table A1-2. Crystallographic Data for $Nd_4Mn_2AgGe_4$ and $Nd_4Mn_2Cd(Ge_{1-y}Si_y)_2$.

formula	$Nd_4Mn_{1.55(2)}Ag_{1.25(2)}Ge_4$	$Nd_4Mn_2Cd_{0.86(1)}Ge_4$	$Nd_4Mn_2Cd_{0.92(1)}Ge_{2.22(1)}Si_{1.78(1)}$	$Nd_4Mn_2Cd_{0.98(1)}Ge_{1.46(3)}Si_{2.54(3)}$	$Nd_4Mn_2Cd_{0.97(1)}Si_4$
formula mass (amu)	1087.31	1073.86	1001.40	976.12	908.79
space group	*C*2/*m* (No. 12)	*C*2/*m* (No. 12)	*C*2/*m* (No. 12)	*C*2/*m* (No. 12)	*C*2/*m* (No. 12)
a (Å)	16.281(5)	16.016(2)	16.224(12)	16.182(2)	16.0991(10)
b (Å)	4.3473(12)	4.2263(5)	4.305(3)	4.2870(5)	4.2746(3)
c (Å)	7.319(2)	7.1880(9)	7.305(5)	7.2859(9)	7.2517(5)
β (°)	106.855(4)	106.4057(18)	107.023(10)	107.1243(17)	107.2161(10)
V (Å^3)	495.8(2)	466.74(10)	487.9(6)	483.02(10)	476.68(6)
Z	2	2	2	2	2
T (K)	296(2)	296(2)	296.2	296(2)	296(2)
ρ_{calcd} (g cm^{-3})	7.284	7.641	6.816	6.712	6.332
crystal dimensions (mm)	0.08 × 0.03 × 0.02	0.04 × 0.03 × 0.02	0.06 × 0.04 × 0.03	0.06 × 0.05 × 0.04	0.04 × 0.04 × 0.02
μ(Mo $K\alpha$) (mm^{-1})	36.69	38.92	32.20	30.44	26.49
transmission factors	0.206–0.531	0.298–0.4554	0.352–0.516	0.309–0.480	0.517–0.642
2θ limits	5.23–66.53°	5.30–66.54°	5.25–66.22°	5.26–66.27°	5.30–66.44°
data collected	$-24 \le h \le 24$, $-6 \le k \le 6$, $-11 \le l \le 11$	$-24 \le h \le 24$, $-6 \le k \le 6$, $-10 \le l \le 11$	$-24 \le h \le 24$, $-6 \le k \le 6$, $-10 \le l \le 11$	$-24 \le h \le 24$, $-6 \le k \le 6$, $-11 \le l \le 10$	$-24 \le h \le 24$, $-6 \le k \le 6$, $-10 \le l \le 11$
no. of data collected	3485	3388	3492	3453	3449
no. of unique data, including $F_o^2 < 0$	1022 (R_{int} = 0.055)	992 (R_{int} = 0.029)	1015 (R_{int} = 0.033)	1006 (R_{int} = 0.044)	1004 (R_{int} = 0.038)
no. of unique data, with $F_o^2 > 2\sigma(F_o^2)$	798	898	875	840	863
no. of variables	38	38	39	40	37
$R(F)$ for $F_o^2 > 2\sigma(F_o^2)$ [a]	0.038	0.036	0.021	0.042	0.020
$R_w(F_o^2)$ [b]	0.091	0.099	0.041	0.127	0.035
goodness of fit	1.00	1.05	1.05	1.10	1.04
$(\Delta\rho)_{max}$, $(\Delta\rho)_{min}$ (e Å^{-3})	6.20, –2.52	4.95, –2.50	1.30, –1.41	7.07, –2.39	1.41, –1.40

[a] $R(F) = \sum||F_o| - |F_c|| / \sum|F_o|$. [b] $R_w(F_o^2) = [\sum[w(F_o^2 - F_c^2)^2] / \sum wF_o^4]^{1/2}$; $w^{-1} = [\sigma^2(F_o^2) + (Ap)^2 + Bp]$, where $p = [\max(F_o^2,0) + 2F_c^2] / 3$.

Table A1-3. Atomic Coordinates and Equivalent Isotropic Displacement Parameters (Å^2) [a] for $Nd_4Mn_2AgGe_4$ and $Nd_4Mn_2Cd(Ge_{1-y}Si_y)_2$.

	$Nd_4Mn_{1.55(2)}Ag_{1.25(2)}Ge_4$	$Nd_4Mn_2Cd_{0.86(1)}Ge_4$	$Nd_4Mn_2Cd_{0.92(1)}Ge_{2.22(1)}Si_{1.78(1)}$	$Nd_4Mn_2Cd_{0.98(1)}Ge_{1.46(3)}Si_{2.54(3)}$	$Nd_4Mn_2Cd_{0.97(1)}Si_4$
Nd1 in 4*i* (*x*, 0, *z*)					
x	0.34985(4)	0.34622(4)	0.34734(2)	0.34729(4)	0.34725(2)
z	0.07299(9)	0.07394(9)	0.07228(4)	0.07203(10)	0.07165(4)
U_{eq}	0.0111(2)	0.0031(2)	0.0092(1)	0.0094(2)	0.0069(1)
Nd2 in 4*i* (*x*, 0, *z*)					
x	0.58167(4)	0.58059(4)	0.58247(2)	0.58282(4)	0.58337(2)
z	0.36684(9)	0.36838(9)	0.37023(4)	0.37042(10)	0.37083(4)
U_{eq}	0.0112(2)	0.0030(2)	0.0103(2)	0.0092(4)	0.0068(1)
M in 4*i* (*x*, 0, *z*)					
occ	0.78(1) Mn, 0.22(1) Ag	1.00 Mn	1.00 Mn	1.00 Mn	1.00 Mn
x	0.2176(1)	0.2193(1)	0.21775(5)	0.2172(1)	0.21712(5)
z	0.6232(2)	0.6181(3)	0.6213(1)	0.6212(3)	0.6211(1)
U_{eq}	0.0116(4)	0.0070(4)	0.0103(2)	0.0105(4)	0.0077(2)
X in 2*a* (0, 0, 0)					
occupancy	0.827(6) Ag	0.860(9) Cd	0.922(3) Cd	0.982(8) Cd	0.974(3) Cd
U_{eq}	0.0199(5)	0.0069(4)	0.0160(2)	0.0157(5)	0.0130(2)
*Tt*1 in 4*i* (*x*, 0, *z*)					
occ	1.00 Ge	1.00 Ge	0.515(4) Ge, 0.485(4) Si	0.33(1) Ge, 0.67(1) Si	1.00 Si
x	0.0606(1)	0.0631(1)	0.06151(5)	0.0613(2)	0.0610(1)
z	0.6561(2)	0.6551(2)	0.6522(1)	0.6497(4)	0.6469(2)
U_{eq}	0.0118(3)	0.0066(3)	0.0100(2)	0.0114(8)	0.0074(3)
*Tt*2 in 4*i* (*x*, 0, *z*)					
occ	1.00 Ge	1.00 Ge	0.596(4) Ge, 0.404(4) Si	0.40(1) Ge, 0.60(1) Si	1.00 Si
x	0.1955(1)	0.1935(1)	0.19774(5)	0.1990(2)	0.2010(1)
z	0.2440(2)	0.2433(2)	0.2515(1)	0.2537(3)	0.2581(2)
U_{eq}	0.0120(3)	0.0071(3)	0.0103(2)	0.0111(7)	0.0093(3)

[a] U_{eq} is defined as one-third of the trace of the orthogonalized U_{ij} tensor.

Table A1-4. Interatomic Distances (Å) in $Nd_4Mn_2AgGe_4$ and $Nd_4Mn_2Cd(Ge_{1-y}Si_y)_4$.

	$Nd_4Mn_{1.55(2)}Ag_{1.25(2)}Ge_4$	$Nd_4Mn_2Cd_{0.86(1)}Ge_4$	$Nd_4Mn_2Cd_{0.92(1)}Ge_{2.22(1)}Si_{1.78(1)}$	$Nd_4Mn_2Cd_{0.98(1)}Ge_{1.46(3)}Si_{2.54(3)}$	$Nd_4Mn_2Cd_{0.97(1)}Si_4$
*RE*1–*Tt*1 (×2)	3.018(1)	2.961(1)	3.022(2)	3.021(2)	3.022(1)
*RE*1–*Tt*2	3.116(2)	3.024(2)	3.077(2)	3.063(2)	3.042(2)
*RE*1–*Tt*2 (×2)	3.108(1)	3.042(1)	3.123(2)	3.121(2)	3.129(1)
*RE*1–*M*	3.371(2)	3.333(2)	3.349(2)	3.339(2)	3.318(1)
*RE*1–*M* (×2)	3.506(1)	3.432(2)	3.485(2)	3.472(2)	3.460(1)
*RE*1–*X* (×2)	3.427(1)	3.399(1)	3.437(2)	3.426(1)	3.412(1)
*RE*2–*Tt*1 (×2)	3.122(1)	3.020(1)	3.066(2)	3.045(2)	3.022(1)
*RE*2–*Tt*2 (×2)	3.152(1)	3.076(1)	3.136(2)	3.130(2)	3.121(1)
*RE*2–*Tt*1 (×2)	3.145(1)	3.094(1)	3.145(2)	3.139(2)	3.132(1)
*RE*2–*M*	3.247(2)	3.178(2)	3.224(3)	3.218(2)	3.195(1)
*RE*2–*M* (×2)	3.276(1)	3.221(2)	3.234(2)	3.213(2)	3.192(1)
*RE*2–*X* (×2)	3.410(1)	3.348(1)	3.409(2)	3.398(1)	3.386(1)
M–*Tt*2 (×2)	2.621(1)	2.573(1)	2.575(2)	2.556(2)	2.528(1)
M–*Tt*1	2.637(2)	2.590(2)	2.610(2)	2.592(3)	2.575(2)
M–*Tt*2	2.692(2)	2.607(2)	2.625(2)	2.606(3)	2.568(2)
M–*M* (×2)	3.192(2)	3.042(3)	3.155(2)	3.153(3)	3.143(1)
X–*Tt*1 (×2)	2.958(1)	2.930(1)	2.990(2)	2.999(3)	3.002(2)
X–*Tt*2 (×2)	3.166(2)	3.099(2)	3.196(2)	3.206(2)	3.223(2)
*Tt*1–*Tt*1	2.548(3)	2.553(3)	2.515(2)	2.479(5)	2.433(3)

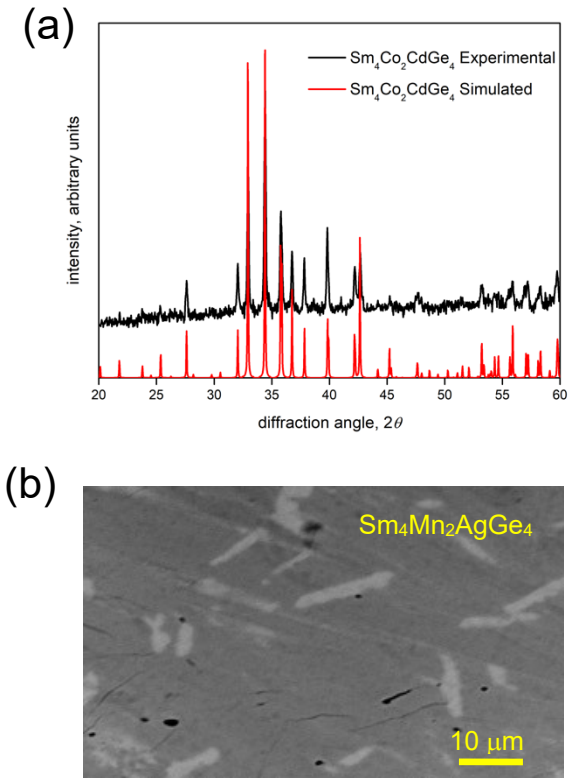

Figure A1-1. Representative XRD and SEM analysis of quaternary germanides. (a) Powder XRD pattern for $Sm_4CoCdGe_4$. (b) Backscattered SEM image of a two-phase sample containing $Sm_4Mn_2AgGe_4$ (dark) and Sm_5Ge_4 (light).